



**SENSITIVITY ANALYSIS OF EMPIRICAL  
PARAMETERS IN THE  
IONOSPHERE-PLASMAPAUSE MODEL**

THESIS

Janelle V. Jenniges, Captain, USAF  
AFIT/GAP/ENP/11-M03

**DEPARTMENT OF THE AIR FORCE  
AIR UNIVERSITY**

**AIR FORCE INSTITUTE OF TECHNOLOGY**

**Wright-Patterson Air Force Base, Ohio**

APPROVED FOR PUBLIC RELEASE; DISTRIBUTION UNLIMITED.

The views expressed in this thesis are those of the author and do not reflect the official policy or position of the United States Air Force, Department of Defense, or the United States Government. This work is declared a work of the U.S. Government and is not subject to copyright protection in the United States.

SENSITIVITY ANALYSIS OF EMPIRICAL PARAMETERS IN THE  
IONOSPHERE-PLASMASPHERE MODEL

THESIS

Presented to the Faculty  
Department of Engineering Physics  
Graduate School of Engineering and Management  
Air Force Institute of Technology  
Air University  
Air Education and Training Command  
in Partial Fulfillment of the Requirements for the  
Degree of Master of Science in Engineering Physics

Janelle V. Jenniges, BS, MBA

Captain, USAF

March 2011

APPROVED FOR PUBLIC RELEASE; DISTRIBUTION UNLIMITED.

SENSITIVITY ANALYSIS OF EMPIRICAL PARAMETERS IN THE  
IONOSPHERE-PLASMASPHERE MODEL

Janelle V. Jenniges, BS, MBA  
Captain, USAF

Approved:



Lt Col Ariel O. Acebal (Chairman)

1 MAR 2011

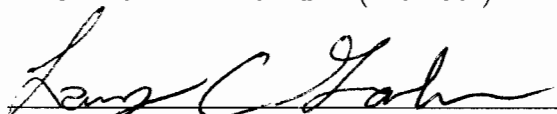
Date



Lt Col Robb M. Randall (Member)

1 MAR 2011

Date



Larry Gardner, PhD (Member)

1 MAR 2011

Date

## Abstract

A sensitivity analysis of empirical parameters used in physics-based models was completed in this study to determine their effect on electron densities and total electron content (TEC) in the ionosphere. The model used was the Ionosphere-Plasmasphere Model (IPM) developed by Utah State University. The empirical parameters studied include the  $O^+/O$  collision frequency, zonal wind, secondary electron production, nighttime  $\vec{E} \times \vec{B}$  drifts, and tidal structure. The sensitivity analysis was completed by comparing a default run of the IPM to a run with the parameter adjusted for three geophysical cases. Many of the comparisons resulted in nonlinear changes to the model output. Doubling the  $O^+/O$  collision frequency increased  $N_m F_2$  up to 250% in the equatorial anomalies. Setting the zonal winds to zero resulted in a 400% increase in TEC units (TECU) over the Southeast Pacific and a 50% decrease near Madagascar. It was found that changes in electron density and TEC are directly proportional to how daytime production is scaled to account for secondary electron production. Decreasing the nighttime downward  $\vec{E} \times \vec{B}$  drift resulted in a 160%–630% increase in low latitude TEC. Finally, modulating the  $\vec{E} \times \vec{B}$  drift to simulate tidal forcing reproduced the four-wave pattern of enhanced low latitude TEC.

## Acknowledgements

I first want to express my sincere thanks to my faculty advisor, Lt Col Ariel Acebal, for his guidance and support throughout my thesis. His knowledge of the subject matter and unique use of his ‘advisor skills’ kept the project interesting. He helped to keep me focused on the task at hand even when I was freaking out over everything I still needed to accomplish. I would like to extend a special thanks to my committee member, Larry Gardner, who spent many nights and weekends early on in the project working through issues with the models for me. His dedication to the project and the time spent making sure everything was working was indispensable. Thanks too, go to my other committee member, Lt Col Robb Randall, whose interest, encouragement, and sound advice was greatly appreciated.

A special thanks to Dr. Robert Schunk, Lie Zhu, and the rest of the team at USU for all of their insight and assistance in keeping this project moving forward. They patiently answered my questions and guided me through the details of the models. Without their knowledge and expertise this project would have never seen fruition.

I would also like to thank my fellow space weather students, for listening to all of my complaints and lamentations. They often provided a welcome distraction and helped me keep the overall goal in perspective. My final thanks go to my mom who spent many nights reading this document and providing valuable feedback. She also spent many telephone conversations listening to me ramble, and although she may not have always understood what I was talking about, she was always interested and provided support and encouragement.

Janelle V. Jenniges

## Table of Contents

	Page
Abstract .....	iv
Acknowledgements .....	v
List of Figures .....	viii
List of Tables .....	x
I. Introduction .....	1
1.1 Motivation and Background .....	1
1.2 Research Objective .....	3
1.3 Document Structure .....	3
II. Background .....	4
2.1 Chapter Overview .....	4
2.2 The Ionosphere and Plasmasphere .....	4
2.3 Ionosphere-Plasmasphere Model .....	18
III. Methodology .....	22
3.1 Chapter Overview .....	22
3.2 IPM Interpolation .....	22
3.3 Geophysical Condition Selection .....	24
3.4 Model Runs .....	24
3.5 Variable Calculation and Data Visualization .....	28
3.6 Analysis Techniques .....	30
IV. Results and Analysis .....	31
4.1 Chapter Overview .....	31
4.2 Baseline Runs .....	31
4.3 $O^+/O$ Collision Frequency .....	36
4.4 Zonal Winds .....	45
4.5 Daytime Production .....	57
4.6 Nighttime $\vec{E} \times \vec{B}$ Drift .....	59
4.7 Four-Wave Tidal Influence .....	65
V. Conclusions and Recommendations .....	75
5.1 Chapter Overview .....	75
5.2 Conclusions .....	75
5.3 Recommendations for Future Work .....	77

	Page
A. Ionosphere Forecast Model . . . . .	79
B. Governing Processes in the Ionosphere . . . . .	83
2.1 Neutral Atmosphere . . . . .	83
2.2 Production and Loss . . . . .	83
2.3 Transport . . . . .	88
Bibliography . . . . .	93
Vita . . . . .	96

## List of Figures

Figure	Page
1. Vertical structure of electron density .....	5
2. Solar irradiance and variability .....	6
3. Chapman layer .....	8
4. Production rates with and without secondary electrons .....	10
5. Thermospheric neutral winds .....	12
6. Formation of the equatorial anomaly .....	14
7. Chemical versus diffusive equilibrium in the $F_2$ region .....	15
8. Ion densities in the ionosphere and plasmasphere .....	17
9. Latitude-altitude grid used in the IPM .....	20
10. Example of longitudinal resolution in the IPM .....	20
11. Vertical resolution of the interpolated IPM output .....	23
12. TEC steady state comparison .....	26
13. TEC plotted in local time .....	29
14. TEC for all three geophysical cases .....	32
15. $N_m F_2$ for all three geophysical cases .....	34
16. $N_e$ at $90^\circ E$ for all three geophysical cases .....	35
17. $N_m F_2$ increase with doubled $O^+/O$ collision frequency .....	38
18. $N_m F_2$ at $0^\circ E$ with doubled $O^+/O$ collision frequency .....	40
19. $N_m F_2$ at $90^\circ E$ with doubled $O^+/O$ collision frequency .....	41
20. $N_m F_2$ at $180^\circ E$ with doubled $O^+/O$ collision frequency .....	42
21. $N_m F_2$ at $270^\circ E$ with doubled $O^+/O$ collision frequency .....	43
22. $N_e$ increase at $0^\circ E$ with doubled $O^+/O$ collision frequency .....	46

Figure	Page
23. HWM derived zonal thermospheric winds	47
24. Schematic of an offset dipole magnetic field	48
25. HWM zonal winds at 300km	50
26. TEC and $N_e$ with adjusted zonal winds for case 1 at 10UT	52
27. TEC and $N_e$ with adjusted zonal winds for case 2 at 10UT	53
28. TEC and $N_e$ with adjusted zonal winds for case 1 at 18UT	54
29. TEC and $N_e$ with adjusted zonal winds for case 2 at 18UT	55
30. TEC with adjusted zonal winds for case 3	56
31. The decrease in daytime production multiplication factor	58
32. TEC with decreased daytime production for case 1	60
33. TEC with decreased daytime production for case 2	61
34. TEC with decreased daytime production for case 3	62
35. Decrease in downward $\vec{E} \times \vec{B}$ drift	63
36. TEC and $N_e$ at 45°E with decreased downward $\vec{E} \times \vec{B}$ drift for case 1	66
37. TEC and $N_e$ at 45°E with decreased downward $\vec{E} \times \vec{B}$ drift for case 2	67
38. TEC and $N_e$ at 45°E with decreased downward $\vec{E} \times \vec{B}$ drift for case 3	68
39. TEC increase with decreased downward $\vec{E} \times \vec{B}$ drift	69
40. TEC with tidal forcing for case 1	72
41. $N_e$ at 400km with tidal forcing for case 1	73
42. TEC and 400km $N_e$ with tidal forcing for case 2 and 3	74
43. Major and minor neutral concentrations	84

## List of Tables

Table	Page
1. Differences in the IFM and IPM .....	23
2. Geophysical conditions .....	24
3. Adjustments made to the IPM .....	27
4. $N_m F_2$ increase with doubled $O^+/O$ collision frequency .....	44
5. TEC decrease with decreased daytime production .....	59
6. Maximum percent change in TEC and 400km $N_e$ at 13LT .....	71
7. Improvements to the Ionosphere Forecast Model .....	81

# SENSITIVITY ANALYSIS OF EMPIRICAL PARAMETERS IN THE IONOSPHERE-PLASMAPAUSE MODEL

## I. Introduction

### 1.1 Motivation and Background

As technology increases, the number of satellites and communication systems that dwell in the near-earth environment continue to increase as well. Additionally, communication signals both to and from space-based platforms also propagate through the near-earth environment. These satellites and communication systems are directly affected by this environment known as the ionosphere. The ionosphere is highly variable and has many effects on these systems including high frequency (HF) radio wave communication blackouts, Global Positioning System (GPS) degradation, and navigation communication impacts. Today's increased reliance on these systems requires more accurate ionospheric forecasts in order to mitigate these effects.

The ionosphere is the region in the earth's atmosphere that consists of a quasi-neutral ionized plasma. The structure and characteristics of the ionosphere are highly dependent on solar cycle, season, time of day, geographic location, and geomagnetic activity. Models are used to forecast how these variables change the ionosphere. Ionospheric model types include empirical, parameterized, numerical, tomographic, and physics-based models (*Schunk et al.*, 2002).

Physics-based models typically solve the continuity, momentum, and energy equations for ions and electrons taking into account all of the chemical and transport processes thought to be important. If the equations describing the physics and chemistry

of the ionosphere are correct, the model output should describe the real ionosphere. However, the accuracy of the model output depends on the quality of the input. The physics-based models also require atmospheric and magnetospheric inputs as boundary conditions and feedback mechanisms due to the inherent coupling of these systems. When sufficient data is not available, empirical models are often used.

Empirical models use a statistical solution based on limited physics and many years of observed data (climatology). In general, the empirical models are more correct than the physics-based models because the output is based on averaging real data instead of solving simplified physical equations (*Schunk*, 2010). However, when these empirical models are combined with the physics-based models, erroneous and inconsistent features can occur in the model output due to the combination of the averaged data from the empirical model and the more robust physics from the physics-based model. These inconsistencies need to be corrected via data assimilation within the model or by adjusting certain physical parameters in the model as determined by comparison with observed data prior to use of the model.

For example, when the physics-based Ionosphere Forecast Model (IFM) was compared to actual data as part of the validation process, it was found that certain model parameters had to be adjusted for the model output to match observations (Appendix A). The parameters that needed to be adjusted included the  $O^+/O$  collision frequency, nighttime drifts, daytime production, zonal winds, tidal forcing, and electron densities at high latitudes (*Schunk*, 2010). The IFM is part of the Global Assimilation of Ionospheric Measurements (GAIM) project developed at Utah State University (USU) and is used by the Air Force as the operational model to specify the ionosphere. The IFM has been validated against observations for different parameters by *Scherliess et al.* (2006), *Zhu et al.* (2006), *Decker and McNamara* (2007), *Thompson et al.* (2006), and others.

## 1.2 Research Objective

The objective of this research is to complete a sensitivity analysis of empirical parameters in a physics-based model. This is done by examining how adjusting certain physical parameters affects the model output. The model used in this project is the Ionosphere-Plasmasphere Model (IPM). The IPM is a physics-based ionospheric forecast model under development at USU for use in the GAIM Full Physics model, which is slated to be the next operational ionospheric forecast model for the Air Force. The physical parameters that are examined are the  $O^+/O$  collision frequency, nighttime drifts, daytime production, zonal winds, and tidal forcing. The default model output is compared to adjusted output to determine the extent of the changes in model output due to the adjustment of each physical parameter. This comparison will give an understanding of the importance of correctly specifying these physical parameters in the physics-based models.

## 1.3 Document Structure

This document is organized into five chapters. Chapter II provides background information on the creation and transport of the ionosphere and a detailed discussion of the IPM. Chapter III details the procedures used to conduct this research and outlines the selection of geophysical conditions, running the model, and data comparison techniques. Chapter IV gives the results and analysis of adjusting the physical parameters in a physics-based model while Chapter V summarizes these results, gives final conclusions, and outlines recommendations for future work.

## II. Background

### 2.1 Chapter Overview

This chapter provides background information necessary to understand this project and consists of two sections. The first section describes the composition of the ionosphere and plasmasphere. Both formation and transport of the ionosphere will be discussed in this section. The second section presents a detailed explanation of the IPM including the domain, resolution, and model physics.

### 2.2 The Ionosphere and Plasmasphere

The ionosphere is the region in the earth's atmosphere that consists of a quasi-neutral ionized plasma. It extends from about  $50\text{km}$  to beyond  $2000\text{km}$  (*Schunk and Nagy*, 2009). In the ionosphere, the plasma density is high enough to reflect radio frequencies while the neutral density remains high enough to influence plasma motion and chemistry. The ionosphere is broken up into different regions based on local peaks in the electron density. These regions include the D region from  $50\text{--}90\text{km}$ , the E region from  $90\text{--}140\text{km}$ , the  $F_1$  region from  $140\text{--}200\text{km}$ , and the  $F_2$  region from  $200\text{--}300\text{km}$ . The region above the  $F_2$  electron density peak is known as the topside ionosphere and extends from  $300\text{--}1500\text{km}$  at mid-latitudes (Figure 1). The plasmasphere is the region between the ionosphere and the magnetosphere consisting of low energy, relatively dense plasma that begins where  $H^+$  becomes the dominant ion and ends at 3–6 earth radii, depending on geomagnetic activity (*Tascione*, 1994). In general, the plasmasphere lies beneath the magnetic field line that maps to  $\pm 60^\circ$  magnetic latitude at the surface. The structure and characteristics of the ionospheric regions are highly dependent on solar cycle, season, time of day, geographic location, and geomagnetic activity.

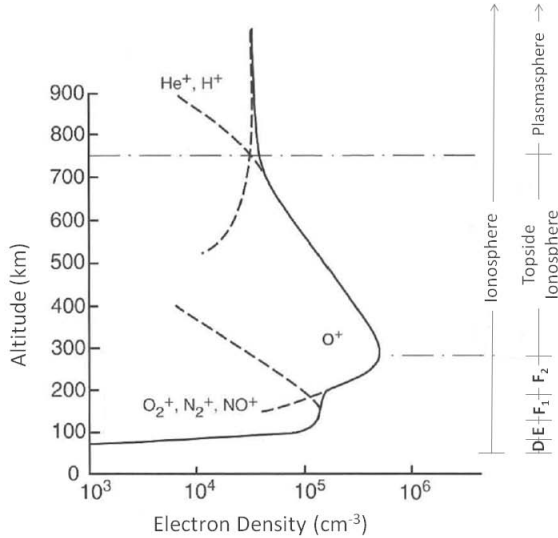


**Figure 1. Vertical structure of electron density and dominant ions showing the ionospheric regions and the plasmasphere (Adapted from Schunk and Nagy (2009))**

The production, loss, and transport of ions control the ion and electron density distributions in the ionosphere. These three processes can be described and modeled using the continuity equation (Equation 1). This mathematical expression equates the time rate of change of the density ( $\frac{dN_s}{dt}$ ) to the transport ( $-\nabla \cdot N_s \vec{u}_s$ ) and the production ( $P_s$ ) and loss ( $L_s$ ) of a species  $s$

$$\frac{dN_s}{dt} = -\nabla \cdot N_s \vec{u}_s + (P_s - L_s) \quad (1)$$

where  $N_s$  is the density of the species and  $\vec{u}_s$  is the velocity of the species. In general, transport is negligible below 200km and the change in ion concentration is described only by production and loss mechanisms. This *photochemical equilibrium* is valid in the D, E, and F<sub>1</sub> regions. Above 200km (F<sub>2</sub> region), production and loss no longer dominate the continuity equation and transport must be included. In the topside ionosphere and plasmasphere, production and loss are negligible and transport is the dominant process that controls ion and electron concentrations.

Where photochemical equilibrium applies in the D, E, and F<sub>1</sub> regions, the ionosphere can be represented by a simplified continuity equation as

$$\frac{dN_s}{dt} = P_s - L_s \quad (2)$$

where the change in species concentration is dependent only on production and loss processes. Photoionization is the primary production mechanism in these regions with chemical reactions, secondary electron production, and impact ionization acting as additional production mechanisms.

Photoionization creates ion-electron pairs by the absorption of solar extreme ultraviolet (EUV) and X-ray radiation by the neutrals. EUV and X-ray radiation encompasses a wavelength range from approximately 5nm to 110nm and are part of the solar flux emitted from the sun (Figure 2). While EUV and X-ray radiation account for only a small portion of the overall solar flux, it is these wavelengths that vary the most with solar cycle—over a 100% increase in irradiance from solar mini-

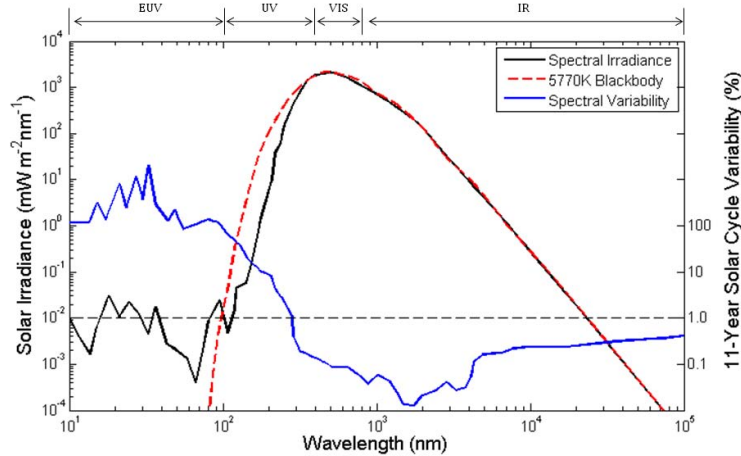


Figure 2. Solar irradiance and variability. Solar spectrum from 10nm to 10<sup>5</sup>nm (black) as compared to a 5770 K blackbody (red) and the solar spectrum's variability between solar maximum and solar minimum (blue, right axis). EUV radiation is much more variable with solar cycle than visible or infrared radiation (Adapted from *Lean (1991)*)

mum to solar maximum (*Lean*, 1991)—making the structure of the ionosphere highly dependent on the solar cycle as well.

Production due to photoionization also depends on the optical depth of the atmosphere, neutral concentrations, and ionization cross sections. The photoionization production rate for a particular species  $s$  is calculated using

$$P_s(z, \chi) = N_s(z) \int_0^{\lambda_{si}} I_\infty(\lambda) \exp[-\tau(z, \chi, \lambda)] \sigma_s^i(\lambda) d\lambda \quad (3)$$

where

- $I_\infty(\lambda)$  is the solar flux at the top of the atmosphere
- $N_s(z)$  is the number density
- $\tau(z, \chi, \lambda)$  is the optical depth
- $\sigma_s^i(\lambda)$  is the ionization cross section
- $\chi$  is the solar zenith angle
- $\lambda_{si}$  is the threshold wavelength for ionization

The optical depth determines how much of the incoming solar radiation passes through the atmosphere. It is dependent on the neutral concentrations as well as the relevant absorption cross sections and the angle of incoming solar radiation (the solar zenith angle). The highest concentration of neutrals occurs in the lower atmosphere with the density of each species falling off exponentially as a function of mass, i.e. the heavier species (Ar, O<sub>2</sub>, N<sub>2</sub>, and O) fall off faster than the lighter species (H and He) (see Appendix B). Because of this neutral structure, the optical depth is largest at low altitudes and the intensity of the incoming photon flux decreases as the radiation penetrates into the atmosphere. The combination of decreasing neutral densities and

increasing solar flux with altitude creates a region of maximum ionization known as a *Chapman layer* (Figure 3).

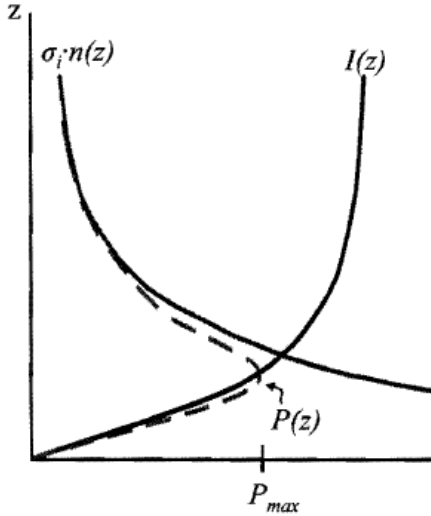


**Figure 3. Chapman layer and ionization curve (dashed line). Decreasing neutral densities ( $\sigma_i \cdot n(z)$ ) and increasing solar irradiance ( $I(z)$ ) with altitude create an ionization peak known as a Chapman layer at F region altitudes**

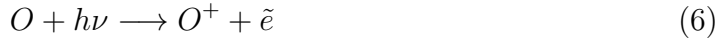
This region of maximum ionization is also highly dependent on the solar zenith angle (dependence is carried in the optical depth term). As the zenith angle increases, the peak ionization rate decreases and the height of the peak increases. (Schunk and Nagy, 2009). Therefore, local noon will have the highest ionization rate with the ionization peak at its lowest altitude; as the sun nears the horizon, the ionization rate decreases and the height of the peak increases. Photoionization is reduced significantly at night due to the loss of solar radiation. Ionization cross-sections are the probability that ionization will occur when an atom or molecule interacts with a photon. These cross-sections are dependent on the photon wavelength and the neutral species that the photon is interacting with.

Two important chemical reactions that create ions include the charge exchange reaction between  $O^+$  and  $H$  and the bimolecular ion–molecule reaction between  $O^+$

and  $N_2$ . These two reactions are given in Equations 4 and 5 below.



Secondary electron production occurs when an EUV or X-ray photon photoionizes an atom or molecule and the resulting electron has enough energy to then ionize a second atom or molecule. This process is shown in Equation 6



where  $\tilde{e}$  denotes the resulting high energy electron. The higher the energy of the electron, the more times it is able to ionize another atom or molecule as it moves down through the ionosphere. Figure 4 shows production rates both with and without secondary electrons. As seen in this figure, secondary electron production increases production rates throughout the ionosphere, but does not significantly alter the height of the peak density. The final production mechanism, impact ionization, is a result of particle precipitation and occurs primarily at high latitudes.

The primary loss processes in the D, E, and  $F_1$  regions are chemical reactions including ion-ion recombination, radiative recombination, dissociative recombination, ion-atom interchange, and associative detachment. The dominant loss mechanism in a region is determined by the chemical reaction rates; dissociative recombination dominates in the E region and ion-atom interchange dominates in the  $F_1$  region (*Schunk and Nagy, 2009*). Appendix B gives more details on reaction rates as well as production and loss mechanisms in the ionosphere.

Chemical reactions can be a production mechanism for one species while at the same time a loss mechanism for another species. This results in the continuity equa-

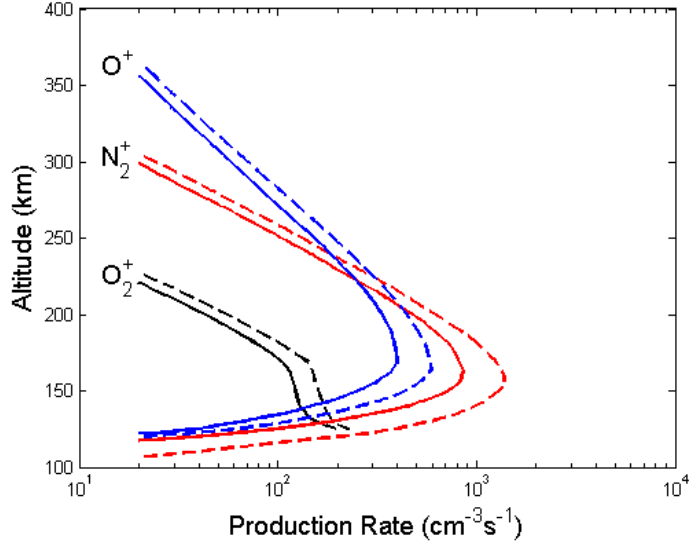


**Figure 4.** Production rates with (---) and without (—) secondary electrons for  $O^+$  (black),  $N_2^+$  (red), and  $O_2^+$  (blue) during solar minimum. Secondary electrons increase the production rate at all altitudes, but do not affect the altitude of the peak (Adapted from Schunk and Nagy (2009))

tion for one species being coupled to many other continuity equations. Therefore, a numerical solution is needed to solve even these simplified continuity equations.

In the  $F_2$  region, transport of the plasma becomes important. This is modeled using the full continuity equation (Equation 1) which includes the transport term  $(-\nabla \cdot N_s \vec{u}_s)$  and the transport velocity  $\vec{u}_s$ . To obtain the transport velocity, a solution to each species' momentum equation is needed. When thermal diffusion, Coriolis force, and centripetal force are all assumed to be negligible, the general momentum equation is given as

$$\rho_s \frac{D_s \vec{u}_s}{Dt} = -\nabla p_s - \nabla \cdot \tau_s + \rho_s \vec{g} + n_s q_s [\vec{E} + \vec{u}_s \times \vec{B}] + \sum_t \rho_s \nu_{st} (\vec{u}_t - \vec{u}_s) \quad (7)$$

where the subscripts denote the species  $s$  and the target  $t$ ,  $\rho_s$  is the mass density,  $D_s/Dt$  is the convective derivative,  $p_s$  is the pressure,  $k_b$  is Boltzmann's constant,  $\tau_s$  is the stress, and  $\nu_{st}$  is the collision frequency.

To understand plasma transport, the motion can be simplified into two cases; motion parallel to (along) the magnetic field, and motion perpendicular to (across) the magnetic field. The overall plasma motion is a combination of these two motions and can be understood by looking at the approximations, simplifying assumptions, and solutions to Equation 7.

For motion along the magnetic field, the diffusion approximation (steady state and subsonic), charge neutrality ( $n_e = n_i$ ), and zero current ( $n_e \vec{u}_e = n_i \vec{u}_i$ ) assumptions are made, resulting in the *ambipolar diffusion equation*

$$\vec{u}_{i\parallel} = -D_a \left[ \frac{1}{n_i} \nabla_{\parallel} n_i + \frac{1}{T_p} \nabla_{\parallel} T_p - \frac{m_i \vec{g}_{\parallel}}{2k_b T_p} + \frac{(\nabla \cdot \tau_i)_{\parallel}}{2n_i k_b T_p} - \frac{m_i}{2k_b T_p} \nu_{in} \vec{u}_{n\parallel} \right] \quad (8)$$

where the ambipolar diffusion coefficient ( $D_a$ ) and plasma temperature ( $T_p$ ) are

$$\begin{aligned} D_a &= \frac{2k_b T_p}{m_i \nu_{in}} \\ T_p &= \frac{T_e + T_i}{2} \end{aligned}$$

Equation 8 shows that the ions move along the magnetic field with the neutral wind subject to density gradients, temperature gradients, gravity, and stress forces.

The two dominant forces in this equation are the neutral winds and the density gradient. The parallel density gradient ( $\nabla_{\parallel} n_i$ ) points from low to high densities. For  $O^+$  in the  $F_2$  region, the gradient is in the upward direction because  $O^+$  is not present in the lower portions of the ionosphere. However, the diffusion coefficient is proceeded by a negative and the resulting motion due to diffusion is down the field lines. Above the  $F_2$  peak, the parallel  $O^+$  density gradient is downward during the day due to the ionization peak and upward at night due to the decay of  $O^+$ . The resulting flow due to diffusion in the topside ionosphere is then upward during the day and downward at night (*Schunk and Nagy, 2009*).

The thermospheric neutral winds at  $F_2$  region altitudes are primarily controlled by solar heating. In general, the thermospheric winds are directed radially away from the subsolar point with daytime meridional winds blowing toward the poles and nighttime meridional winds blowing toward the equator. As seen in Figure 5, the winds are weak near the subsolar point and increase in magnitude as the distance from the subsolar point increases. Weak daytime winds are due to higher ion concentrations resulting in increased ion drag on the neutral wind. Because the plasma is constrained to follow the field lines, the neutral winds push the plasma down the field lines to lower altitudes during the day and up the field lines to higher altitudes at night.

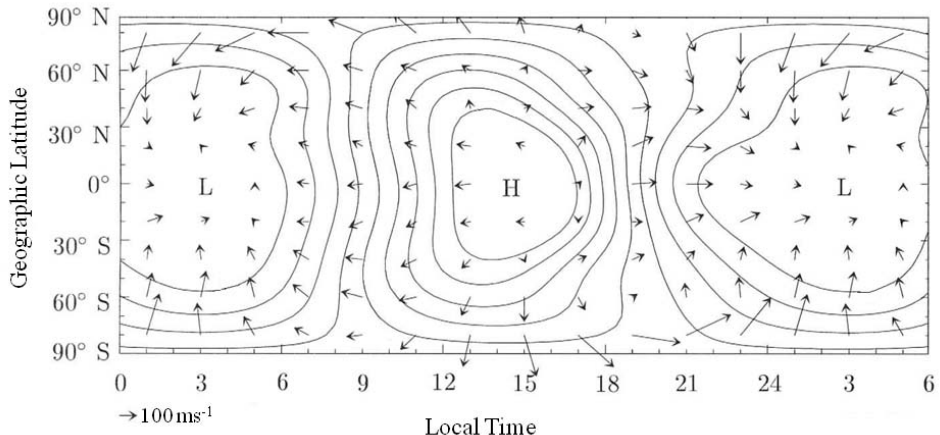


**Figure 5. Thermospheric neutral winds at 300 km calculated using HWM 93. Winds flow radially away from the subsolar point and are weaker on the day side (Adapted from Prolss (2004))**

Motion across the magnetic field can be looked at in a manner similar to motion along the magnetic field. After transforming to a reference frame moving with the neutral wind and separating the perpendicular motion into its two possible orientations, the motion across the magnetic field is described by

$$\vec{u}'_{s\perp} = \frac{1}{1+K^2} \left[ \frac{-D_s}{p_s} \nabla_{\perp} p_s + \frac{1}{\nu_{sn}} \vec{g}_{\perp} + \mu_s \vec{E}'_{\perp} \right] + \frac{1}{1+1/K^2} [\vec{u}_P + \vec{u}_g + \vec{u}_E] \quad (9)$$

where

$$\begin{aligned}
 K &= \frac{\omega_{cs}}{\nu_{sn}} && \text{is the gyrofrequency to collision frequency ratio} \\
 D_s &= \frac{k_b T_s}{m_s \nu_{sn}} && \text{is the diffusion coefficient} \\
 \mu_s &= \frac{q_s}{m_s \nu_{sn}} && \text{is the mobility}
 \end{aligned}$$

and where

$$\vec{u}_P = \frac{-1}{n_s q_s} \frac{(\nabla_{\perp} p_s \times \vec{B})}{B^2} \quad \text{is the gradient drift} \quad (10)$$

$$\vec{u}_g = \frac{m_s}{q_s} \frac{(\vec{g}_{\perp} \times \vec{B})}{B^2} \quad \text{is the gravitational drift} \quad (11)$$

$$\vec{u}_E = \frac{(\vec{E}'_{\perp} \times \vec{B})}{B^2} \quad \text{is the electromagnetic drift} \quad (12)$$

At high altitudes where collisions are negligible,  $K \rightarrow \infty$  and the first term in Equation 9 drops out leaving only motion perpendicular to both the magnetic field and the force. Electrons and ions drift across the magnetic field in opposite directions in the presence of pressure gradients and gravity, but they drift together in the presence of a perpendicular electric field. Typically the drifts due to pressure gradients and gravity are small and the dominant drift is the electromagnetic drift. At low latitudes, the electromagnetic drift is caused by the dynamo electric field created in the E region of the ionosphere and transmitted along the highly conductive dipole field lines to the F region. This electric field is generated by thermospheric winds as the ions are dragged across the magnetic field. The dynamo electric field is eastward during the day with a resulting upward  $\vec{E} \times \vec{B}$  drift; the opposite occurs at night with a westward electric field and a downward drift (Schunk and Nagy, 2009). The daytime combination of upward drifts and downward diffusion is responsible for the ionization

peaks on both sides of the geomagnetic equator known as the equatorial anomaly (Figure 6).

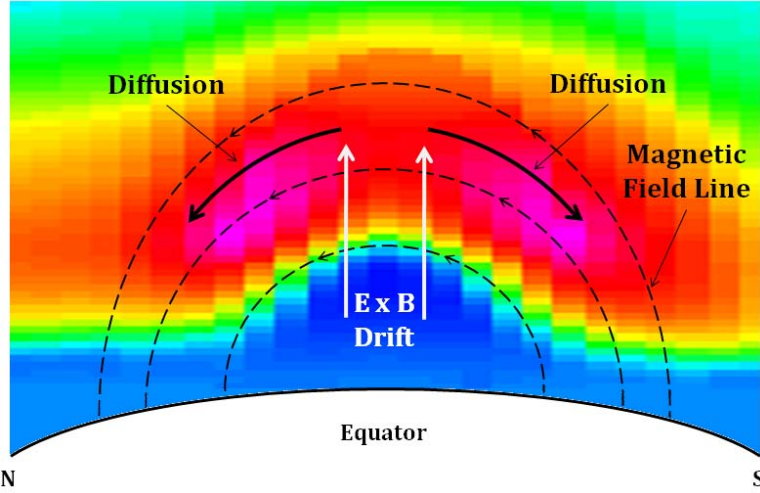


**Figure 6.** Formation of the equatorial anomaly (pink) is a result of upward  $\vec{E} \times \vec{B}$  drifts and diffusion down the magnetic field lines

At low altitudes where the magnetic field strength is small compared to the collision frequency  $K \rightarrow 0$ , and the second term in Equation 9 becomes negligible. This occurs because of the high concentration of neutrals in the lower atmosphere. The resulting plasma motion is perpendicular to the magnetic field but in the same direction as the force causing the motion. At intermediate locations where neither of the above approximations is valid (i.e.  $K \approx 1$ ), the plasma motion is a combination of the motion perpendicular to the magnetic field and parallel to the force (Kelley, 1989). Plasma movement occurs throughout the entire ionosphere, but becomes significant in the F<sub>2</sub> region and is the dominant process in the topside ionosphere and plasmasphere. The full derivation of the momentum equation solutions are included in Appendix B.

Transport and diffusion are important in the F<sub>2</sub> region because this is where the transition from chemical equilibrium in the D, E, and F<sub>1</sub> regions to diffusive

equilibrium in the topside ionosphere occurs. The location and magnitude of the  $F_2$  peak is dependent on where the chemical and diffusive equilibrium solutions are equal (Figure 7). Changes to either solution by changing such factors as the the diffusion rate or the neutral densities can change the magnitude and altitude of the  $F_2$  peak.

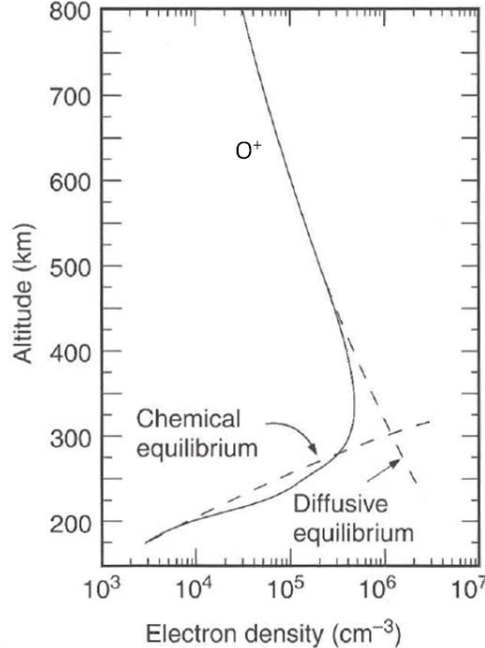


**Figure 7. Chemical versus diffusive equilibrium in the  $F_2$  region. The  $O^+$  density peak occurs where chemical and diffusive equilibrium are equal (Adapted from Schunk and Nagy (2009))**

Where transport and diffusion are the dominant processes in the topside ionosphere and plasmasphere, the ion and electron concentrations can be described by a *diffusive equilibrium* approximation. To simplify this approximation, Equation 8 is transformed from a Cartesian coordinate system to coordinates along the magnetic field as

$$\frac{1}{n_i} \frac{\partial n_i}{\partial r} = -\frac{m_i g}{2k_b T_p} - \frac{1}{T_p} \frac{\partial T_p}{\partial r} - \frac{\partial \tau_{i||}/\partial r}{2n_i k_b T_p} + \frac{(\vec{u}_n - \vec{u}_i)}{D_a} \quad (13)$$

Because the diffusion coefficient is inversely proportional to the neutral density, and

the neutral density decreases exponentially with altitude, the last term in Equation 13 becomes negligible as altitude increases ( $D_a \rightarrow \infty$ ). At high altitudes the stress term is small and can also be neglected ( $\tau_{i\parallel} \rightarrow 0$ ). With these approximations, the momentum equation becomes the classical *diffusive equilibrium equation*

$$\frac{1}{n_i} \frac{\partial n_i}{\partial r} = -\frac{1}{H_p} - \frac{1}{T_p} \frac{\partial T_p}{\partial r} \quad (14)$$

where  $H_p$  is the plasma scale height

$$H_p = \frac{2k_b T_p}{m_i g}$$

For an isothermal atmosphere and ignoring the variation of gravity with altitude, Equation 14 is integrated to give

$$n_i(r) = n_i(r_0) e^{-(r-r_0)/H_p} \quad (15)$$

where  $r$  indicates an altitude dependence and the subscript 0 corresponds to a reference altitude, typically the height of the F2 peak. Equation 15 shows that in this approximation the major ion density decreases exponentially with altitude at a rate governed by the plasma scale height (Schunk and Nagy, 2009).

In addition to the continuity and momentum equations, the temperature of each species due to heat transport is important in describing the true nature of the ionosphere. This temperature change is described by the energy equation

$$\frac{D_s}{Dt} \frac{3p_s}{2} = -\frac{5}{2} p_s (\nabla \cdot \vec{u}_s) - \nabla \cdot \vec{q}_s + Q_s - L_s + \sum_t \frac{\rho_s \nu_{st}}{m_s + m_t} 3k_b (T_t - T_s) \quad (16)$$

where  $\vec{q}_s$  is the heat flow,  $Q_s$  and  $L_s$  are the local heating and cooling rates, respectively, and all other variable are as described previously. The energy equation shows

the balance between the time rate of change of energy and the combination of compressional heating, divergence of heat flow, local heating and cooling, and transfer of energy due to elastic collisions.

Solving the coupled, nonlinear, continuity, momentum, and energy equations for each species is required to obtain a representative profile of the ion and electron concentrations in the ionosphere and plasmasphere. A numerical solution is needed as this is not possible analytically without making trivializing assumptions. Figure 8 shows a representative vertical profile of the major ions in the ionosphere and plasmasphere created using the numerical solution of the IPM. Molecular ions dominate in the E region while  $O^+$  is the principal ion in the F region and topside ionosphere. The transition to the plasmasphere occurs where  $H^+$  becomes the primary ion.

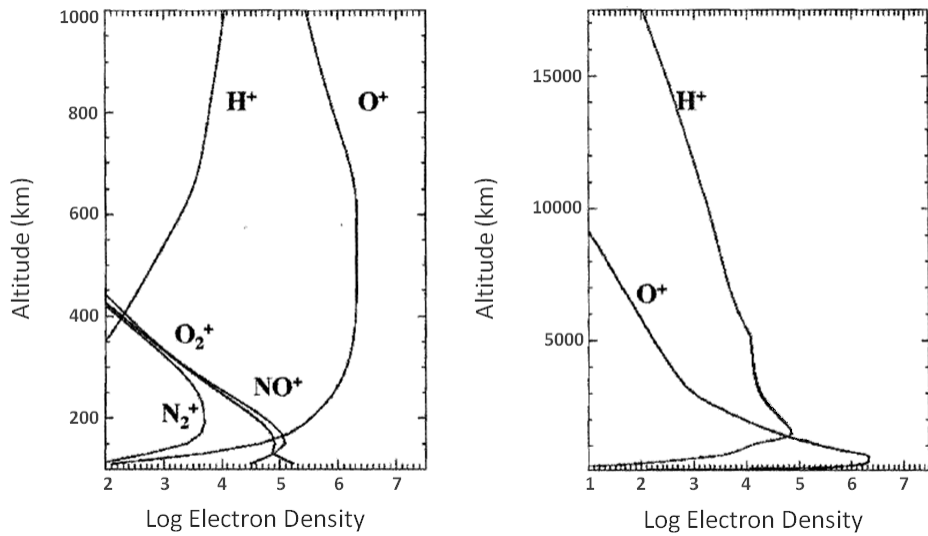


**Figure 8. Ion densities in the ionosphere and plasmasphere. Molecular ions dominate in the E region while  $O^+$  is the principal ion in the F region and topside ionosphere.  $H^+$  becomes the primary ion in the plasmasphere (Adapted from Scherliess *et al.* (2004))**

## 2.3 Ionosphere-Plasmasphere Model

The Ionosphere-Plasmasphere Model, developed at USU by Dr. Robert Schunk, is a physics-based model that calculates the three-dimensional time dependent ion and electron density distributions. The IPM solves the continuity and momentum equations for six ions ( $NO^+$ ,  $O_2^+$ ,  $N_2^+$ ,  $O^+$ ,  $H^+$ , and  $He^+$ ) on flux tubes that follow the geomagnetic field and allow for inter-hemispheric flow (*Schunk et al.*, 2004). A flux tube is a cylindrical region of space around a magnetic field line. The cross-sectional area of the tube and the strength of the magnetic field within the tube may change, but the magnetic flux through the tube always remains constant. The use of flux tubes simplifies the calculations by allowing the plasma densities of one flux tube to be solved independently of the other flux tubes. Due to the complex chemical reactions, the D region is not included in the IPM. In the E region, chemical equilibrium is assumed for  $NO^+$ ,  $O_2^+$ ,  $N_2^+$ , and  $O^+$ , and the four continuity equations are solved simultaneously at each grid point. Above the E region, both the continuity and momentum equations are solved for  $H^+$ ,  $O^+$ , and  $He^+$ . Included in the calculations are the effects of the equatorial electric field and interactions with the neutral atmosphere. Although solving along individual flux tubes creates output that is two-dimensional, calculating and tracking the ion densities for many flux tubes across many longitudes results in a three-dimensional global model.

The IPM can be run globally, regionally, or locally, and covers geomagnetic latitudes from  $60^\circ N$  to  $60^\circ S$  while extending vertically from 90–30000km to cover the E and F regions as well as the topside ionosphere and the plasmasphere (*Schunk et al.*, 2004). *Thompson et al.* (2009) shows that inclusion of the plasmasphere in the IPM is important due to model assimilation of GPS total electron content (TEC) data. The GPS path passes through the entire plasmasphere, and the plasmasphere's nighttime contribution to the TEC can exceed 50% (*Scherliess et al.*, 2009).

Although the IPM output is on a geomagnetic grid, a multi-step transformation of the field-aligned equations is performed within the model in order to allow a more efficient numerical solution (*Schunk et al.*, 2004; *Schunk and Nagy*, 2009). First the transport equations are transformed to spherical coordinates, then to dipolar coordinates, and finally to a “sinh” variable. This transformation optimizes the number of grid points along a field line. The result is unequally spaced grid points along each flux tube (Figure 9). The number of flux tubes varies with altitude; from 90–600km the flux tubes cross the equator at an equally spaced distance of 20km. This spacing increases exponentially with increasing altitude; a similar variation in vertical resolution has been successfully used in the IFM (Appendix A). The flux tube spacing has also been optimized in order for the model to converge at the transition heights. As vertical drifts lift and lower the ionosphere, flux tubes are added to or deleted from the upper and lower boundaries as required to maintain altitude boundaries.

The combination of unequally spaced grid points and flux tubes results in more grid points in the lower altitudes where more physical interactions occur and fewer grid points at higher altitudes where densities are lower. Figure 9 shows the latitude-altitude grid used in the IPM for both the ionosphere and plasmasphere. Latitudinal resolution is greatest over the equatorial anomalies and around 2.5° at mid-latitudes.

The longitudinal resolution depends on the number of longitudinal planes solved in the model. In the global mode, a 10° resolution is used with 36 planes. The resolution can be increased by decreasing the grid spacing to 1° in the regional and local modes; however, increasing the number of planes significantly increases computational runtime. Figure 10 shows the horizontal spacing of the IPM output using 48 longitudinal planes (7.5° resolution). Note that in the IPM the output is in geomagnetic coordinates but is plotted in geographic coordinates. The International Geomagnetic Reference Field (IGRF) is used in the IPM to model the earth’s magnetic field.

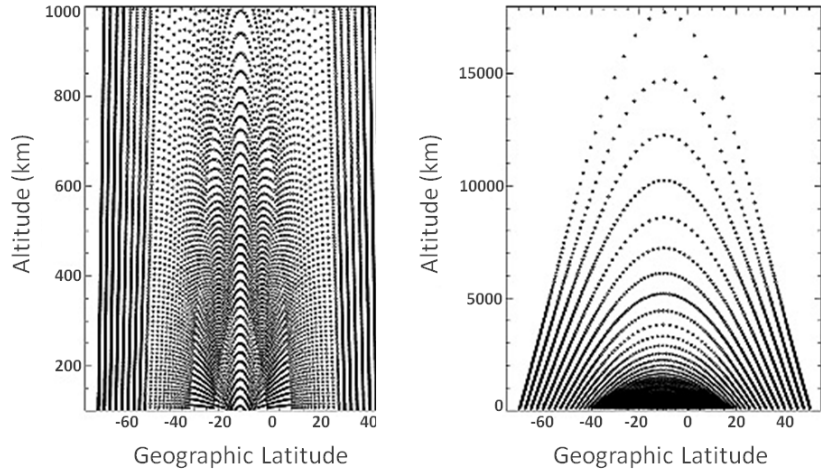


**Figure 9.** Latitude-altitude grid used in the IPM showing the vertical and latitudinal resolution of the IPM for the ionosphere (left) and the plasmasphere (right) (Adapted from Scherliess *et al.* (2004))

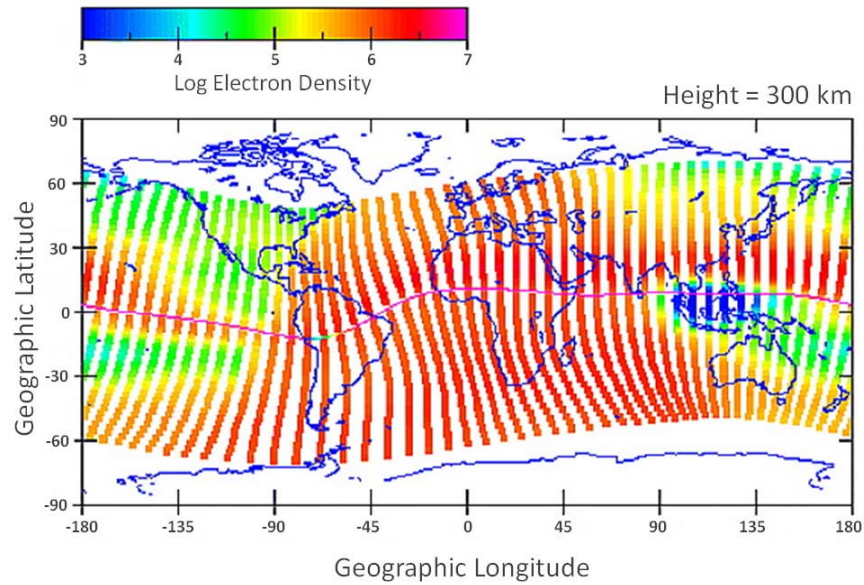


**Figure 10.** Example of longitudinal resolution in the IPM using 48 longitudinal planes. Plasma densities at 300km at 1200UT during solar medium conditions are displayed. The 'S' shape of the longitudinal planes is due to the geomagnetic flux tubes graphed geographically (Adapted from Scherliess *et al.* (2004))

The IPM calculates the ionospheric drivers needed to run the model using internal empirical models. The Mass Spectrometer and Incoherent Scatter (MSIS) model is used for the neutral density and temperature profiles. This empirical model provides these parameters based on a given set of geophysical conditions (solar cycle, season, geomagnetic activity, etc.) (*Hedin*, 1991). The zonal and meridional neutral winds are obtained from the Horizontal Wind Model (HWM) developed by *Hedin et al.* (1991). The dynamo electric fields are calculated in the IPM using the model developed by *Fejer et al.* (1999). The *Titheridge* (1998) model is used in the IPM to solve the energy equation and calculate the ion and electron temperature profiles.

Each empirical model is solved independently within the IPM; in addition, the E region, F<sub>1</sub> region, and F<sub>2</sub> region are also solved in separate modules within the IPM. As a final step, the IPM splices together the solutions for the different regions. Because each module is run separately within the IPM, the solutions may not be self-consistent. For example, although the zonal thermospheric winds play an important role in setting up the equatorial electric fields, the winds and the electric fields are calculated separately with their respective empirical models; therefore, the HWM calculated zonal wind does not affect the electric fields (*Schunk*, 2010). The zonal wind does, however, play a role in transport of the plasma because the momentum equation requires this term as part of its solution.

Using empirical model results to solve the physical equations in the physics-based model can lead to erroneous and inconsistent features in the physics-based model output. Data assimilation can be used to correct these errors, however, if data assimilation is not accomplished or if there is only a limited amount of data the model must be corrected by comparing the output to a large set of observational data and manually adjusting physical parameters in the model prior to its use. The result of correcting these errors is a more realistic plasma density distribution.

### III. Methodology

#### 3.1 Chapter Overview

This chapter describes the methods used to perform this study and is broken into five sections. The first section describes the interpolation of the IPM from magnetic flux tubes to a global geographic grid. The selection of the geophysical conditions chosen for this study is discussed in section two. The third section discusses the model runs including details on the model inputs and the adjustments made for each comparison. The fourth section outlines how the variables were calculated from the IPM output and plotted. The final section describes the techniques used to compare the model output.

#### 3.2 IPM Interpolation

Before the model physics could be investigated, the IPM had to be interpolated to output on a three-dimensional global grid. The IPM interpolation code takes the IPM output from a two-dimensional longitude versus altitude geomagnetic grid consisting of many flux tubes (Figure 9) and converts it to a global three-dimensional (latitude, longitude, altitude) geographic grid. The grid chosen was a  $3.5^\circ$  latitude by  $7.5^\circ$  longitude grid with variable altitude spacings (Figure 11). The interpolation code searches through each longitudinal plane within a set number of degrees of the desired latitude grid point and fills a vertical array with values going from low to high altitude. This array is then fit with a cubic spline interpolation routine. Once all of the latitudes have been filled, a cubic spline in longitude is performed to match the data to the longitudes of the IFM output grid (*Gardner, 2010*). The longitudes have to be fit as well because the IPM flux tubes form a type of ‘S’ shape in geographic coordinates (see Figure 10).

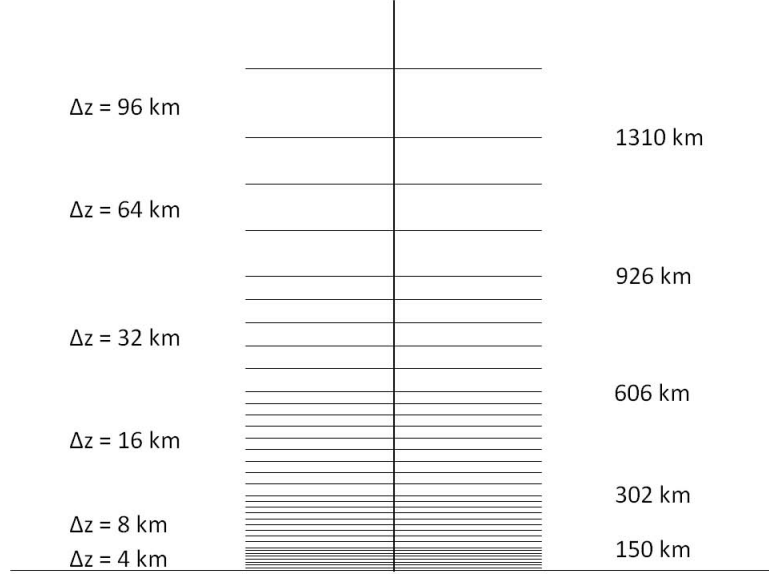


**Figure 11. Vertical resolution of the interpolated IPM output (not to scale)**

Multiple comparisons of the interpolated IPM output to the IFM output ensured that the IPM was producing valid results and that the interpolation code was working correctly. A general agreement between the IFM and IPM was achieved, however, the model output differed in some instances due to the differences in each model's physics. The physical differences between the IFM and IPM are given in Table 1. The interpolation code for the IPM was written by USU and modified with the aid of the IFM/IPM comparisons completed at the Air Force Institute of Technology (AFIT) for this thesis.

**Table 1. Differences in the IFM and IPM**

IFM	IPM
Simple magnetic field	IGRF magnetic field
Simple $H^+$ calculation	Rigorous $H^+$ calculation
No $He^+$	$He^+$ included
Coarse geographic grid	Geomagnetic flux tube grid
1600km top boundary	30000km top boundary
Temperatures numerically solved	Empirically-derived temperatures

### 3.3 Geophysical Condition Selection

The ionosphere varies significantly with season and solar cycle. In order to capture the large variation in these conditions while limiting the number of times the model needed to be run, three sets of geophysical conditions were chosen: solar maximum June solstice, solar minimum December solstice, and solar medium fall equinox. The combination of solar maximum and June solstice results in the highest levels of ionization in the northern hemisphere due to the high solar activity and increased daylight during summer. High solar activity during solar maximum corresponds to increased solar EUV radiation which is absorbed in earth's ionosphere through increased ionization. Solar minimum December solstice conditions have the opposite result: decreased solar activity with less solar EUV radiation and decreased daylight. Solar medium fall equinox was also chosen as a middle ground with medium levels of solar activity and equal daylight in each hemisphere. Table 2 summarizes the geophysical conditions for which the models were run.

**Table 2. Geophysical conditions chosen for the model runs**

Case #	Solar Cycle	Season	Year	Day	$F_{10.7}$	$K_p$	$A_p$
1	Minimum	December Solstice	1995	358	70	3	15
2	Medium	Fall Equinox	1998	267	140	3	15
3	Maximum	June Solstice	2001	172	220	3	15

### 3.4 Model Runs

The IPM requires as input the day, year, Universal Time (UT) start time, output interval, daily and 90-day average  $F_{10.7}$  solar flux, and daily  $A_p$  index. In addition, the resolution and domain of the IPM are set by specifying the number of degrees between each longitudinal plane and the upper and lower altitude boundaries. The altitudes are in reference to the height at which the flux tubes cross the equatorial plane.

For this project the IPM was set to output 36 longitudinal planes ( $10^\circ$  longitudinal resolution) with altitude bounds of  $135\text{--}20000\text{km}$  at the equator.

Once the model run has been started, four days of output are required before the model reaches a steady state solution. For example, if the model is started on day 354, the output will not be valid until day 358. To ensure that the model has indeed converged to a steady state solution, the fourth day of output (day 358) was compared to the fifth day of output (day 359) (Figure 12, top row) for the baseline run of case 1. In addition, the fourth day was also compared to the twentieth day (day 374) to show that the model first converges and then outputs the same steady state solution from that point on (Figure 12, bottom row). For these comparisons the input parameters were not changed. Although only the 0000UT TEC is shown in Figure 12, the comparisons were done for all 24 hours and included variables such as  $N_mF_2$ ,  $h_mF_2$ ,  $300\text{km}$   $N_e$ , and  $800\text{km}$   $N_e$ . The left hand plots of Figure 12 show the output from the fourth day of the model run, the middle plots show the fifth day (top) and twentieth day (bottom), and the right hand plots show the difference. As can be seen in both difference plots, there is less than a  $\pm 1$  TECU change in either of the comparisons. The cause for the differences in the bottom right plot around  $60^\circ\text{E}$  and  $300^\circ\text{E}$  are not known but are not in regions that are evaluated in this project and therefore do not affect the results. Further investigation of the cause for the differences in these regions is recommended for future work. The negligible differences across the rest of the plot, which can be attributed to solar zenith angle changes, confirms the assumption that the model has converged to the steady state solution in the areas of interest by the fourth day of output.

With steady state conditions not reached until the fourth day of output and the 1:1 ratio of model runtime to output, the IPM takes at least five days of runtime to obtain one day of usable output. To force the model to run faster, the IPM was

## Total Electron Content Steady State Comparison

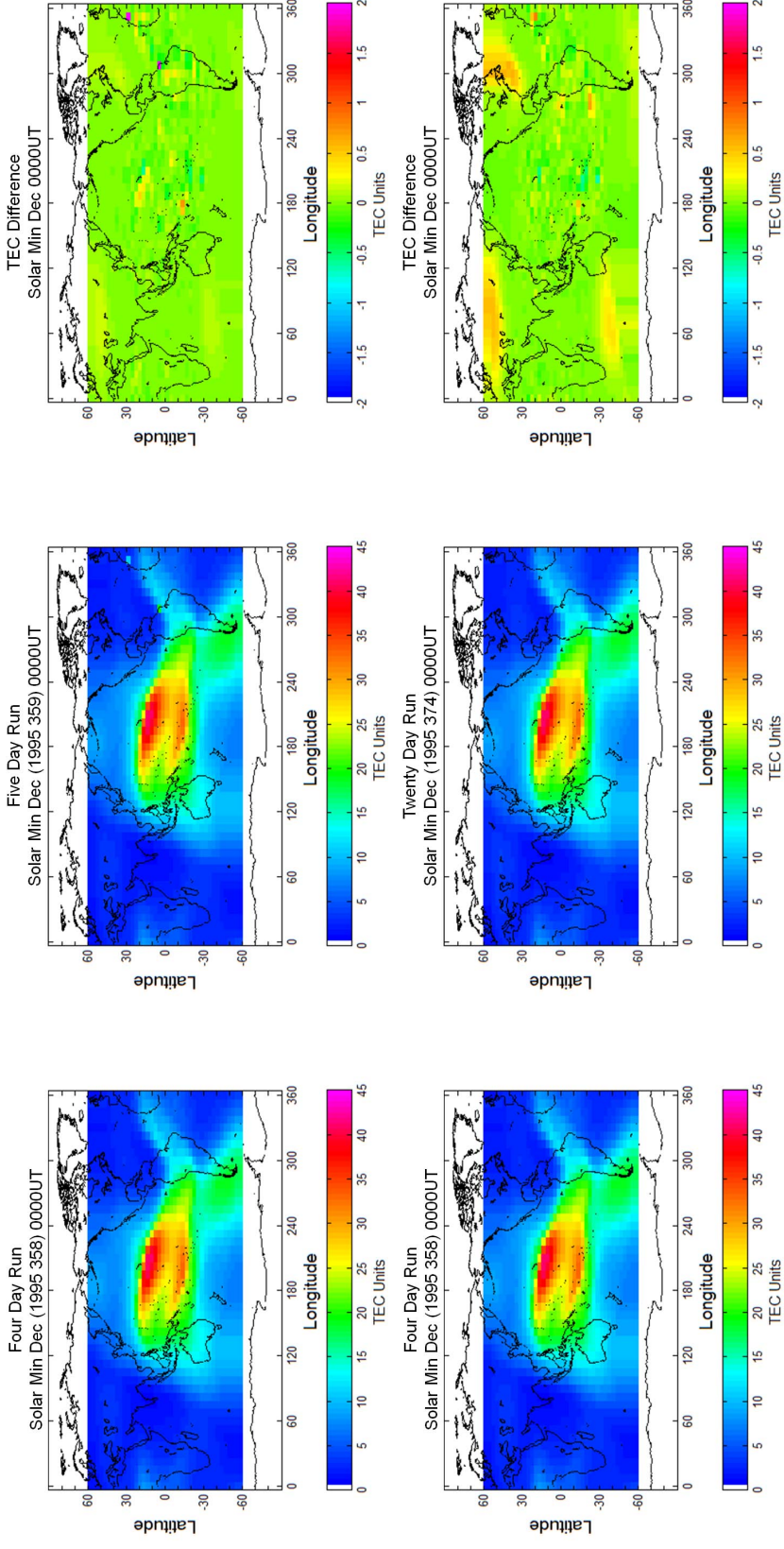


Figure 12. TEC steady state comparison for the four day run compared to a five day run (top) and the four day run compared to a twenty day run (bottom). The left plot is the four day run, the middle plot is the 5 and 20 day run, and the right plot is the difference. After day five, the model output has reached steady state conditions and differs by less than 1 TECU, which can be attributed to the change in zenith angle

ran with three different altitude sections (135–5000km, 5000–11000km, and 11000–20000km). These sections are recombined into one continuous altitude section using the interpolation code. The IPM does not require an end time and will continue until the run is manually terminated. The IPM outputs the electron density, six ion densities, and temperature arrays in large text files. The interpolation code can be run on any of these output variables.

To investigate the physical parameters in the IPM, an input file was created to turn ‘off’ and ‘on’ different sections of code in the IPM. Turning ‘on’ a section of code changed the parameter specified in the input file. The adjustments for each of the five parameters ( $O^+/O$  collision frequency, daytime production rate, nighttime drift, zonal winds, and tidal forcing), in addition to the default settings, are given in Table 3 and are discussed in more detail in Chapter IV. These physical parameters are known to be uncertain in physics-based models and the adjustments were motivated by comparisons with the 12-year TOPEX TEC database (Schunk, 2010).

**Table 3. Adjustments made to the IPM**

Parameter	Default	Adjustment
$O^+/O$ Collision Frequency	Normal	Doubled
Zonal Winds	HWM derived zonal winds	Zonal winds set to zero
Tidal Forcing	No tidal forcing	Tidal forcing included by modulating the $\vec{E} \times \vec{B}$ drift
Daytime Production	Production multiplied by 1.8	Multiplication factor decreased as a linear function of $F_{10.7}$
Nighttime Drifts	No correction to drifts	Decreased the nighttime $\vec{E} \times \vec{B}$ drift as a linear function of $F_{10.7}$

In total, 18 model runs were completed: 1 baseline run and 5 adjustments for 3 geophysical cases. The model runs were done in collaboration with Utah State

University. USU developed both the IFM and IPM and changes to the models were made by USU researchers. The models were run remotely on USU computers; the model output was downloaded to AFIT computers where the analysis was completed.

### 3.5 Variable Calculation and Data Visualization

Data visualization is an important part of research because it allows large arrays of data to be interpreted quickly and easily. This project produced hundreds of arrays of data while investigating the total electron content (TEC), electron density ( $N_e$ ), and  $F_2$  region peak density ( $N_mF_2$ ) and height ( $h_mF_2$ ) of the ionosphere. This section discusses how these variables were calculated and plotted from the IPM output, and the technique used to create the longitude slice plots and the local time plots.

The IPM outputs a 3-D (latitude, longitude, altitude) array of electron densities for every hour (in UT) in a text file. This data was read into MATLAB where it was then manipulated to compute the required variables and to plot the data in a variety of configurations. The TEC was calculated by adding up the electron density at every altitude for each latitude/longitude pair and then converting the densities to TECU by dividing by  $10^{16}$  electrons/m<sup>2</sup>. The  $N_mF_2$  and  $h_mF_2$  were calculated together by systematically stepping through every altitude and locating the largest value for every latitude/longitude pair ( $N_mF_2$ ) and the height at which that value occurred ( $h_mF_2$ ). These variables were saved in 2-D arrays for every hour calculated. The electron density arrays at 300km, 400km, and 800km were also saved in 2-D arrays for comparison and evaluation. The longitude slice plots were created in a manner similar to the  $N_e$  plots. Instead of choosing one specific altitude, one longitude was selected to display. The longitude slice plots are more intuitive when plotted in local time; this was accomplished by simply calculating the local time of each plot by utilizing the UT offset for the chosen longitude.

The 2-D arrays were plotted using MATLAB's *imagesc* plotting function and a 72-hue colormap. The minimum value and maximum value of the entire 24-hour period were found for each variable and these values were used as the boundaries of the colorscale. This ensured that the colorscale did not vary between plots. The IPM does not cover the high latitude regions and so these areas (poleward of  $\pm 60^\circ$ ) were left white to indicate no data.

Although the UT plots are the most intuitive (day versus night is easy to distinguish and understand), plotting in local time can highlight diurnal trends in the data. When the same local time for each location is plotted together, the variations due to geographic location (instead of time) can easily be seen. For example, when the TEC is plotted at 1200LT (Figure 13), the longitudinal variation in the equatorial anomalies is easily identifiable. This type of plot was created by determining the UT offset for each longitude and then choosing the correct local time longitude from each UT array and saving the data to a new local time array. This array was then plotted in the same manner as the UT arrays.

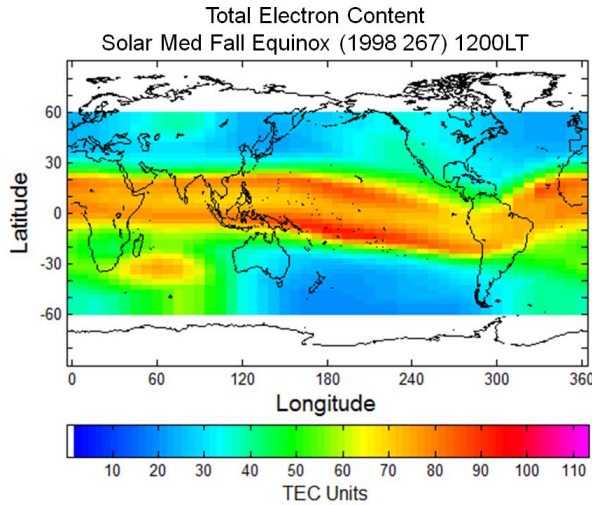


**Figure 13.** TEC plotted in local time highlights the variation in TEC across longitudes

### 3.6 Analysis Techniques

The next step in this project was to evaluate how adjusting the physical parameters affected the model output. For this evaluation, two comparison techniques were used—a difference and a percentage change. These comparisons were done over the entire spatial grid in order to highlight regions of differences. The difference was computed by subtracting the default IPM output value at each grid point from the adjusted IPM output value at the corresponding grid point (Equation 17). The percent increase (or decrease) was calculated by dividing the difference by the default IPM output value and then multiplying by 100 to get a percentage (Equation 18).

$$\text{Difference} = \text{IPM}_{adjusted} - \text{IPM}_{default} \quad (17)$$

$$\text{Percent Increase} = \frac{\text{IPM}_{adjusted} - \text{IPM}_{default}}{\text{IPM}_{default}} \times 100 \quad (18)$$

These comparisons were done for each variable of interest (TEC,  $N_mF_2$ ,  $h_mF_2$ , and  $400\text{km } N_e$ ) every hour for 24 hours and plotted in both UT and local time (LT). Additionally, different longitudes were chosen to do a latitude versus altitude (longitude slice) comparison of the electron density. In general, the longitudes were selected based on where the TEC or  $N_mF_2$  showed large changes. The longitude slices are displayed only in local time.

## IV. Results and Analysis

### 4.1 Chapter Overview

The objective of this project was to complete a sensitivity analysis of certain physical parameters in a physics-based model and to examine how adjusting these parameters affects the model output. The parameters that were investigated are known to have inherent uncertainty within models. Each of the parameters were adjusted independently of each other to isolate the effects of each adjustment on the model output. First the baseline results for each geophysical case (see Chapter II) are given where no adjustments were made to the model. Next, the effects of adjusting each parameter are discussed. The  $O^+/O$  collision frequency is examined first followed by the zonal winds, daytime production, nighttime  $\vec{E} \times \vec{B}$  drift, and finally the four-wave tidal influence. Comparing the baseline output to the adjusted output gives an understanding of the importance of correctly specifying these physical parameters in a physics-based model.

### 4.2 Baseline Runs

This section gives the default output from the IPM for which no adjustments were made to any parameters. Understanding the baseline results is imperative to understanding how adjusting the physical parameters affects this output. Figure 14 shows plots of TEC for all three geophysical conditions at both 0000UT and 1200UT. Maximum daytime values of TEC range from 45–160 TECU while nighttime values are as low as 2–3 TECU. As expected, TEC is a function of the incoming solar flux and increases from solar minimum to solar maximum. In the 0000UT plots, 1200LT is near  $180^\circ E$  and the higher daytime TEC values are due to the presence of photoionization. The terminators can also be clearly seen in these plots with the area of illumination

## Total Electron Content for All Three Geophysical Cases

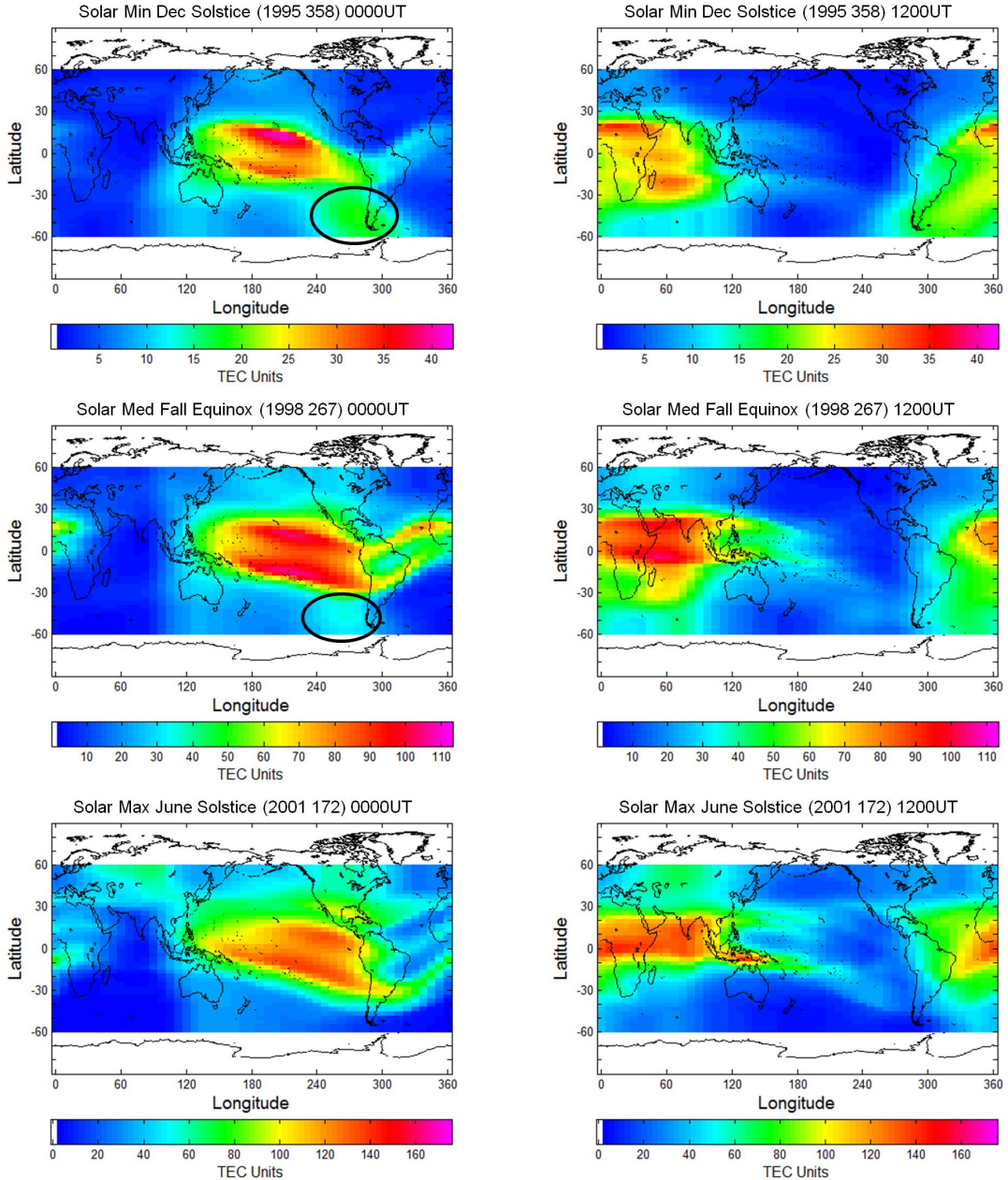


Figure 14. TEC for all three geophysical cases (solar minimum December solstice - top, solar medium fall equinox - middle, and solar maximum June solstice - bottom) at both 0000UT (left) and 1200UT (right). Both solar cycle and seasonal effects can be seen in the differences in TEC in these plots. The circled region is the Weddell Sea Anomaly. Note that the scales are different for each geophysical case

changing according to season. The equatorial anomaly regions of enhanced TEC on each side of the geomagnetic equator are also evident in these plots.

Similar to the TEC plots, the  $N_m F_2$  for all three geophysical conditions is plotted in Figure 15. These plots show the peak density in the  $F_2$  region of the ionosphere, which is a significant contributor to the overall TEC. Because of this, the same features (equatorial anomalies, and day/night, seasonal, and solar cycle differences) can also be seen in these plots. The scale of these plots is the log of the electron density, i.e. a value of '5' means  $10^5$  electrons/cm $^{-3}$ .

Also of note in the baseline runs is the area of enhanced TEC and  $N_m F_2$  over the Southeast Pacific during solar minimum and solar medium (circled in the top and middle left hand plots of Figures 14 and 15). This feature shows up throughout the comparisons and is a result of the Weddell Sea Anomaly (WSA). The WSA in the ionosphere is characterized by higher plasma densities at night than during the day in the region near the Weddell Sea (Antarctica). This nighttime enhancement is due to the vertical plasma drifts resulting from the combination of thermospheric neutral winds and the magnetic field configuration in this region (*Horvath and Essex, 2003*).

*Jee et al. (2009)* found that the WSA is most prominent during December solstice (southern hemisphere summer) and occurs in all seasons for low  $F_{10.7}$  values while for high  $F_{10.7}$  values it is not as prominent during southern hemisphere winter (June solstice).

The altitude structure of the electron density is also important because densities can increase at one altitude while decreasing at another with no resulting change in TEC. Figure 16 shows a latitude versus altitude plot of the the electron density at 90°E at both 0000LT and 1200LT. Both the solar cycle and seasonal dependence of  $N_e$  is evident in these plots. As solar activity increases, short wavelength solar radiation increases resulting in higher levels of photoionization and  $N_e$ . The seasonal

## $F_2$ Peak Electron Density for All Three Geophysical Cases

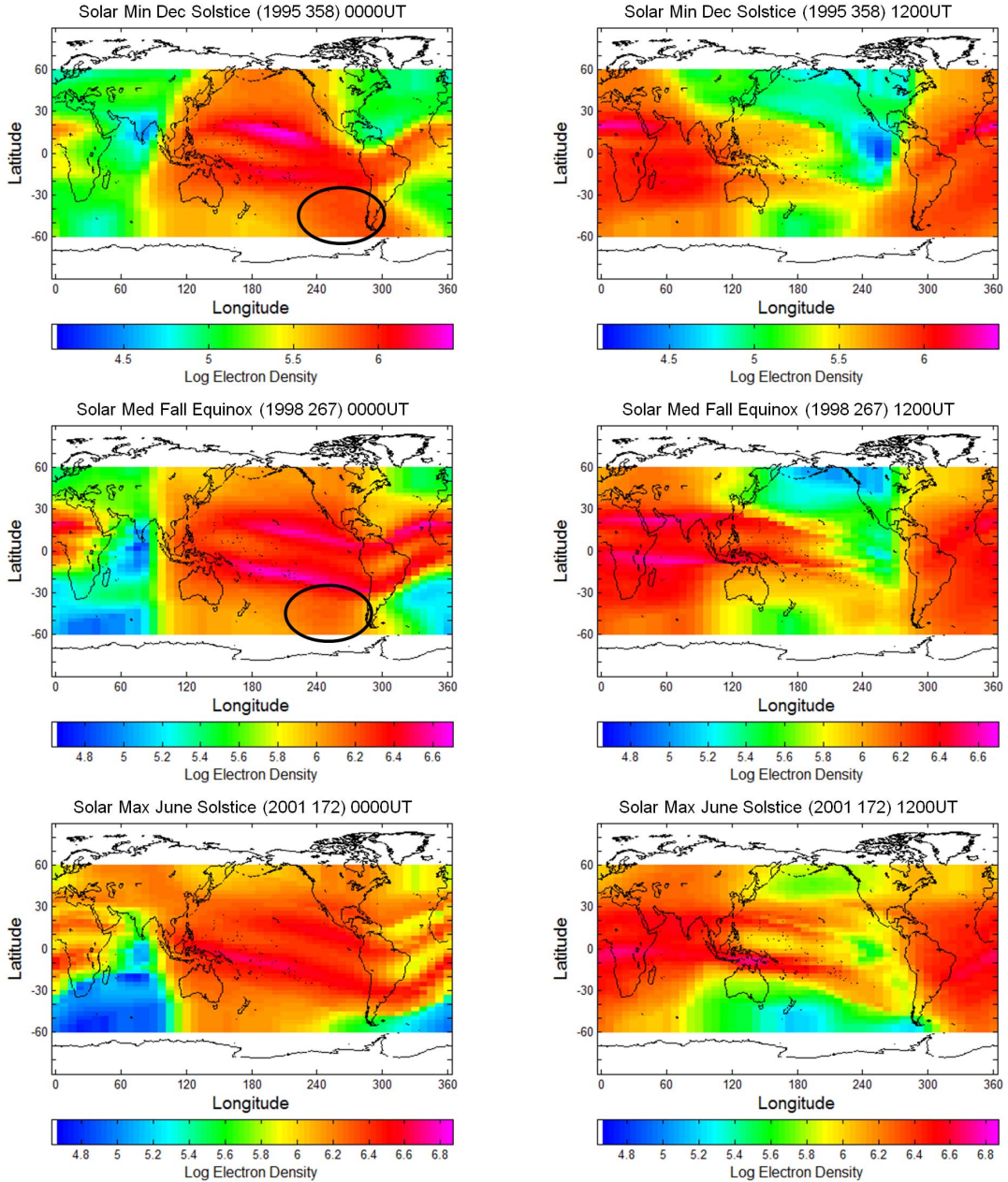


Figure 15.  $N_m F_2$  for all three geophysical cases (solar minimum December solstice - top, solar medium fall equinox - middle, and solar maximum June solstice - bottom) at both 0000UT (left) and 1200UT (right). Both solar cycle and seasonal effects can be seen in the differences in  $N_m F_2$  in these plots. The circled region is the Weddell Sea Anomaly. Note that the scales are different for each geophysical case

## 90°E Electron Density for All Three Geophysical Cases

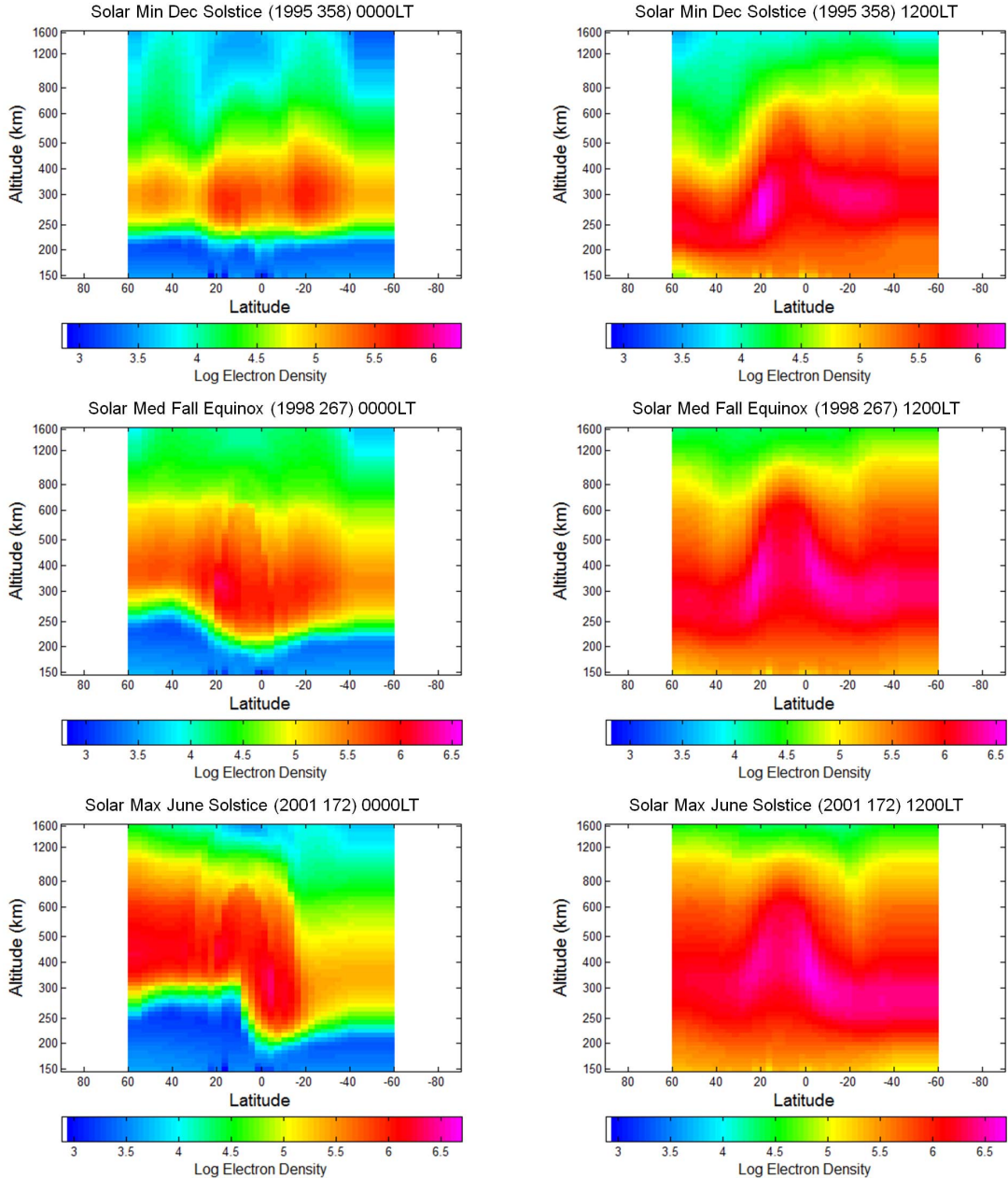


Figure 16.  $N_e$  at 90°E for all three geophysical cases (solar minimum December solstice - top, solar medium fall equinox - middle, and solar maximum June solstice - bottom) at both 0000UT (left) and 1200UT (right). Both solar cycle and seasonal effects can be seen in the differences in  $N_e$  in these plots. Note that the scales are different for each geophysical case

dependence is seen in the *winter anomaly*—higher plasma densities in the winter hemisphere than in the summer hemisphere. Even though the ion production rate is higher in the summer hemisphere, the loss rate is also much higher and overwhelms the increase in ionization due to production. Additionally, the plasma is transported by meridional neutral winds along the field lines from the summer (hot) hemisphere to the winter (cold) hemisphere. These processes result in the summer hemisphere density peak being at a higher altitude and lower in magnitude than the winter hemisphere density peak. This structure is evident in the top and bottom plots of Figure 16. These plots are especially useful to show the development and subsequent depletion of the equatorial anomalies as well as the location and magnitude of the peak density.

### 4.3 $O^+/O$ Collision Frequency

The  $O^+/O$  collision frequency was the first parameter investigated. For this comparison, the standard value of the  $O^+/O$  collision frequency as calculated by *Schunk and Nagy* (2009) was doubled. This directly affects both diffusion along the magnetic field and the plasma’s interaction with the thermospheric neutral wind (see Figure 5). The diffusion rate is inversely proportional to the collision frequency, therefore doubling the collision frequency reduces diffusion by a factor of two. The result is slower downward diffusion of  $O^+$  which aids in maintaining the F region plasma. Additionally, doubling the  $O^+/O$  collision frequency acts to significantly increase the coupling of the plasma drifts to the neutral wind. The thermospheric neutral winds are directed radially away from the subsolar point with daytime meridional winds blowing toward the poles and nighttime meridional winds blowing toward the equator. During the day the wind becomes more effective in driving the plasma to lower altitudes, and at night the wind is more effective in driving the plasma to higher altitudes.

During the day, the reduced  $O^+$  diffusion and the increased neutral wind effect act to oppose each other. Even though the neutral winds are doubled, daytime neutral winds are weak, and so the wind effect and diffusion effect are nearly equal resulting in very little change in the peak electron density. However, if the wind effect is stronger than the diffusion effect, a decrease in peak electron density may be observed.

At night, the diffusion and the winds act together to maintain F region plasma densities. The overall effect is higher peak densities at higher altitudes because the plasma is lifted to higher altitudes where recombination rates are slower. During sunrise and sunset, the neutral winds are primarily in the east-west direction across the terminator and do not significantly affect the plasma densities, except in regions where the magnetic declination is large.

Figure 17 shows the percent increase in  $N_mF_2$  when the  $O^+/O$  collision frequency is doubled. The 0000UT (left hand plots) and 1200UT (right hand plots) are shown for all three geophysical cases. The same general changes occur for all three cases with a significant increase in  $N_mF_2$  at night and very little change in  $N_mF_2$  during the day. The largest increase is 250% and occurs in the equatorial anomalies during solar minimum December solstice (top plots) due to the combination of the HWM derived neutral winds and the configuration of the magnetic field. In regions where the neutral wind effect dominates over the diffusion effect during the day, up to a 30% decrease can be seen in the  $N_mF_2$ .

In order to investigate more closely what is occurring when the  $O^+/O$  collision frequency is doubled, mid-latitude locations at four equally spaced longitudes in both the northern and southern hemisphere were chosen and the peak electron density for the normal  $O^+/O$  collision frequency as well as for the doubled  $O^+/O$  collision frequency were plotted versus local time (Figures 18–21). The expected trend appears in all plots with the greatest increase in  $N_mF_2$  occurring at night and a minimal

$N_m F_2$  Percent Increase with a Doubled  $O^+/O$  Collision Frequency  
for All Three Geophysical Cases

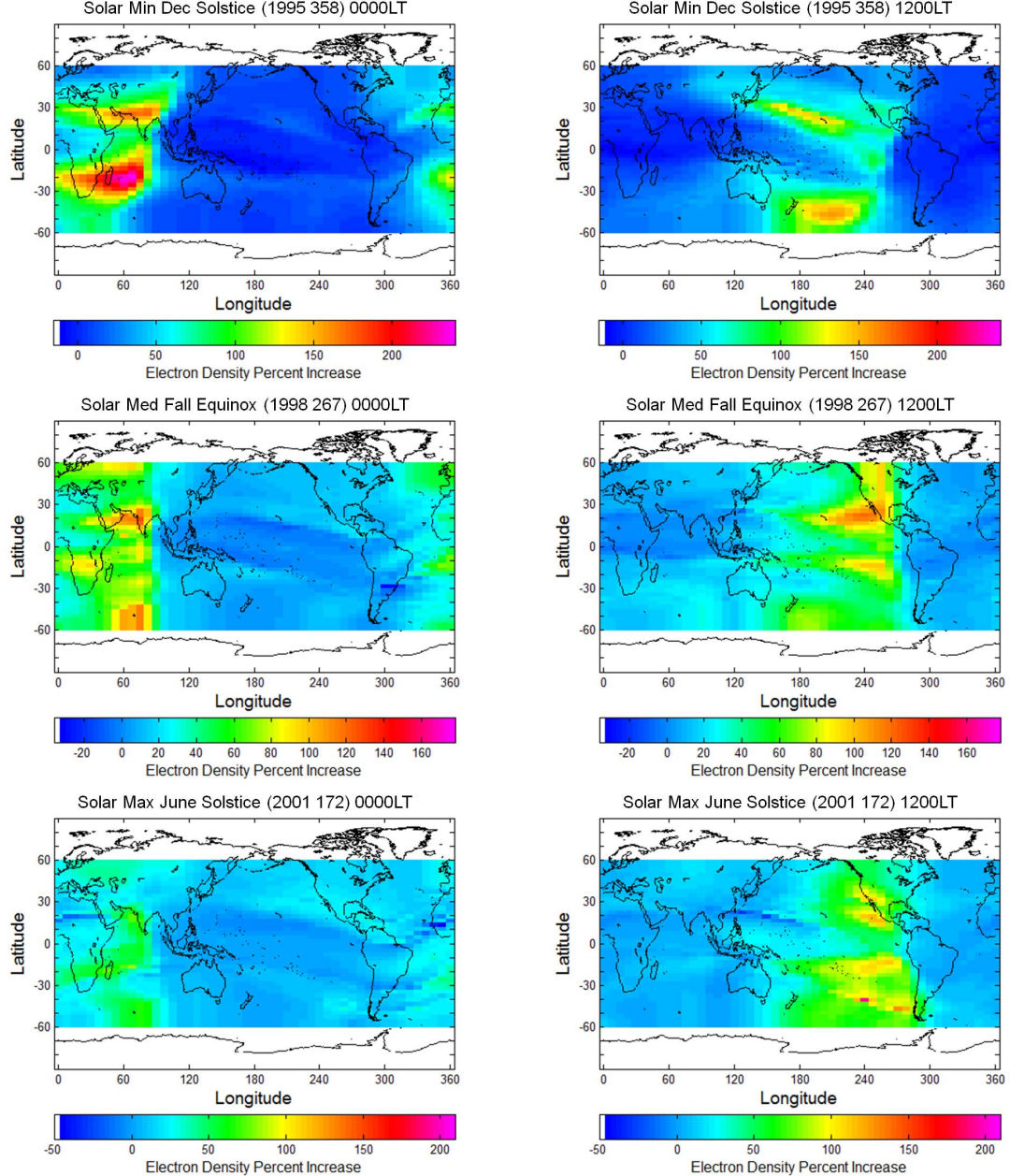


**Figure 17.**  $N_m F_2$  increase with doubled  $O^+/O$  collision frequency for all three geophysical cases (solar minimum December solstice - top, solar medium fall equinox - middle, and solar maximum June solstice - bottom) at both 0000UT (left) and 1200UT (right). The largest changes in  $N_m F_2$  occur during solar minimum. Note that the scales are different for each geophysical case

increase occurring during the day. It was found that the peak increase occurs in the early morning hours after plasma densities have had time to build up at the higher altitudes. The plasma decay at sunset was found to be slower with the doubled  $O^+/O$  collision frequency due to the reduced downward diffusion. The same general behavior is seen for all eight locations with the largest changes occurring during solar minimum December solstice and solar medium fall equinox at  $45^\circ S$   $90^\circ E$  and  $45^\circ S$   $180^\circ E$ . In these instances, the  $N_m F_2$  increases by 120–180%. The nonlinearity of the changes is a result of the complex nature of the many interactions in the ionosphere. Nighttime peak heights increased by 10–50km while daytime heights only increased a maximum of 10km.

Of interest are the double peaks, indicated by black arrows, in the  $270^\circ E$  southern hemisphere  $N_m F_2$  plots in Figure 21. The peaks occur just after sunrise and before sunset. This double peak in  $N_m F_2$  is a result of the Weddell Sea Anomaly discussed in Section 4.2. The increased efficiency of the neutral winds during the day act to bring the plasma down the field lines to regions of higher recombination and thus lowering the plasma density. At night the opposite occurs and the winds lift the plasma up the field lines resulting in enhanced densities (Horvath and Essex, 2003). As mentioned previously, the peaks are most prominent during solar minimum December solstice and solar medium fall equinox.

Table 4 gives values for the percent change in  $N_m F_2$  at local midnight, before sunrise, at local noon, and during the daytime for all eight locations. As mentioned previously, the largest changes in  $N_m F_2$  occur at night, specifically just before sunrise, and minimal changes occur during the daytime. The negative daytime values that occur at solar maximum are a result of a strong interaction with the neutral wind that overwhelms the reduced diffusion and drives the plasma down the field lines to where recombination is faster.

$N_m F_2$  vs. Local Time with a Doubled  $O^+/O$  Collision Frequency  
for All Three Geophysical Cases

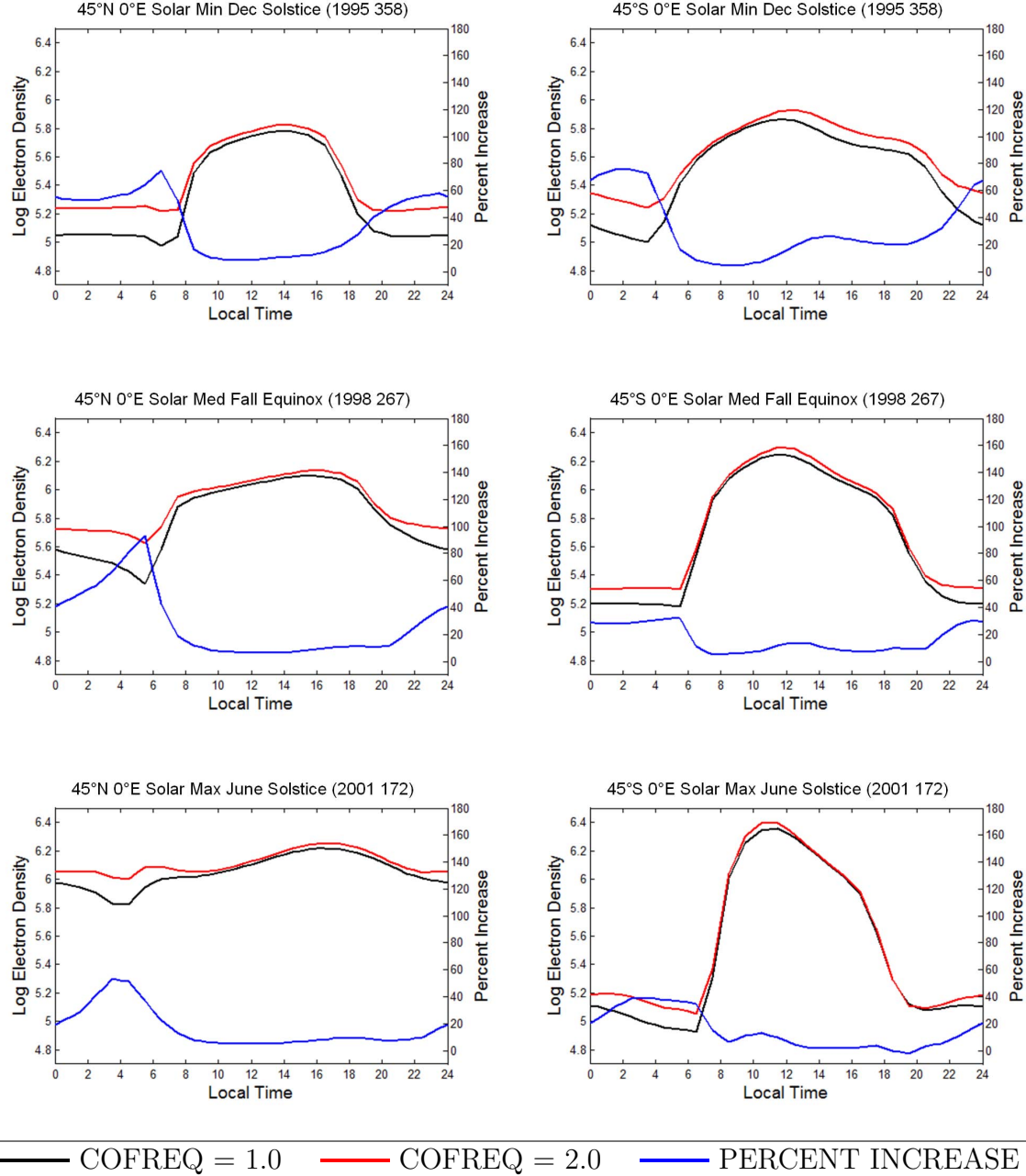
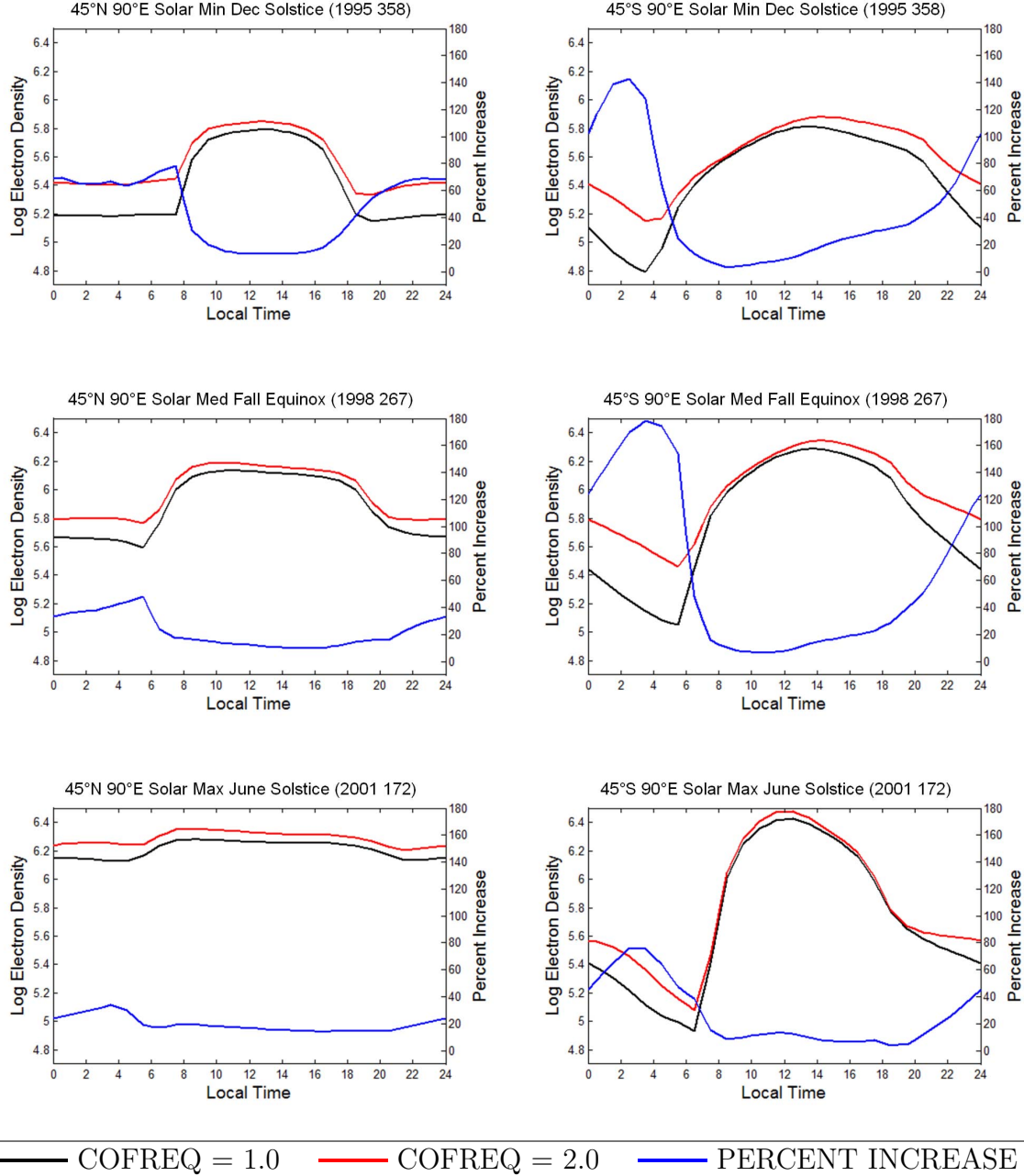


Figure 18.  $N_m F_2$  at  $0^\circ E$  with doubled  $O^+/O$  collision frequency for all three geophysical cases (solar minimum December solstice - top, solar medium fall equinox - middle, and solar maximum June solstice - bottom) at both  $45^\circ N$  (left) and  $45^\circ S$  (right). The black line is the unchanged  $O^+/O$  collision frequency, the red line is the doubled  $O^+/O$  collision frequency, and the blue line is the percent increase. The largest increases occur at night with minimal changes during the day

$N_m F_2$  vs. Local Time with a Doubled  $O^+/O$  Collision Frequency  
for All Three Geophysical Cases



**Figure 19.**  $N_m F_2$  at 90°E with doubled  $O^+/O$  collision frequency for all three geophysical cases (solar minimum December solstice - top, solar medium fall equinox - middle, and solar maximum June solstice - bottom) at both 45°N (left) and 45°S (right). The black line is the unchanged  $O^+/O$  collision frequency, the red line is the doubled  $O^+/O$  collision frequency, and the blue line is the percent increase. The largest increases occur at night with minimal changes during the day

$N_m F_2$  vs. Local Time with a Doubled  $O^+/O$  Collision Frequency  
for All Three Geophysical Cases

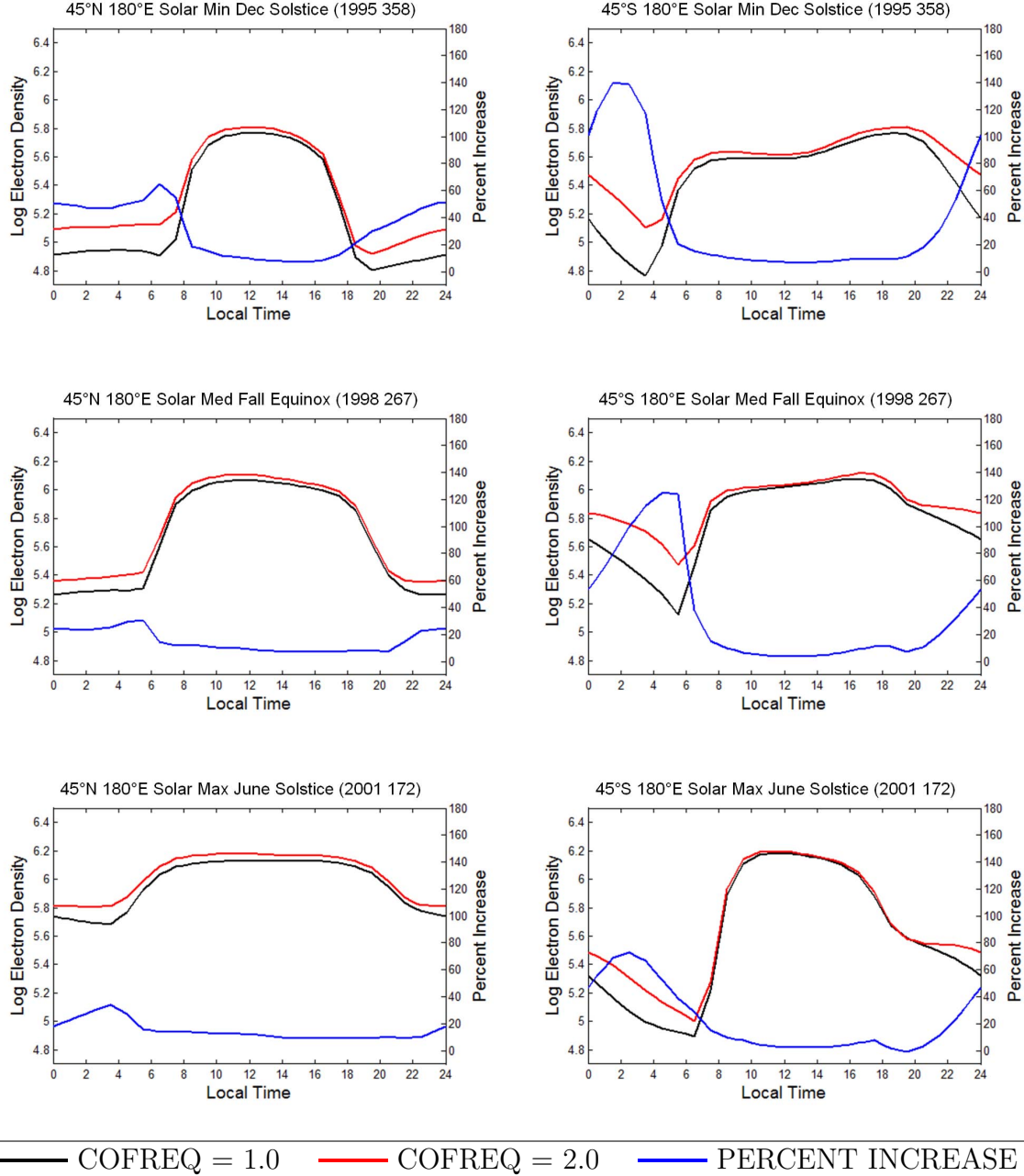


**Figure 20.**  $N_m F_2$  at 180°E with doubled  $O^+/O$  collision frequency for all three geophysical cases (solar minimum December solstice - top, solar medium fall equinox - middle, and solar maximum June solstice - bottom) at both 45°N (left) and 45°S (right). The black line is the unchanged  $O^+/O$  collision frequency, the red line is the doubled  $O^+/O$  collision frequency, and the blue line is the percent increase. The largest increases occur at night with minimal changes during the day

$N_m F_2$  vs. Local Time with a Doubled  $O^+/O$  Collision Frequency  
for All Three Geophysical Cases

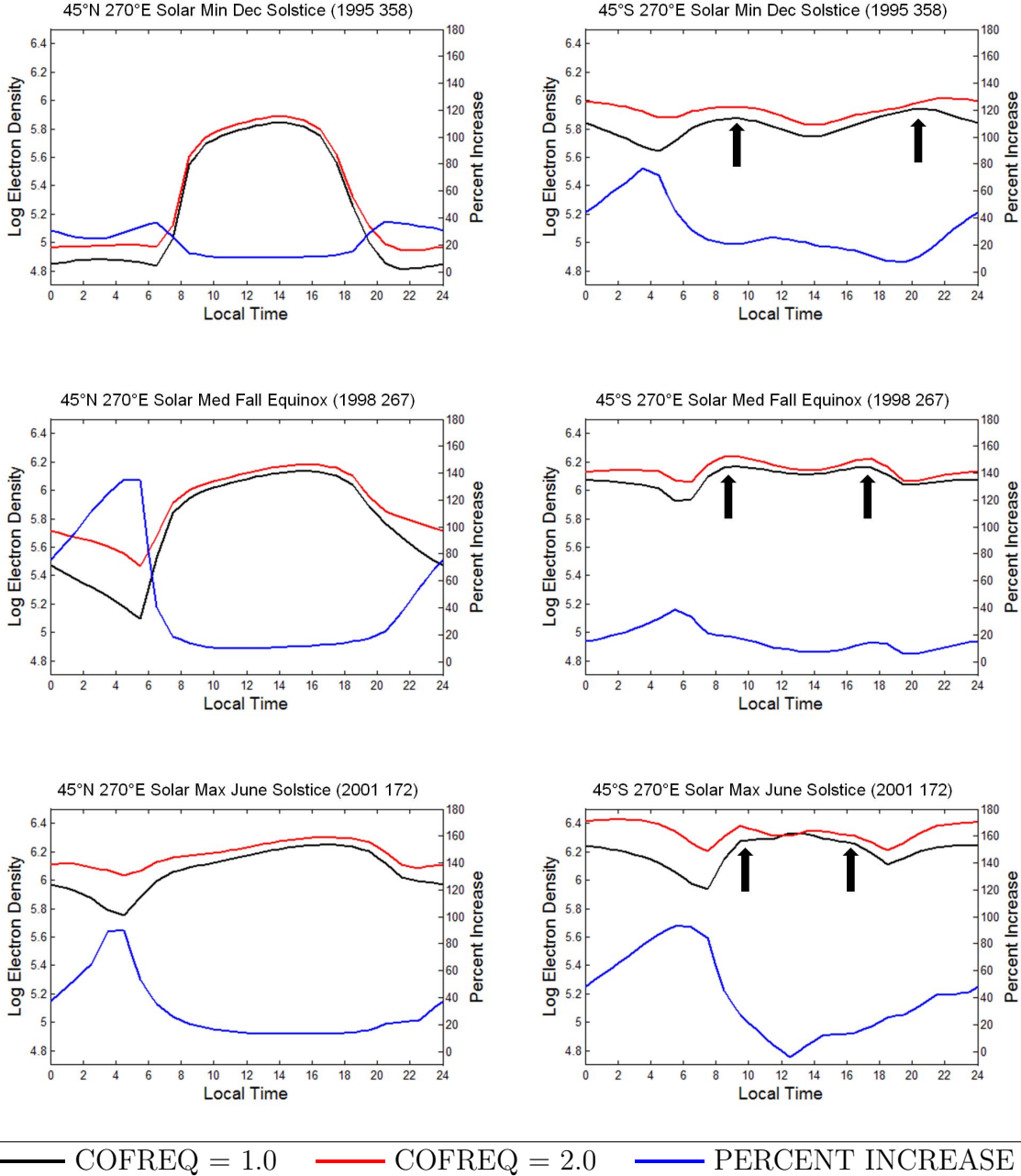


**Figure 21.**  $N_m F_2$  at 270°E with doubled  $O^+/O$  collision frequency for all three geophysical cases (solar minimum December solstice - top, solar medium fall equinox - middle, and solar maximum June solstice - bottom) at both 45°N (left) and 45°S (right). The black line is the unchanged  $O^+/O$  collision frequency, the red line is the doubled  $O^+/O$  collision frequency, and the blue line is the percent increase. The largest increases occur at night with minimal changes during the day. Double peaks due to the Weddell Sea Anomaly are indicated by black arrows

Table 4.  $N_m F_2$  increase with doubled  $O^+/O$  collision frequency for eight mid-latitude locations\*. The largest increases occur at night with minimal changes during the day. Decreases in  $N_m F_2$  (negative values) occur when the daytime wind effect overcomes the diffusion effect

		45°N			45°S		
		00LT	Pre-Sunrise	Peak	12LT	Daytime	Min
0°E	C1 <sup>a</sup>	55.76	75.08	8.75	8.59	67.70	75.61
	C2 <sup>b</sup>	40.97	93.26	6.39	6.25	29.40	31.95
	C3 <sup>c</sup>	19.33	53.28	4.86	4.81	20.36	39.40
90°E	C1	68.94	78.22	13.33	13.03	102.71	142.99
	C2	33.10	47.98	12.31	9.65	124.00	178.10
	C3	23.81	33.73	16.67	14.11	45.52	75.96
180°E	C1	50.66	65.07	9.52	7.44	101.14	140.06
	C2	24.07	30.64	8.96	6.83	53.21	124.73
	C3	17.76	33.90	11.98	9.02	46.84	72.65
270°E	C1	30.86	36.99	10.25	10.22	43.98	76.80
	C2	75.31	135.16	9.66	9.62	15.11	38.54
	C3	37.57	89.93	13.81	13.06	48.32	93.26

\* The largest global percent increase of 250% occurs in the equatorial anomalies during case 1

<sup>a</sup> Solar Minimum December Solstice

<sup>b</sup> Solar Medium Fall Equinox

<sup>c</sup> Solar Maximum June Solstice

Plasma densities below the peak were also affected by doubling the  $O^+/O$  collision frequency. The plasma in this region was significantly depleted at sunset and filled back in after sunrise. The upward motion of the plasma resulting from the combination of the increased wind effect and decreased  $O^+$  diffusion acts to deplete  $O^+$  at low altitudes with no source of replenishment. Figure 22 shows latitude versus altitude plots at  $0^\circ E$  of the percent increase in  $N_e$  due to doubling the  $O^+/O$  collision frequency during solar minimum December solstice conditions. The upper left plot is at midnight local time and shows a nearly uniform 80% decrease in  $N_e$  from 200–250 km. As sunrise approaches (upper middle and upper right plots), the depleted region is filled in as the plasma begins to move back down the field lines. By 0800LT (upper right plot) the depletion is only 10–20%. This slight depletion continues throughout the day and then as sunset approaches and the plasma begins to move to higher altitudes the depletion increases again. The bottom three plots in Figure 22 show the time sequence of the density decrease during sunset from 1800LT–2000LT. The increase in densities above the peak can also be seen in these plots. These results are consistent for all three geophysical cases.

#### 4.4 Zonal Winds

The thermospheric low latitude zonal winds are calculated in the IPM using the HWM. These winds force the plasma to move up and down the magnetic field lines and result in magnetic field induced vertical drifts. The general trend of the low latitude ( $5^\circ N$ – $5^\circ S$ ) HWM zonal winds (binned every hour by local time and averaged over all  $K_p$  and  $F_{10.7}$ ) is westward during the day and eastward at night with only slight variations in magnitude and time of wind direction switch (Figure 23). *Liu et al.* (2006), also evaluated the HWM zonal winds for different levels of geomagnetic activity and  $F_{10.7}$  values, however, the variation in the results remains small. The

$N_e$  Percent Increase at  $0^\circ$ E with a Doubled  $O^+/O$  Collision Frequency for Solar Minimum December Solstice

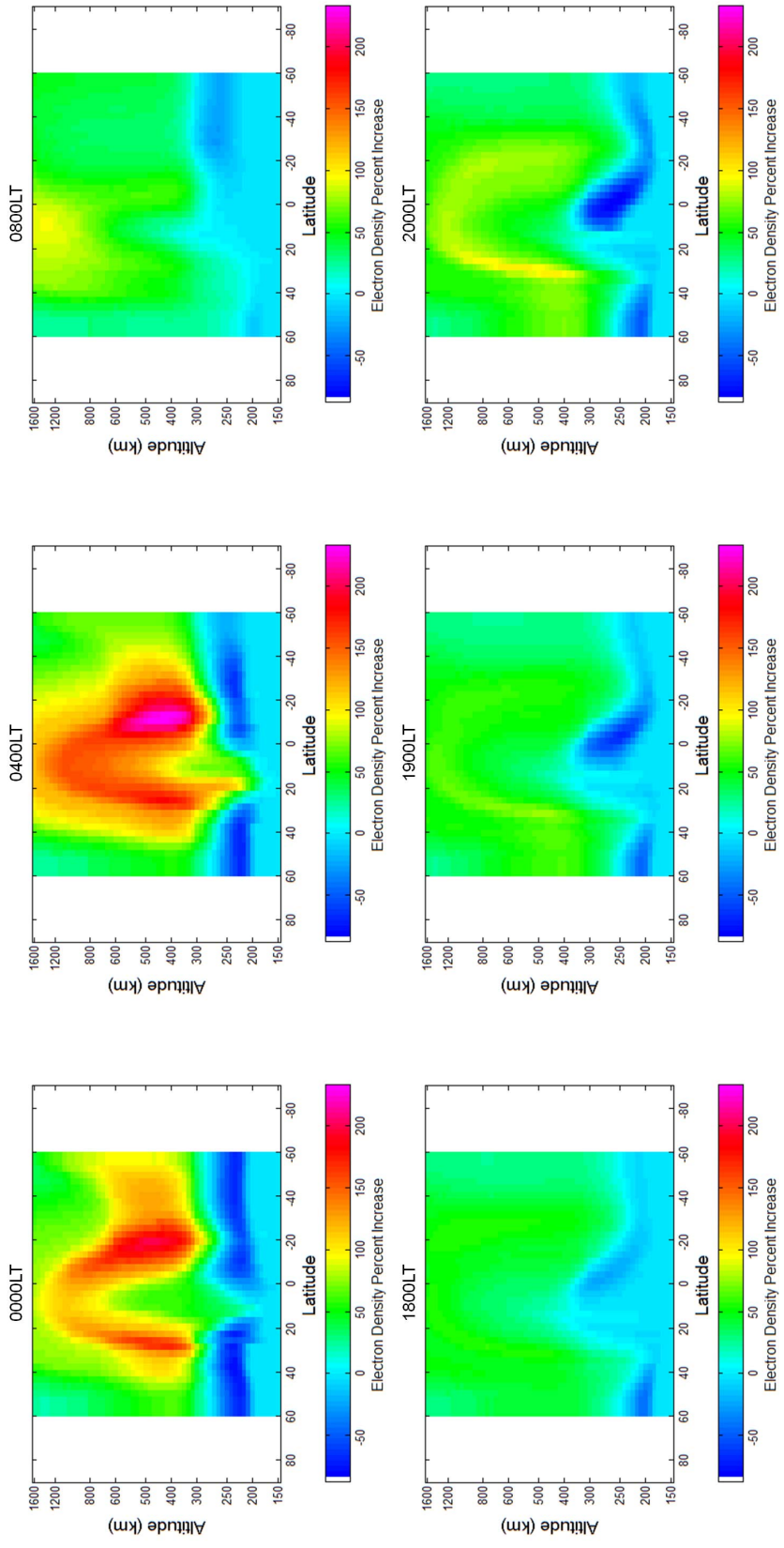


**Figure 22.**  $N_e$  increase at  $0^\circ$ E with doubled  $O^+/O$  collision frequency during solar minimum December solstice. This time sequence shows how the plasma increases at upper altitudes and decreases at low altitudes overnight with a doubled  $O^+/O$  collision frequency. After sunrise, the winds and diffusion oppose each other resulting in much smaller changes to the density structure. As sunset occurs, the diffusion and winds once again work in combination to deplete the lower altitude plasma and increase the upper altitude plasma

HWM is a climatological model and cannot accurately represent the global thermospheric wind pattern on a day to day basis and is instead an averaged representation leading to uncertainties in the model output.

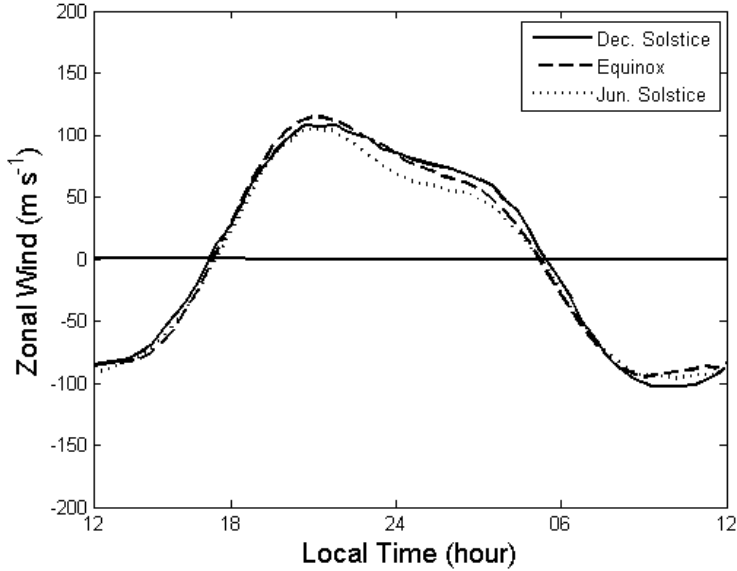


**Figure 23.** HWM derived zonal thermospheric winds averaged over  $K_p$  and  $F_{10.7}$  at 400km for all three geophysical conditions. The winds are westward (negative values) during the day and eastward (positive values) at night with very little seasonal dependence (Adapted from *Liu et al. (2006)*)

In its simplest version, the earth's magnetic field can be represented by a tilted and offset dipole with respect to earth's axis of rotation. The offset dipole field results in a non-perpendicular intersection of a plane of magnetic field lines and the earth's surface over certain geographic locations. Figure 24 shows a simple schematic of this effect. The offset dipole field and the daytime westward thermospheric winds cause upward plasma drifts near  $45^\circ E$  (Madagascar) and downward plasma drifts near  $225^\circ E$  (Southeast Pacific) during the daytime; these drifts are reversed at night.

In addition to the offset dipole, the east-west tilt of the field lines also leads to magnetic field induced vertical drifts. Figure 25 shows the HWM-derived zonal

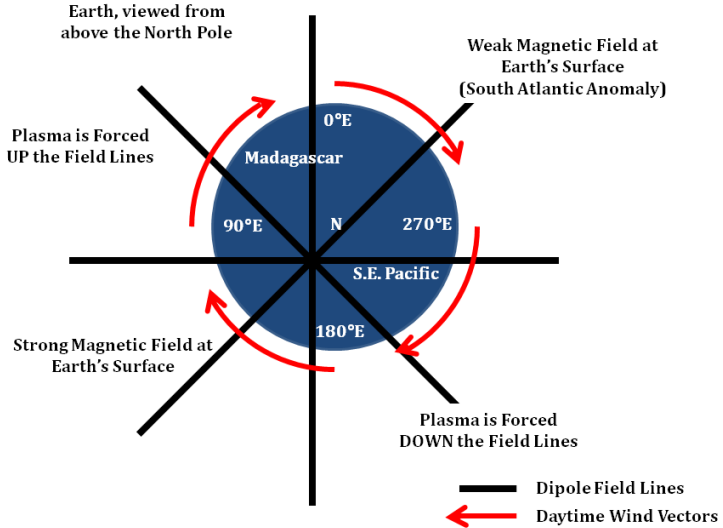


**Figure 24.** Schematic of an offset dipole magnetic field and the daytime low-latitude thermospheric winds as viewed from above the northern geographic pole. The zonal winds force the ions along the field lines resulting in upward drifts near Madagascar and downward drifts in the Southeast Pacific

winds for the three geophysical conditions used in this project. The times chosen (1000UT and 1800UT during solar minimum and solar medium, and 0000UT and 0500UT during solar maximum) correspond to the time of the maximum change in TEC and  $N_e$ . Eastward winds are depicted as positive values and westward winds are negative values; in general, the daytime winds are westward and the nighttime winds are eastward as was seen in Figure 23. The black lines are magnetic field lines (and the geomagnetic equator) as calculated by the IGRF. The IGRF is a numerical model that calculates earth's magnetic field based on observations collected by satellites at magnetic observatories and during magnetic surveys (*Finlay et al.*, 2010). The lowest order solution of the IGRF is a dipole field. Because of this magnetic field structure, the zonal wind has components both parallel and perpendicular to the field lines. The parallel component will cause the ions to move along the field lines; if the parallel component of the wind is toward the equator, upward drifts will occur. Downward drifts will occur with a parallel component that is poleward.

For example, in the upper left plot in Figure 25, the westward flow over South Africa causes the ions to move along the field line toward the equator, which results in an upward vertical drift. In the upper right plot, the westward flow over the Southeast Pacific causes the ions to move along the field line toward the pole resulting in a downward vertical drift. These magnetic field induced drifts are especially important for the solar maximum June solstice case (bottom two plots) in the region of the South Atlantic Anomaly (SAA) which will be discussed further below.

For this comparison, the IPM was first run with the HWM-derived zonal winds and then with the zonal winds set to zero to evaluate the effects of an uncertain zonal wind field on the magnetic field induced vertical drifts. Although all of the magnetic field induced drifts are shut off when the HWM zonal winds are forced to zero in the comparison runs, the  $\vec{E} \times \vec{B}$  drifts are unaffected. In the IPM, each parameter is determined using separate climatological models and the zonal wind model is not coupled to the electric field model. Therefore, forcing the zonal winds to zero does not affect the  $\vec{E} \times \vec{B}$  drift that is calculated within the model.

The most significant results from this comparison occur during the day near Madagascar ( $45^\circ E$ ) and in the Southeast Pacific Ocean near  $270^\circ E$ . The largest changes in TEC occur over Madagascar at 1000UT (1300LT) and over the Southeast Pacific at 1800UT (1100LT) during both solar minimum December solstice and solar medium fall equinox conditions. The largest changes in TEC during solar maximum June solstice occur in the Eastern Pacific and the South Atlantic. All of the changes are directly related to the complicated structure of the IGRF derived magnetic field and to the changes in the magnetic field induced vertical drifts of the plasma.

When the zonal winds are set to zero, the TEC near Madagascar decreases a maximum of 45% (12 TECU) during solar minimum and 50% (40 TECU) during solar medium (Figures 26 and 27). This occurs because the magnetic field induced

### 300km HWM Zonal Winds for All Three Geophysical Cases

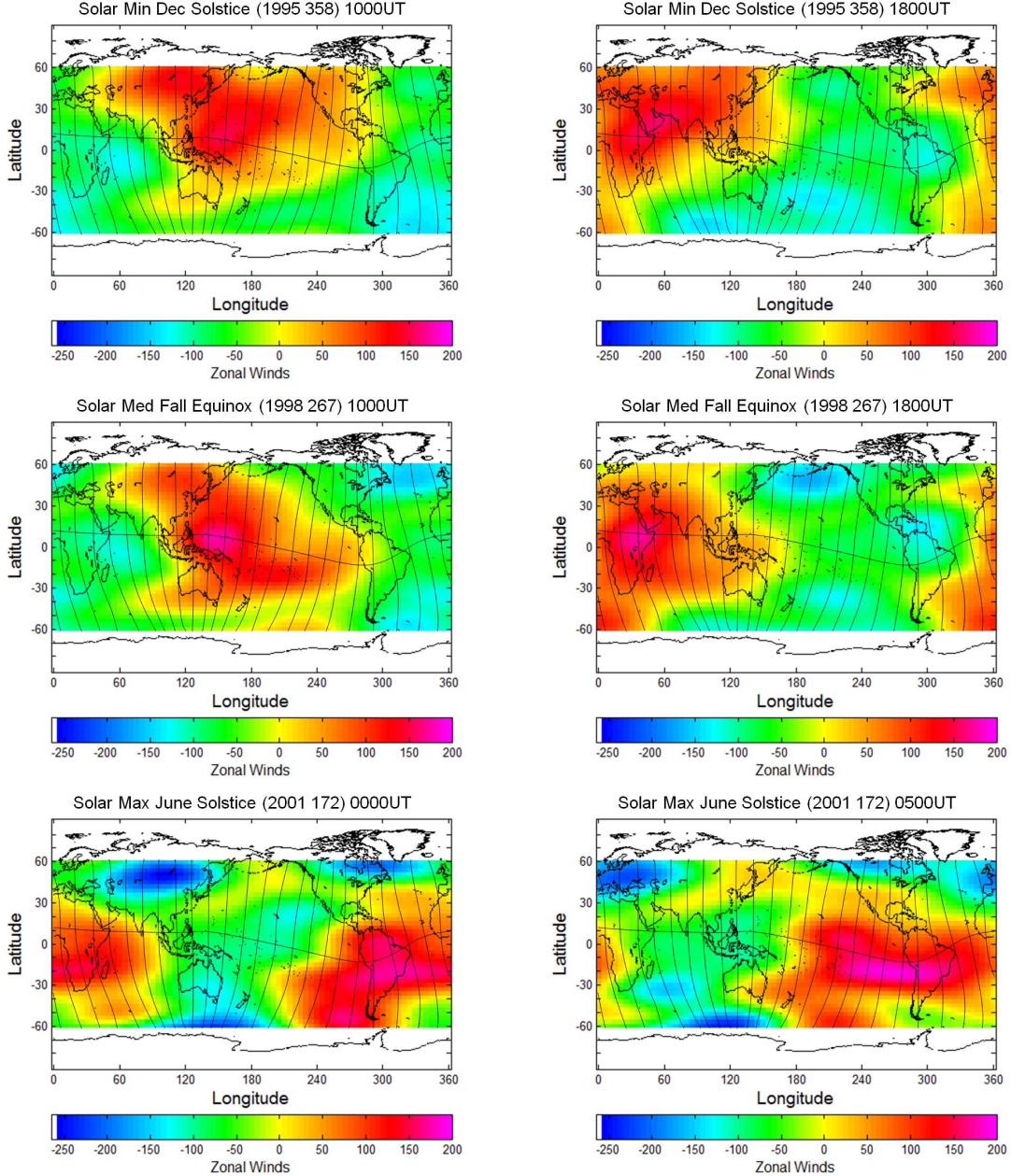


**Figure 25.** HWM zonal winds at 300km for all three geophysical cases at 1000UT (left) and 1800UT (right) for solar minimum (top) and solar medium (middle) and at 0000UT (left) and 0500UT (right) for solar maximum (bottom). Positive values are eastward and negative values are westward. The black lines are magnetic field lines as calculated by the IGRF. The combination of the zonal winds and the east-west tilt of the field lines creates vertical plasma drifts

upward plasma drift is stopped during the day keeping the plasma at lower altitudes where recombination is faster. The electron density decrease at  $45^{\circ}E$  is also shown in the latitude versus altitude plots in Figures 26 and 27. Densities decrease above the  $F_2$  peak due to the lack of the upward drift and increase slightly below the peak as more plasma is kept at lower altitudes.

TEC over the Southeast Pacific increases up to 85% (10 TECU) during solar minimum and 57% (16 TECU) during solar medium as seen in Figures 28 and 29. In this region, setting the zonal winds to zero shuts off the downward plasma drift keeping the plasma at higher altitudes where recombination rates are slower. Once again, the latitude versus altitude plots show additional information about the altitude at which the changes in electron density are occurring. The bottom right difference plot shows an increase in electron densities above the  $F_2$  peak and a decrease in electron densities below the peak. This is the opposite from what is occurring over Madagascar because in this region the magnetic field induced daytime drift is opposite that of Madagascar.

The most significant changes in TEC that occurred during solar maximum (Figure 30) were different than for the other two cases. Although the decrease near Madagascar occurs for this case with a maximum decrease of 50% (29 TECU) at 0600UT, the increase in the Southeast Pacific does not occur. The reason is partly due to encroaching eastward winds in the HWM at the time when the maximum changes are expected. This encroaching eastward wind occurs due to the short amount of daylight during this period (southern hemisphere winter). The TEC over the Eastern Pacific decreases a maximum of 50 TECU (90%) and the TEC over the South Atlantic increases 75 TECU (400%) (Figure 30). Both of these changes occur at night (around 2200LT) when the eastward winds are strongest over these locations (Figure 25).

The decrease over the Eastern Pacific is a result of the interaction of the magnetic field and the eastward zonal winds creating an upward drift in this region. Shutting

## TEC and $N_e$ with Adjusted Zonal Winds for Solar Minimum December Solstice

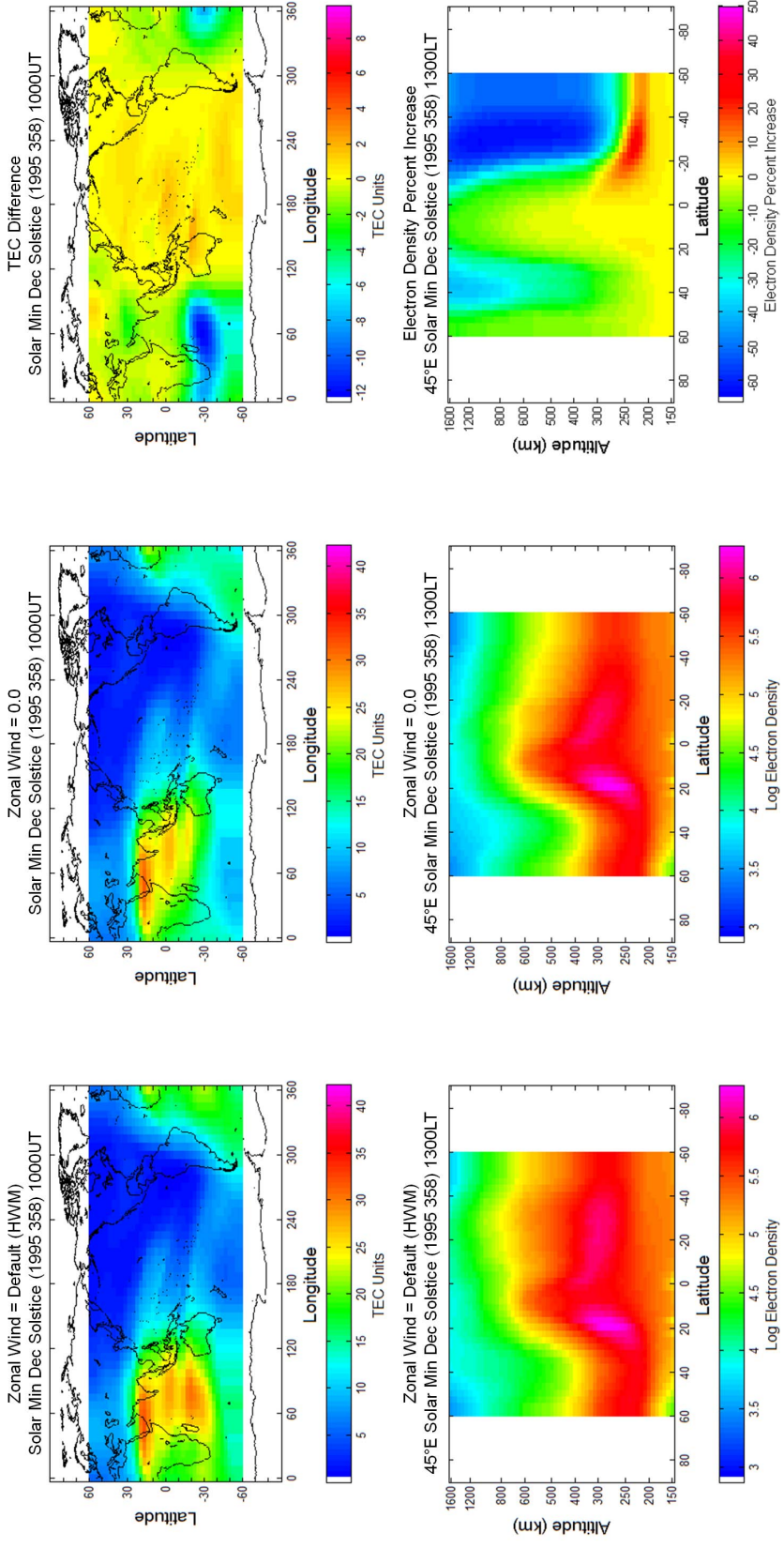


Figure 26. TEC and  $N_e$  with adjusted zonal winds for case 1 (solar minimum December solstice) at 1000UT (1300LT). TEC is plotted on top and  $N_e$  is plotted on the bottom. The left plot is with the HWM calculated zonal winds, the middle plot is with the zonal winds set to zero, and the right plot is the difference. Setting the zonal winds to zero results in a 12 TECU decrease over Madagascar (45°E)

## TEC and $N_e$ with Adjusted Zonal Winds for Solar Medium Fall Equinox

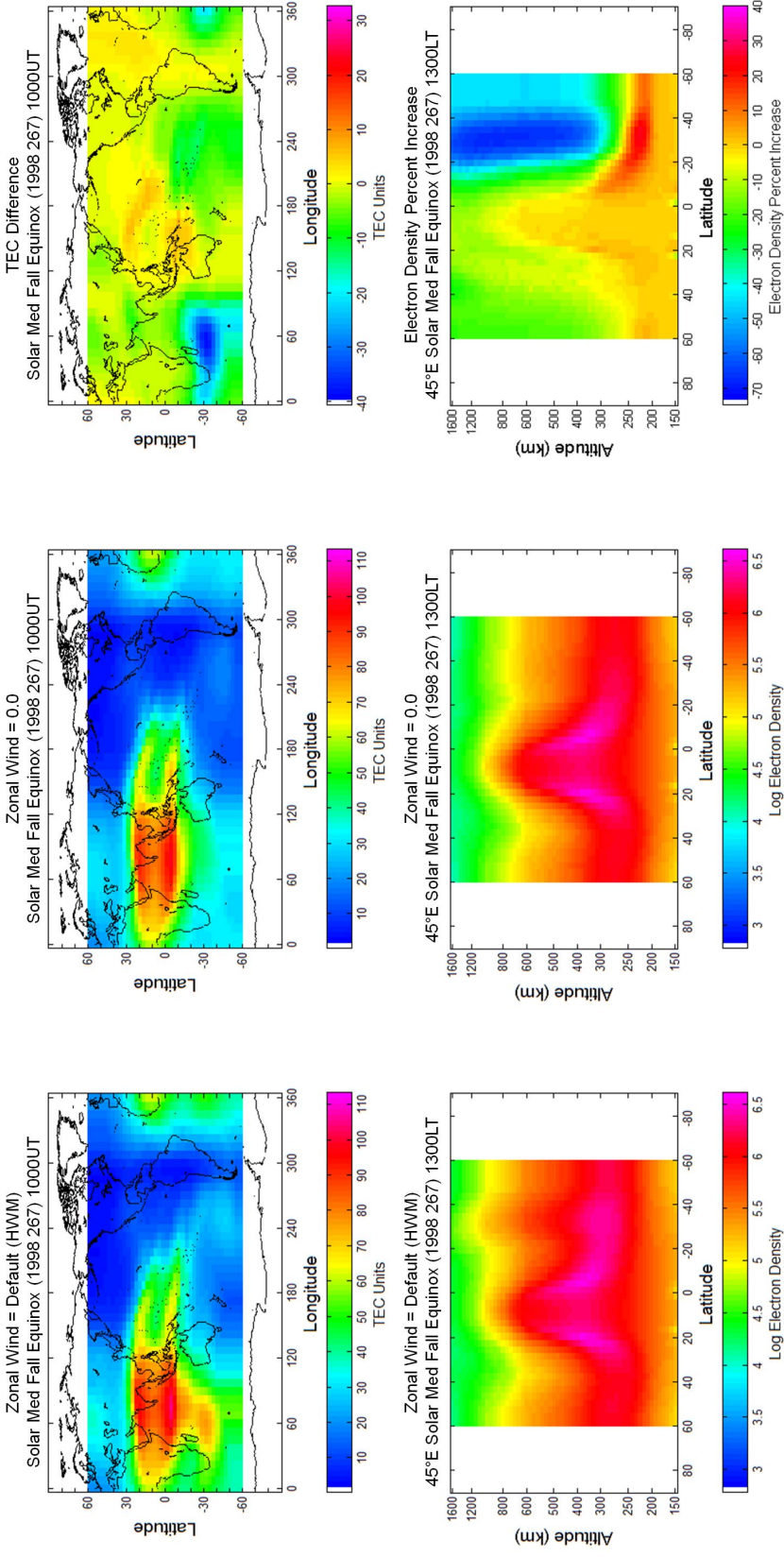


Figure 27. TEC and  $N_e$  with adjusted zonal winds for case 2 (solar medium fall equinox) at 1000UT (1300LT). TEC is plotted on top and  $N_e$  is plotted on the bottom. The left plot is with the HWM calculated zonal winds, the middle plot is with the zonal winds set to zero, and the right plot is the difference. Setting the zonal winds to zero results in a 40 TECU decrease over Madagascar ( $45^\circ E$ )

## TEC and $N_e$ with Adjusted Zonal Winds for Solar Minimum December Solstice

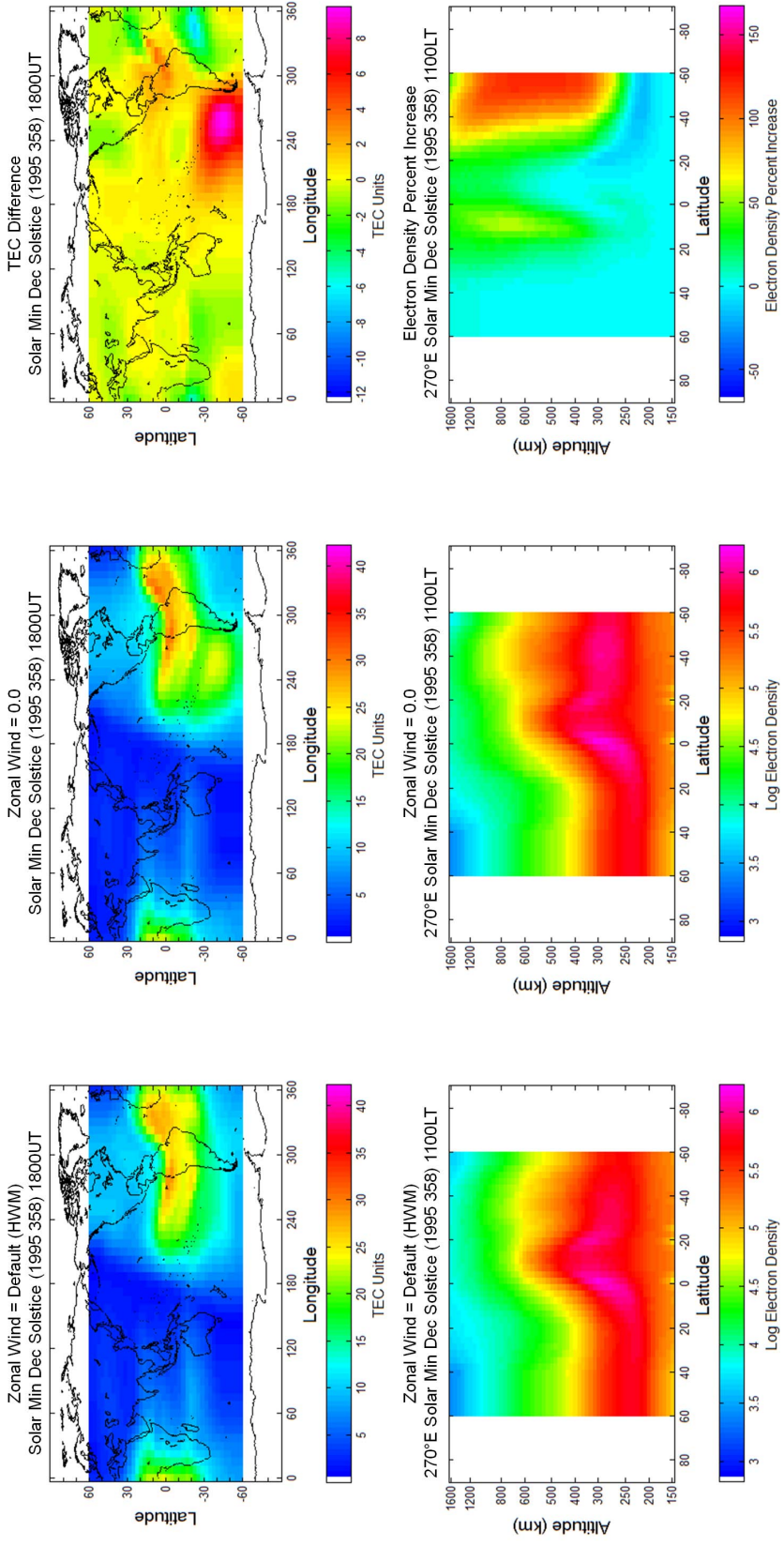


Figure 28. TEC and  $N_e$  with adjusted zonal winds for case 1 (solar minimum December solstice) at 1800UT (1100LT). TEC is plotted on top and  $N_e$  is plotted on the bottom. The left plot is with the HWM calculated zonal winds, the middle plot is with the zonal winds set to zero, and the right plot is the difference. Setting the zonal winds to zero results in a 10 TECU increase over the Southeast Pacific (270°E)

## TEC and $N_e$ with Adjusted Zonal Winds for Solar Medium Fall Equinox

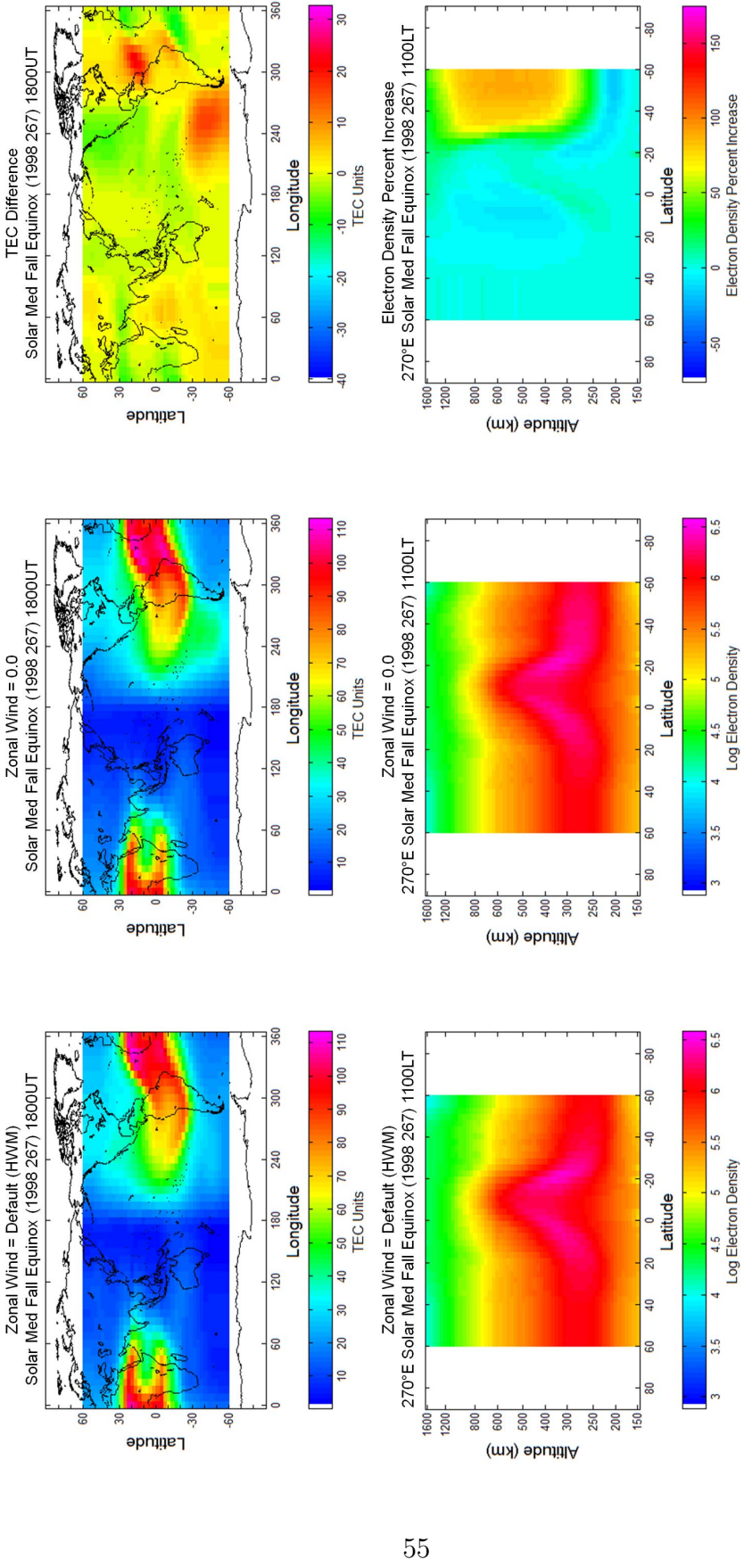


Figure 29. TEC and  $N_e$  with adjusted zonal winds for case 2 (solar medium fall equinox) at 1800UT (1100LT). TEC is plotted on top and  $N_e$  is plotted on the bottom. The left plot is with the HWM calculated zonal winds, the middle plot is with the zonal winds set to zero, and the right plot is the difference. Setting the zonal winds to zero results in a 16 TECU increase over the Southeast Pacific ( $270^\circ E$ )

## TEC with Adjusted Zonal Winds for Solar Maximum June Solstice

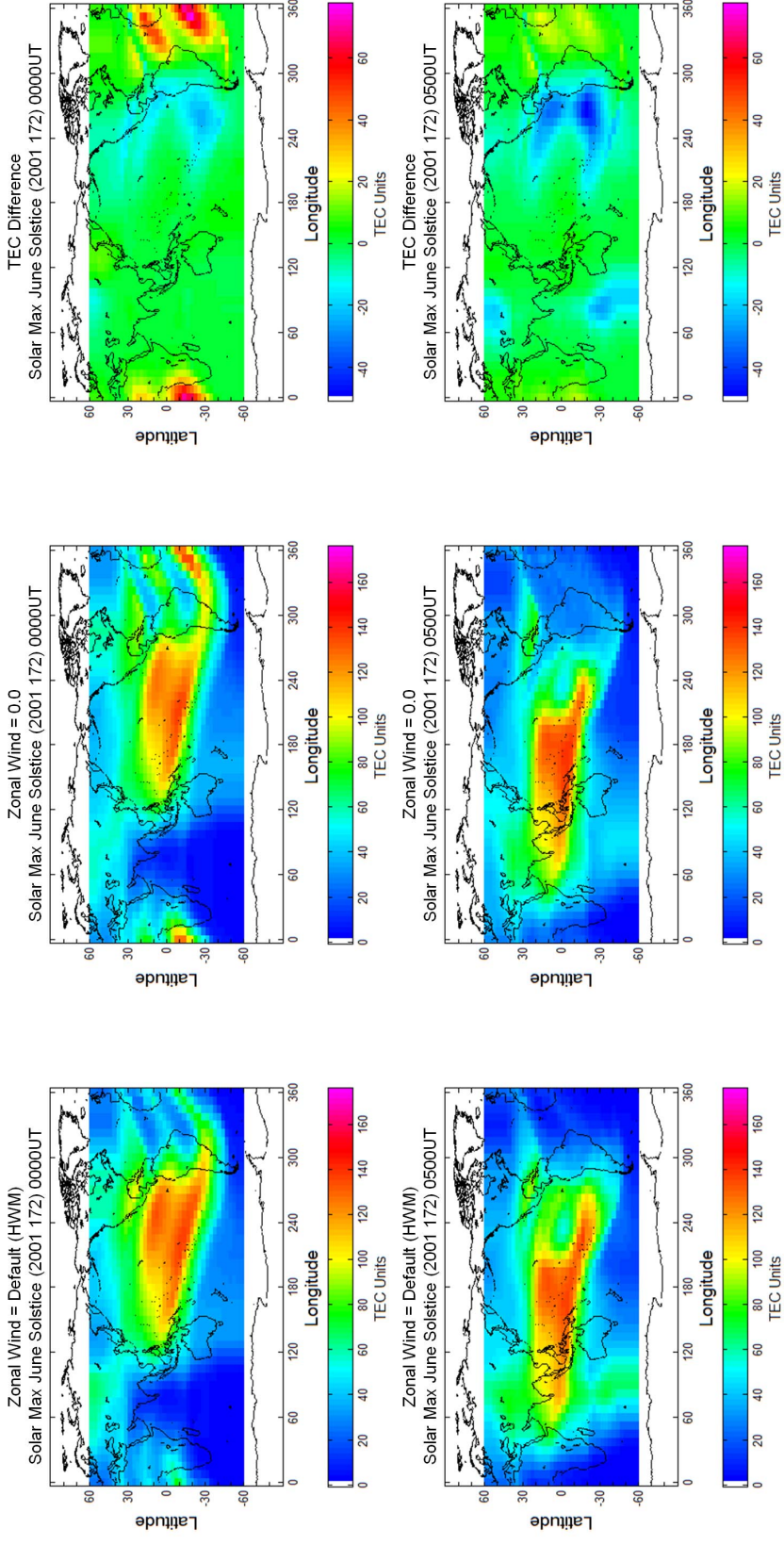


Figure 30. TEC with adjusted zonal winds for case 3 (solar maximum June Solstice) at 0000UT (top) and 0500UT (bottom). The left plot is with the HWM calculated zonal winds, the middle plot is with the zonal winds set to zero, and the right plot is the difference. Setting the zonal winds to zero results in a 75 TECU increase over the South Atlantic (top right) and a 45 TECU decrease over the Eastern Pacific (bottom right)

off the winds stops the upward drift resulting in decreased plasma densities. The increase over the South Atlantic is a result of a complicated magnetic field. The magnetic field vertical drifts create regions of converging and diverging winds which results in enhancements and depletions in the plasma density. For this case, the result of setting the zonal winds to zero is a significant increase in the equatorial anomalies in the South Atlantic (upper right hand plot, Figure 30).

#### 4.5 Daytime Production

Daytime production mechanisms include photoionization, chemical reactions, secondary electron production, and impact ionization as discussed in Chapter II. Secondary electron production is an additional important production mechanism that is difficult to accurately model. This leads to uncertainties in the magnitude of the total daytime production in the ionosphere. Previous studies found that daytime production in a physics-based model needed to be increased by a factor of 1.8 (the ‘primo fix’) to account for the contribution of secondary electron production. More recent studies by *Zhu et al.* (2006) using a larger set of observational data have suggested that this value is too high and that realistic production levels are obtained when the production multiplication factor varies linearly as a function of  $F_{10.7}$  as shown in Figure 31.

For this comparison, the baseline runs of the IPM were done with the original 1.8 multiplication factor while the comparison runs were done with a multiplication factor that varied linearly as a function of  $F_{10.7}$  (Figure 31). The maximum change to the production occurred during solar maximum ( $F_{10.7} = 220$ ) with the production multiplication factor reduced from 1.8 to 1.2—a decrease of 33% in overall production. The minimum change occurred during solar minimum ( $F_{10.7} = 80$ ) with a new production multiplication factor of 1.5, which is a decrease of 17% in overall production.

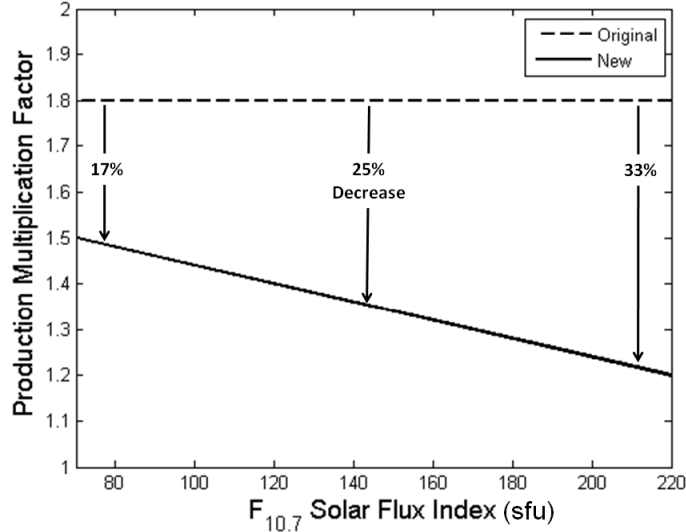


**Figure 31.** The decrease in daytime production multiplication factor varies linearly as a function of  $F_{10.7}$ . The largest change to the production factor occurred for high  $F_{10.7}$  values and the smallest change occurred for low  $F_{10.7}$  values

Higher solar flux during solar maximum results in higher production due to both photoionization as well as to secondary electrons. This is why the solar maximum photoionization production is only increased by 20% (production multiplication factor of 1.2) to account for secondary electron production while during solar minimum it is increased by 50% (production multiplication factor of 1.5). For example, TEC during solar minimum can be as low as 25 TECU; increasing this by 50% results in a 12.5 TECU increase. Solar maximum TEC is as large as 100 TECU; the 20% solar maximum increase results in a 20 TECU increase which is 7.5 TECU higher than the solar minimum increase. Therefore the higher number of energetic electrons during solar maximum are still being accounted for with the linear variation of the production multiplication factor.

The results of this comparison show that the magnitude of the maximum decrease in TEC during the day is directly proportional to the change in the production multiplication factor. The smallest change in TEC occurred during solar minimum while

solar maximum had the largest change in TEC. Figure 32 shows the TEC plots for solar minimum December solstice. The difference plot shows a 7 TECU maximum decrease occurring at 1400LT in the equatorial anomalies. Figures 33 and 34 show the same plots for both solar medium fall equinox and solar maximum June solstice, respectively. The maximum decrease during solar medium fall equinox was 30 TECU while during solar maximum June solstice the maximum decrease was 50 TECU. Additionally, all three geophysical cases had very little or no change in TEC at night when production due to photoionization and secondary electron production decrease. Table 5 gives a summary of the maximum change in TEC for all three geophysical cases.

**Table 5. TEC decrease with decreased daytime production. The maximum change in TEC was directly proportional to the change in the production multiplication factor**

	Solar Minimum	Solar Medium	Solar Maximum
Original Production Factor	1.8	1.8	1.8
New Production Factor	1.5	1.35	1.2
Production Factor Decrease	17%	25%	33%
TECU Decrease	7	30	50
TEC Percent Decrease	17%	27%	33%

## 4.6 Nighttime $\vec{E} \times \vec{B}$ Drift

Photoionization decreases significantly at night and results in a significant decay of the ionosphere. During this time, the ionosphere is primarily controlled by loss mechanisms and plasma transport. At low latitudes, the nighttime  $\vec{E} \times \vec{B}$  drift is downward due to the westward electric field. This drift brings the ions to lower altitudes where recombination rates are higher resulting in the depletion of the ionosphere. Downward drifts that are too fast will result in nighttime densities that are too low while drifts that are too slow will result in densities that are too high due to the higher

## TEC with Decreased Daytime Production for Solar Minimum December Solstice

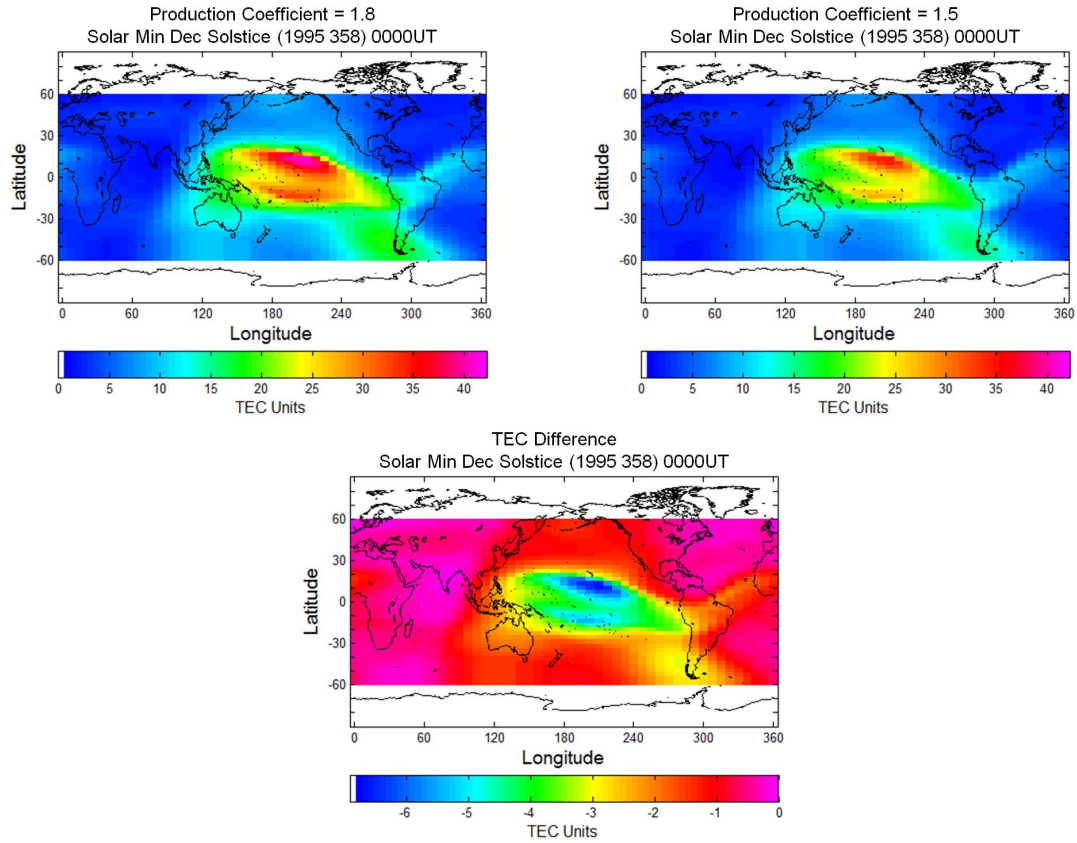


**Figure 32.** TEC with decreased daytime production for case 1 (solar minimum December solstice) at 0000UT. The top left plot is with a 1.8 multiplication factor for daytime production, the top right plot is with a 1.5 multiplication factor, and the bottom plot is the difference. The 17% decrease in the production multiplication factor resulted in a maximum decrease of 7 TECU (17%) in the equatorial anomalies

## TEC with Decreased Daytime Production for Solar Medium Fall Equinox

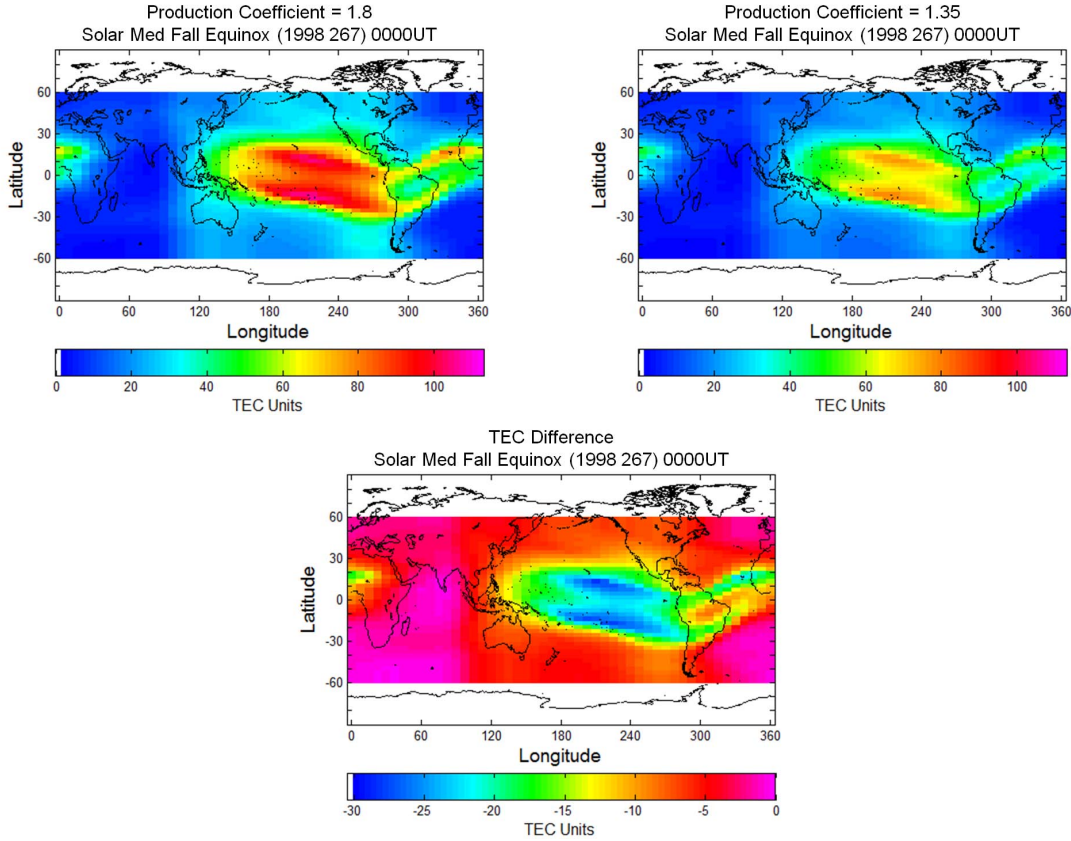


Figure 33. TEC with decreased daytime production for case 2 (solar medium fall equinox) at 0000UT. The top left plot is with a 1.8 multiplication factor for daytime production, the top right plot is with a 1.35 multiplication factor, and the bottom plot is the difference. The 25% decrease in the production multiplication factor resulted in a maximum decrease of 30 TECU (27%) in the equatorial anomalies

### TEC with Decreased Daytime Production for Solar Maximum June Solstice

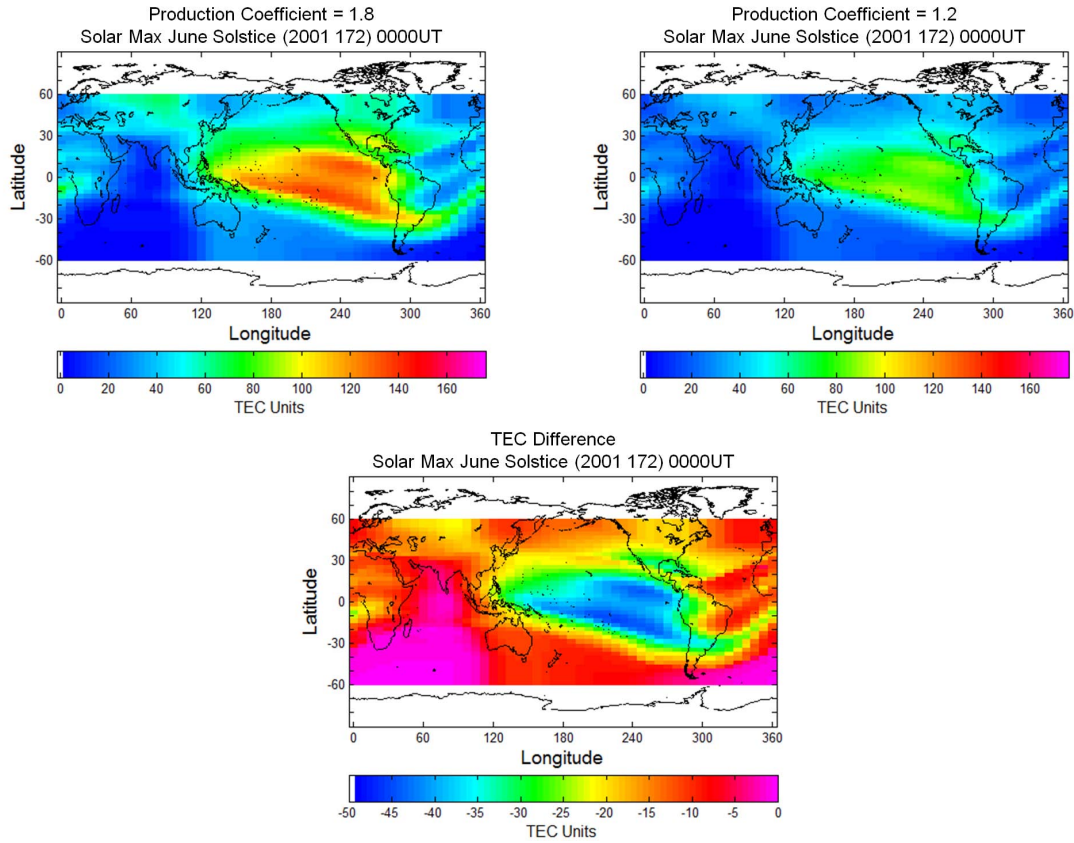
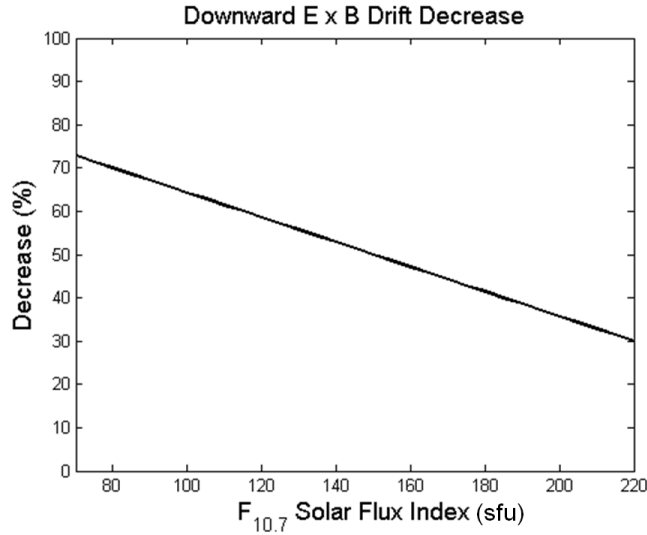


Figure 34. TEC with decreased daytime production for case 3 (solar maximum June solstice) at 0000UT. The top left plot is with a 1.8 multiplication factor for daytime production, the top right plot is with a 1.2 multiplication factor, and the bottom plot is the difference. The 33% decrease in the production multiplication factor resulted in a maximum decrease of 50 TECU (33%) in the equatorial anomalies

recombination at low altitudes. Slowing the downward nighttime  $\vec{E} \times \vec{B}$  drift allows the ions to remain at higher altitudes where recombination rates are slower. In this comparison, the downward nighttime  $\vec{E} \times \vec{B}$  drift is decreased linearly as a function of  $F_{10.7}$  (Figure 35) to investigate the resulting changes to the nighttime densities.



**Figure 35.** Decrease in downward  $\vec{E} \times \vec{B}$  drift varies linearly as a function of  $F_{10.7}$ . The largest change occurred for low and the smallest change occurred for large  $F_{10.7}$  values

For all three geophysical cases, the largest absolute increase in nighttime TEC occurs around 0100LT–0200LT while the largest percent increase in TEC occurs at 0500LT (due to the much smaller densities at this time). The largest changes for solar minimum December solstice and solar medium fall equinox occurred in the region of the SAA (Figures 36 and 37). The magnetic field is weakest in this region resulting in a fast initial  $\vec{E} \times \vec{B}$  drift ( $\vec{u}_E \propto E/B$ ). Decreasing this fast drift results in a larger overall change than in the regions where the drift is slower. For solar maximum June solstice, the largest changes occurred over and just to the west of South America (Figure 38) due to the magnetic field configuration and neutral wind pattern in this region.

For the solar minimum December solstice case, the  $\vec{E} \times \vec{B}$  drift was decreased by 70% resulting in a maximum 8 TECU increase (480% increase) over the SAA as seen in the right hand plot of Figure 36. A slight decrease in TEC (less than 1.5 TECU) also occurs during the day due to the residual effects propagating into the daytime sector. The bottom plots in Figure 36 show the  $45^\circ E$  altitude structure of the electron density at 0500LT (0300UT). The increase in low latitude densities can be seen in the right hand plot. This plot shows a maximum 700% increase in electron density occurring over the geomagnetic equator at approximately  $300\text{km}$ . This plot also shows that the changes occur only in the low latitudes— $30^\circ N$ – $20^\circ S$  geographic latitude as this is where the  $\vec{E} \times \vec{B}$  drift is most significant. Also of interest is the decrease in electron densities around  $200\text{km}$  in the southern hemisphere. The decrease is occurring because the plasma is not allowed to move to lower altitudes to replenish the depleted plasma. The effect is stronger in the southern (summer) hemisphere due to the winter anomaly.

The same general results were obtained for the solar medium fall equinox case as for solar minimum. The maximum increase in TEC occurred over the SAA; this increase can be easily seen in the top row of plots in Figure 37. The right hand plot shows that the maximum increase in TEC was almost 40 TECU, corresponding to a 630% increase. The small decrease during the day can also be seen in this plot. The plots showing the altitude structure of the electron density (Figure 37, bottom row) show the same overall changes as for the previous case. Increases in low latitude electron density of up to 900% result from decreasing the downward nighttime  $\vec{E} \times \vec{B}$  drift by approximately 55%.

The results for the solar maximum June solstice case are slightly different than the previous two cases due to the significant increase in photoionization during this period. In addition, this period also had the smallest decrease (30%) to the downward

nighttime  $\vec{E} \times \vec{B}$  which results in smaller changes to the TEC and  $N_e$ . The top right hand plot in Figure 38 shows that the maximum increase in TEC is 30 TECU (160% increase) while the bottom right hand plot shows the maximum increase in electron densities with altitude is 250%. The effect of the winter anomaly can also be seen in this plot with the northern (summer) hemisphere having a larger decrease in electron densities below the peak.

Another interesting way to examine the results of this comparison is to look at the same local time for all locations. Figure 39 shows both the absolute difference (left) and percent increase (right) in TEC at 0500LT for all three cases. For the solar minimum and solar medium cases, this plot shows that the largest changes occur over the SAA as previously stated. However, these plots also show that the location of the largest changes moves from the SAA during solar minimum December solstice to the East Asia/Pacific Ocean region during solar maximum June solstice. This change can be attributed to the configuration of the magnetic field and the differences in field-aligned drifts that result from the changing thermospheric winds with season.

## 4.7 Four-Wave Tidal Influence

A ‘longitudinal wave number four pattern’ of enhanced TEC was shown to exist in the low latitude equatorial anomalies by *Immel et al.* (2006). This wave number four pattern is created by longitudinal variations in atmospheric tides in the troposphere that propagate upward into the E region ionosphere resulting in a corresponding modulation of the zonal electric field and the vertical plasma drifts. These variations manifest in the ionosphere as a wave-like pattern of TEC enhancements and depletions at equatorial and low latitudes. *Scherliess et al.* (2008) studied the longitudinal variability of the low latitude TEC using TOPEX observations and showed the local time, seasonal, solar cycle, and geomagnetic activity dependence of this pattern.

### TEC and $N_e$ with Decreased Downward $\vec{E} \times \vec{B}$ Drift for Solar Minimum December Solstice

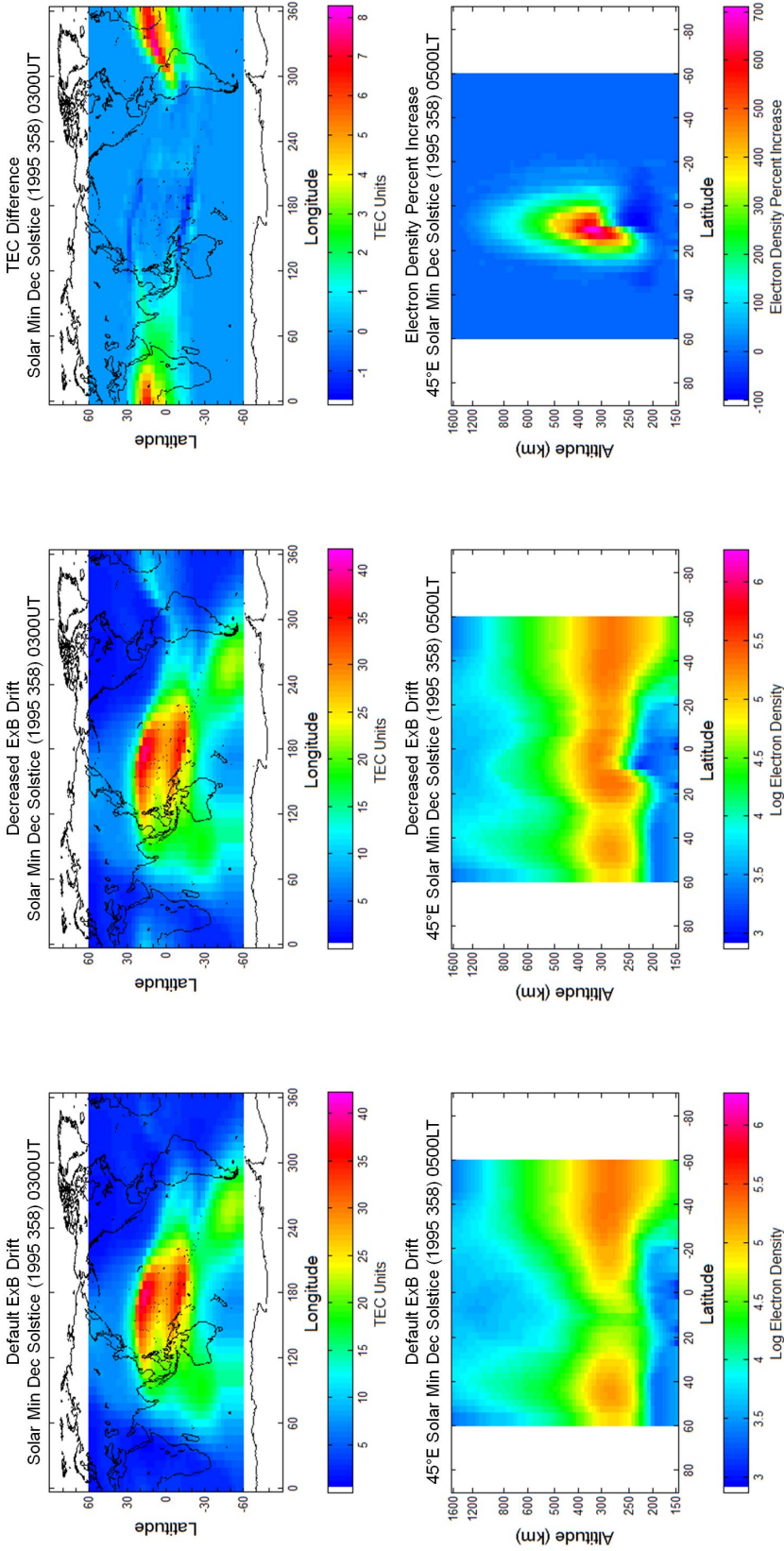


Figure 36. TEC and  $N_e$  at  $45^\circ\text{E}$  with decreased downward  $\vec{E} \times \vec{B}$  drift for case 1 (solar minimum December solstice) at 0300UT/0500LT. TEC is plotted on top and  $N_e$  is plotted on the bottom. The left plot is with the default  $\vec{E} \times \vec{B}$  drift, the middle plot is with the decreased downward  $\vec{E} \times \vec{B}$  drift, and the right plot is the difference (top) and percent increase (bottom). TEC increases a maximum of 8 TECU over the SAA

## TEC and $N_e$ with Decreased Downward $\vec{E} \times \vec{B}$ Drift for Solar Medium Fall Equinox

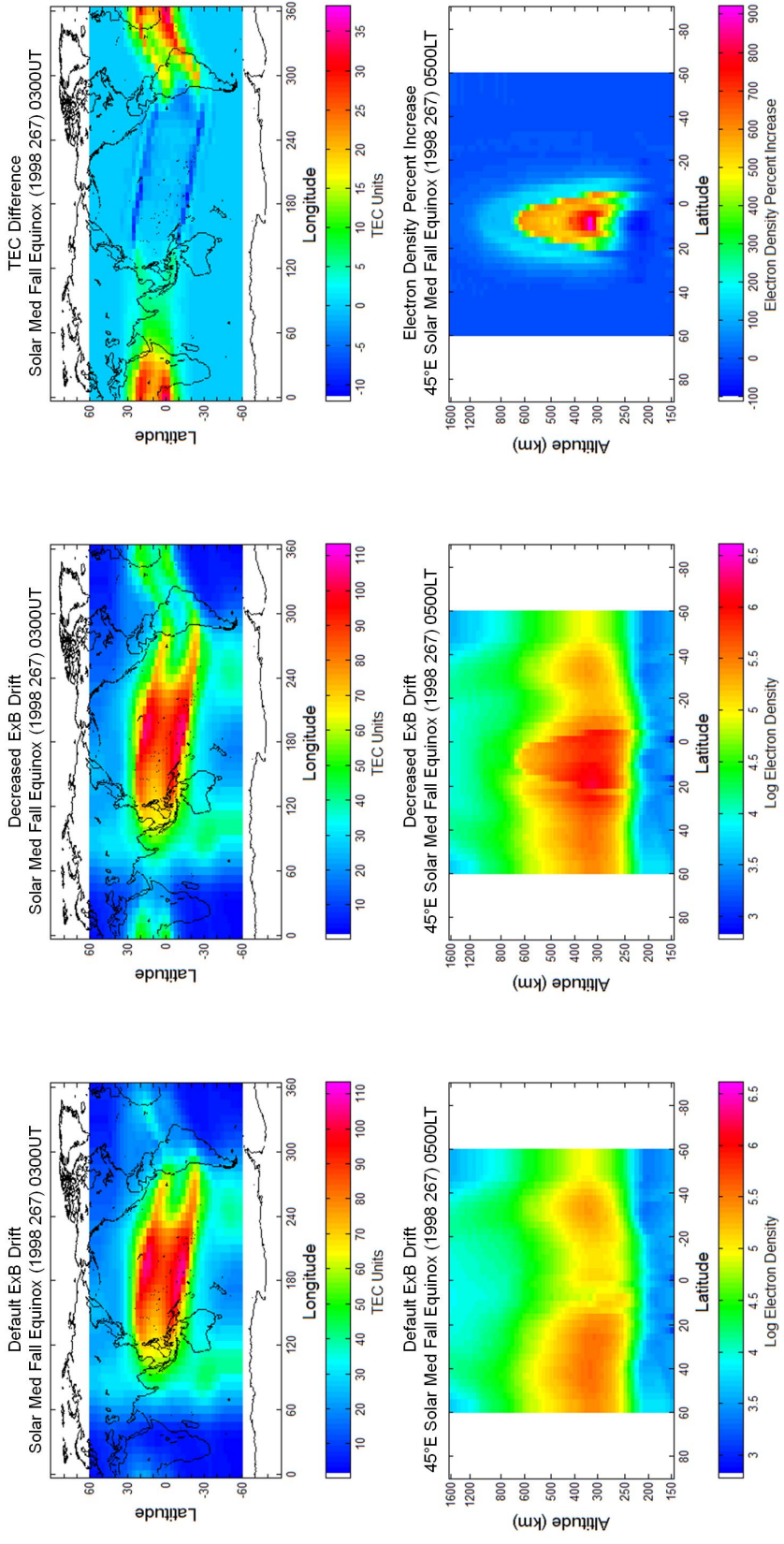


Figure 37. TEC and  $N_e$  at  $45^\circ$ E with decreased downward  $\vec{E} \times \vec{B}$  drift for case 2 (solar medium fall equinox) at 0300UT/0500LT. TEC is plotted on top and  $N_e$  is plotted on the bottom. The left plot is with the default  $\vec{E} \times \vec{B}$  drift, the middle plot is with the decreased downward  $\vec{E} \times \vec{B}$  drift, and the right plot is the difference (top) and percent increase (bottom). TEC increases a maximum of 40 TECU over the SAA.

## TEC and $N_e$ with Decreased Downward $\vec{E} \times \vec{B}$ Drift for Solar Maximum June Solstice

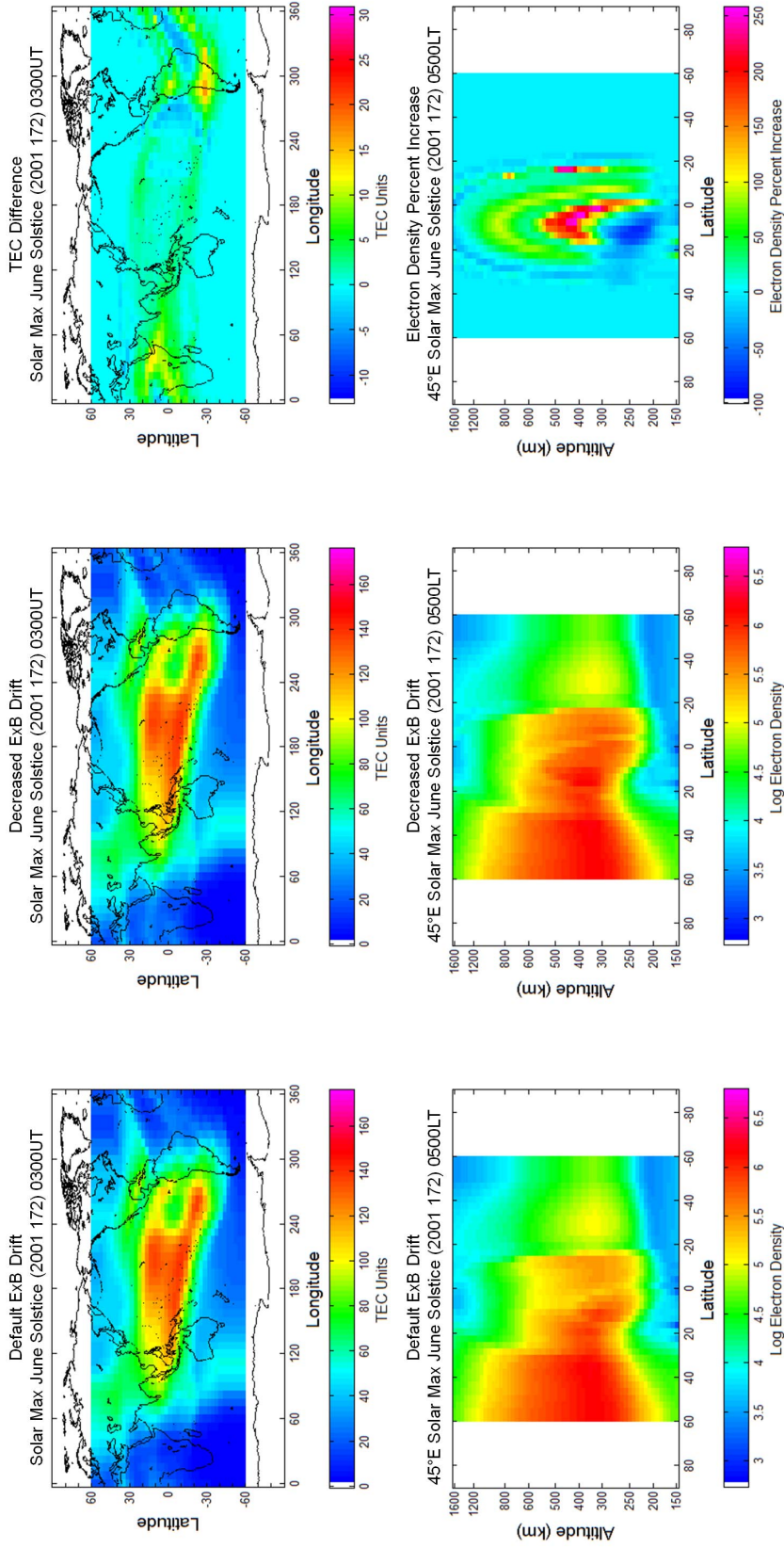


Figure 38. TEC and  $N_e$  at  $45^\circ\text{E}$  with decreased downward  $\vec{E} \times \vec{B}$  drift for case 3 (solar maximum June solstice) at 0300UT/0500LT. TEC is plotted on top and  $N_e$  is plotted on the bottom. The left plot is with the default  $\vec{E} \times \vec{B}$  drift, the middle plot is with the decreased downward  $\vec{E} \times \vec{B}$  drift, and the right plot is the difference (top) and percent increase (bottom). TEC increases a maximum of 30 TECU over the Western South America

## TEC with Decreased Downward $\vec{E} \times \vec{B}$ Drift for All Three Geophysical Cases

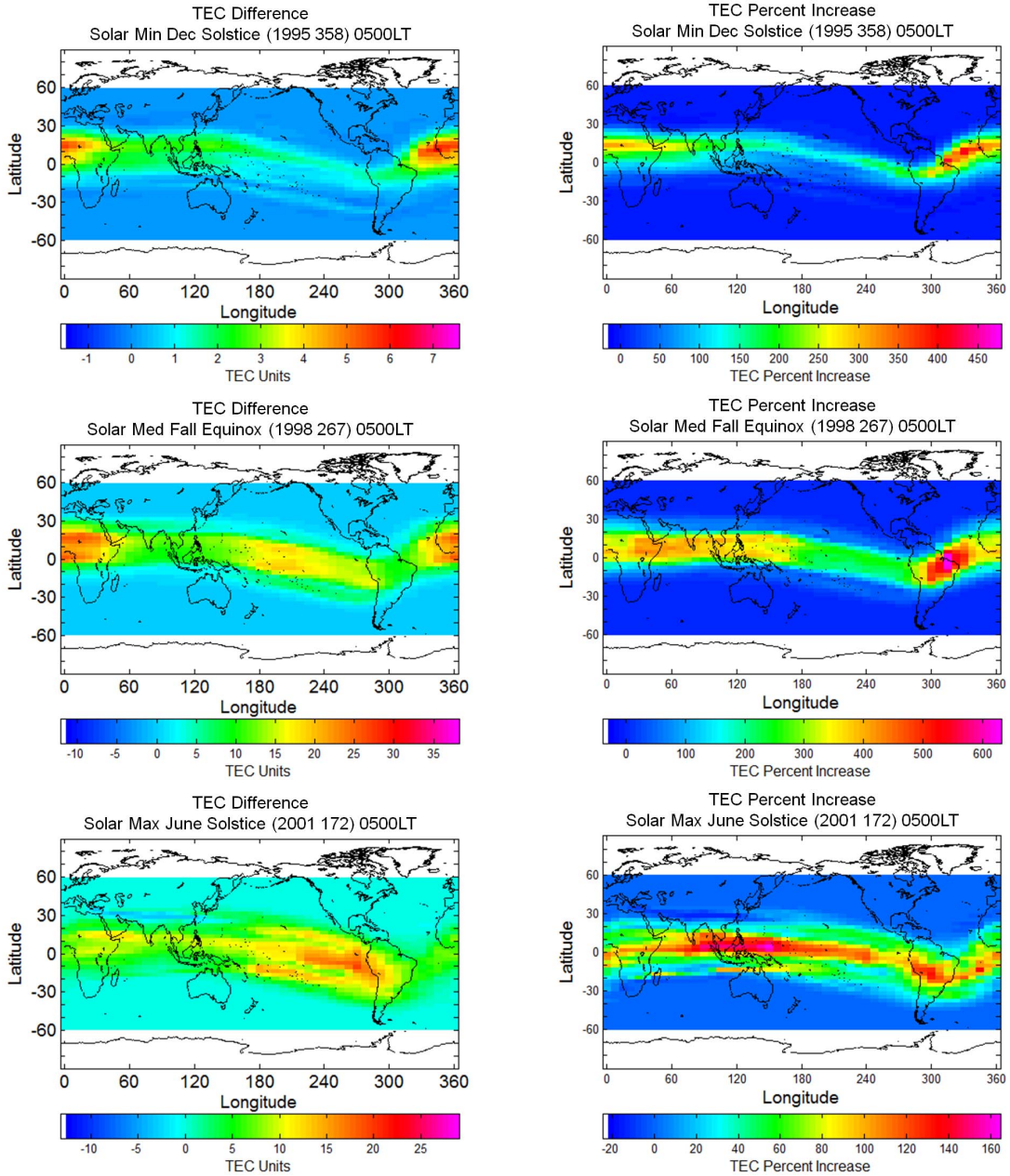


Figure 39. TEC increase with decreased downward  $\vec{E} \times \vec{B}$  drift for all three geophysical cases (solar minimum December solstice - top, solar medium fall equinox - middle, and solar maximum June solstice - bottom). The plots show the changes in TEC at 0500LT for all geographic locations. The area of the maximum change shifts from the SAA to the Pacific Ocean from case 1 to case 3. Note that the scales are different for each geophysical case

It was found that the wave number four pattern is created during the day during equinox and June solstice and is present but not well-defined during December solstice (*Scherliess et al.*, 2008). It was also found that the pattern is not dependent on solar cycle or geomagnetic activity.

Because the wave number four pattern is created by tides in the troposphere, this forcing can only be simulated in an ionospheric model. This was done in the IPM by modulating the vertical  $\vec{E} \times \vec{B}$  drift as a function of longitude based on previous work done by USU (*Schunk*, 2010). This modulation increases the  $\vec{E} \times \vec{B}$  drift at certain longitudes and decreases it at other longitudes.

Including tidal forcing in this manner resulted in a distinctive pattern of enhancements and depletions of TEC and 400km  $N_e$  in the equatorial anomalies (Figures 40 and 41). The enhancements are centered at longitudes of 15E, 110E, 200E, and 290E and the depletions centered at longitudes of 60E, 155E, 245E, and 335E this pattern does not migrate with time. Each enhancement and depletion spans approximately 40° of longitude and is symmetric in location (though not magnitude) about the geometric equator for all three geophysical cases.

Figures 40 and 41 show the TEC and 400km  $N_e$ , respectively, for solar minimum December solstice. Both figures are at 1300LT, which is when the largest changes in each parameter occur. The top left plot in each figure shows the model output without the  $\vec{E} \times \vec{B}$  drift modulation while the top right plot is the model output with the tidal forcing included. Although these two plots look nearly identical, subtracting one grid from the other shows the enhancements and depletions that result from the modulation (bottom plot). For this case, the TEC increases a maximum of 23% over Northern Africa and decreases a maximum of 14% over the Northeast Pacific. Changes in the 400km  $N_e$  are similar with a maximum increase of 44% and a decrease of 24% in the same locations. Of interest is that the northern hemisphere

enhancements and depletions are slightly greater than the southern hemisphere ones. This is again due to the winter anomaly and the resulting asymmetries in electron densities.

Because the differences in the plots of TEC and  $400\text{km } N_e$  without tidal forcing and with tidal forcing (e.g. between Figures 40 and 41) are difficult to distinguish, these plots are not shown for the solar medium and solar maximum cases. Instead, Figure 42 shows only the plots of the percent change in TEC and  $400\text{km } N_e$  for both cases. As mentioned previously and seen clearly in these plots, the pattern of enhancements and depletions is similar across solar cycle and season with only a change in the magnitude of the enhancements and depletions. Table 6 lists the maximum changes in TEC and  $400\text{km } N_e$  for all three cases. The smallest percent change occurs during solar maximum June solstice (bottom row of Figure 42), which is due to the higher overall plasma densities present during these conditions. Again, the effects of the winter anomaly can be seen in the asymmetric magnitudes in the June solstice case (bottom row) with the southern hemisphere having larger changes than the northern hemisphere; for the fall equinox case, the magnitudes of the enhancements and depletions are fairly symmetric across the geomagnetic equator.

**Table 6. Maximum percent change in TEC and  $400\text{km } N_e$  at 1300LT. The largest changes occur during solar minimum December solstice while the smallest changes occur during solar maximum June solstice**

	TEC		$400\text{km } N_e$	
	Maximum % Increase	Maximum % Decrease	Maximum % Increase	Maximum % Decrease
Case 1	23	14	44	24
Case 2	21	16	34	28
Case 3	13	11	19	18

### TEC with Tidal Forcing Included for Solar Minimum December Solstice

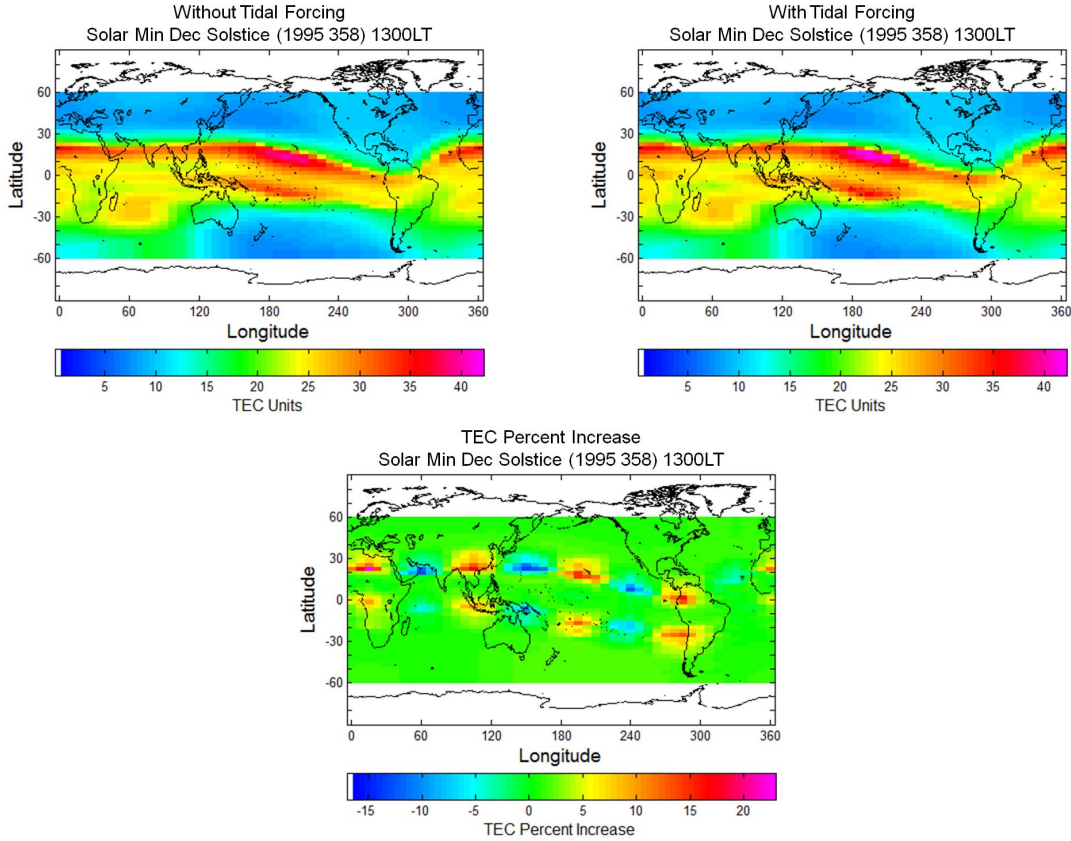
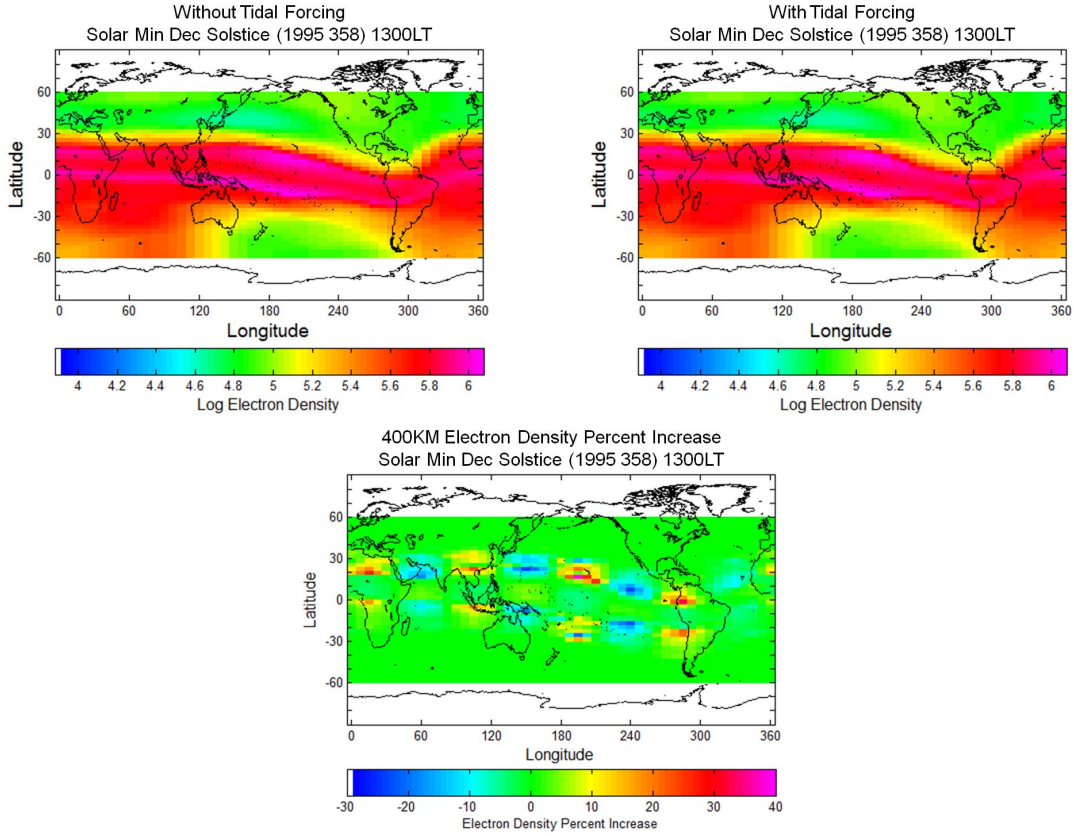


Figure 40. TEC with tidal forcing for case 1 (solar minimum December solstice). The plots are for a fixed local time (1300LT). The top left plot is the default run, the top right plot is with tidal forcing included, and the bottom plot is the difference. Modulating the  $\vec{E} \times \vec{B}$  drift results in enhancements and depletions in the low latitude TEC

$N_e$  at 400km with Tidal Forcing Included for Solar Minimum December Solstice



**Figure 41.**  $N_e$  at 400km with tidal forcing for case 1 (solar minimum December solstice). The plots are for a fixed local time (1300LT). The top left plot is the default run, the top right plot is with tidal forcing included, and the bottom plot is the difference. Modulating the  $\vec{E} \times \vec{B}$  drift results in enhancements and depletions in the low latitude 400km  $N_e$

TEC and  $400\text{km}$   $N_e$  Percent Increase with Tidal Forcing Included  
for Two Geophysical Cases

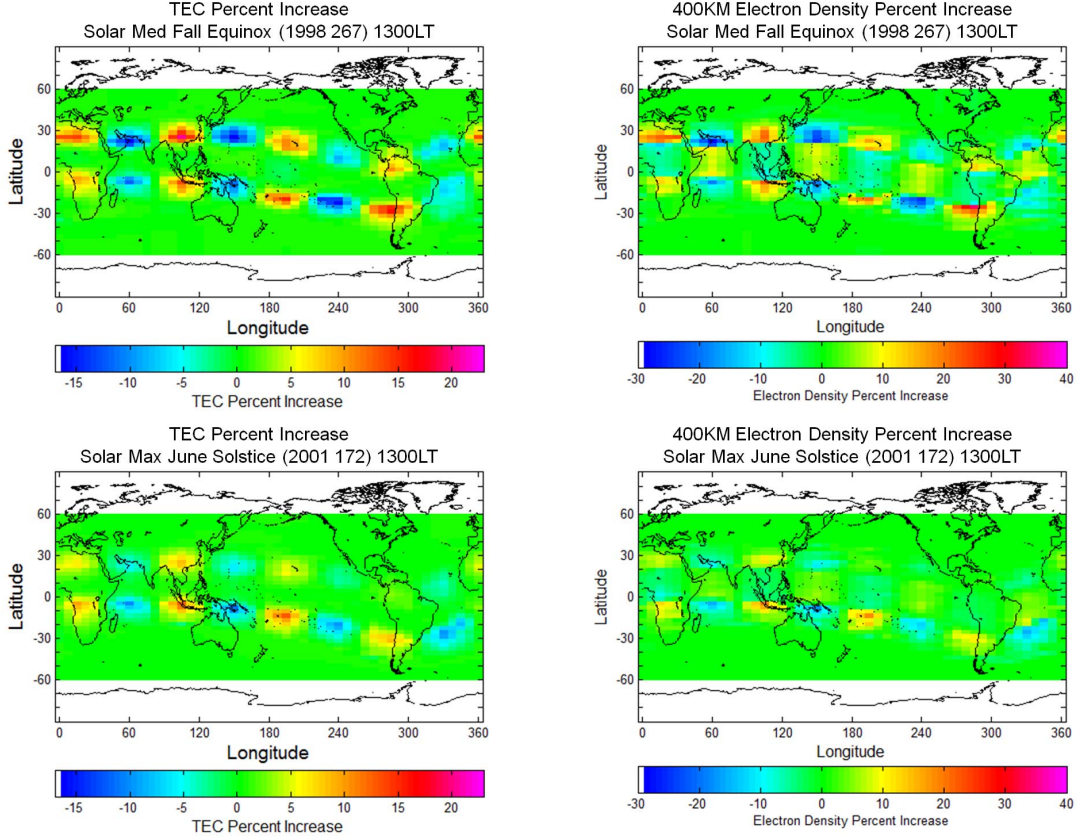


**Figure 42.** TEC and  $400\text{km}$   $N_e$  with tidal forcing for case 2 and 3. The left hand plots are the percent increase in TEC and the right hand plots are the percent increase in  $400\text{km}$   $N_e$  for solar medium fall equinox (top) and solar maximum June solstice (bottom). The plots are for a fixed local time (1300LT). Modulating the  $\vec{E} \times \vec{B}$  drift results in enhancements and depletions in the low latitude TEC and  $400\text{km}$   $N_e$ . Note that the scales are different for each geophysical case

## V. Conclusions and Recommendations

### 5.1 Chapter Overview

This chapter is broken into two sections. The first section summarizes the analysis of the physical parameters in the IPM and reiterates the most significant changes that occurred due to changing these parameters. Recommendations for future research are given in the second section of this chapter.

### 5.2 Conclusions

Understanding the effects of adjusting parameters in a physics-based model is critical in ensuring the accuracy of the model. This study analyzed model performance by varying the  $O^+/O$  collision frequency, downward nighttime  $\vec{E} \times \vec{B}$  drifts, daytime production, zonal winds, and tidal forcing. It was found that when the physical parameters were adjusted in the IPM, the resulting changes were nonlinear and varied with location, time, and solar conditions. The changes ranged from very slight changes in the model output to a 630% increase in TEC and a 900% increase in  $N_e$ . Each parameter had its own unique effect on the model output; the most significant of these changes are summarized below.

The most significant effect of doubling the  $O^+/O$  collision frequency was an increase in the mid latitude nighttime peak electron density ranging from 30–180%. The changes were not consistent across solar cycle, season, or location and so no generalities could be made as to when the smallest and largest changes occurred. Also significant were decreases in electron densities below the peak with a maximum 80% decrease. This decrease occurred because the doubled  $O^+/O$  collision frequency drove the plasma to higher altitudes and the plasma depleted by recombination at low altitudes was not replenished.

It was found that setting the zonal winds to zero resulted in an increase in TEC of up to 400% over the Southeast Pacific Ocean with the largest change occurring during solar maximum June solstice at 1100LT. Near Madagascar on the opposite side of the globe, the TEC decreased with a maximum change of 50% during solar medium fall equinox at 1300LT. The changes in TEC were caused by changes to the magnetic field induced vertical drifts created by the combination of zonal winds and the earth's magnetic field.

The most straightforward results occurred when the production multiplication factor was scaled to correctly account for secondary electron production. The changes to  $N_e$  and TEC were found to be directly proportional to the change in the production factor. The solar maximum production multiplication factor was decreased by 33% with a resulting 33% decrease in low latitude TEC. A production multiplication factor decrease of 25% and 17% during solar medium and minimum, respectively, also resulted in directly proportional changes to the TEC in the equatorial anomalies.

The most significant results of decreasing the nighttime downward  $\vec{E} \times \vec{B}$  drift occurred during solar medium fall equinox. TEC values over the SAA increased 630% while  $300\text{km } N_e$  increased 900%. The solar minimum December solstice case had only slightly smaller changes, while the solar maximum June solstice case had increases of 160% and 250% in TEC and  $300\text{km } N_e$ , respectively. These large changes in the model output show the importance of correctly specifying the physical parameters.

For the final adjustment, tidal forcing was included in the model by modulating the  $\vec{E} \times \vec{B}$  drift and was found to reproduce the four-wave pattern of enhanced TEC at low latitudes. Low latitude TEC and  $400\text{km } N_e$  increased 13–23% and 19–44%, respectively, at longitudes centered at  $15^\circ E$ ,  $110^\circ E$ ,  $200^\circ E$ , and  $290^\circ E$  while decreasing 11–16% (TEC) and 18–28% ( $400\text{km } N_e$ ) at longitudes centered at  $60^\circ E$ ,  $155^\circ E$ ,  $245^\circ E$ , and  $335^\circ E$ . Because the same modification was applied to all three

cases, the largest relative changes occurred during solar minimum and the smallest relative changes occurred during solar maximum.

Except for the adjustment to the daytime production multiplication factor, none of the adjustments produced linear or straightforward changes in the model output. Not only did the changes vary as a function of time and solar condition, but they also varied with location. These nonlinear variations with location resulted from the earth's complex magnetic field configuration and the zonal wind distribution in addition to many other factors. The nonlinearity of these relationships makes it difficult to identify which parameters may be causing erroneous model output.

### 5.3 Recommendations for Future Work

Two avenues exist for possible future work stemming from the results of this project. The first is to improve the operational capability of the IPM by comparing the model output to known data and adjusting the parameters until the results are better correlated. The second avenue is to investigate some of the physical parameters more in-depth for a larger set of geophysical conditions.

While this project provided useful information on the range of output that occurred when certain physical parameters were adjusted in the model, no information was given as to the accuracy of the model output, either adjusted or unadjusted. In order for the model to be useful operationally, it must be validated. This can be done by comparing the model output either to another previously validated physical model (e.g. the IFM) or to an actual data set (e.g. the TOPEX database).

Comparing the IPM to the IFM would be the most simple and straightforward way to perform an initial validation of the IPM. The physical parameters have already been optimized in the IFM and using these optimized values for the parameters in the IPM would provide an ideal starting point for the IPM validation. In addition,

comparing the IPM to the IFM would allow a wide range of controlled geophysical cases to be examined. Ideally, this comparison would serve to optimize the physical parameters in the IPM before it is compared to actual observational data.

Even if the IPM is compared to another physical model, the IPM still needs to be compared to actual data to ensure the accuracy of model. Because the TOPEX TEC database covers a large range of geophysical conditions, it would be a good observational database to use for the validation. However, there are many other sources of data that can be used to validate the IPM including ionosondes, GPS TEC, and the Constellation Observing System for Meteorology, Ionosphere, and Climate (COSMIC) occultations. If an IPM/IFM type comparison is not done, this comparison would serve as an opportunity to optimize the physical parameters in the IPM.

While the operational capability of the IPM is important, this research also has significant implications from a theoretical viewpoint. Understanding in more depth how adjusting each of these parameters, specifically the  $O^+/O$  collision frequency and the zonal winds, modifies electron densities and TEC would be useful in gaining a better understanding of ionospheric processes. These two parameters are highlighted because they showed the greatest nonlinearity in the model output changes. While this project provided a broad overview of the range of model output that results from the uncertainty in these physical parameters, these two parameters could be looked at in more detail. For example, this project varied the level of solar activity and season together; different relationships may be present if only the seasons are varied and the level of solar activity is kept constant. Additionally, the temporal and spatial resolution could be increased over regions where the model output is changing the most. Focusing the research on just these two parameters for more geophysical cases with an increased temporal and spatial resolution may show additional trends and relations in the nonlinearity of the results presented in this paper.

## Appendix A. Ionosphere Forecast Model

The Ionosphere Forecast Model (IFM) is a physics-based model that calculates the three-dimensional time dependent electron and ion density distributions from 90–1600km (*Schunk et al.*, 1997). Density distributions are given for four major ions ( $NO^+$ ,  $O_2^+$ ,  $N_2^+$ , and  $O^+$ ) in the E region, two major ( $O^+$  and  $NO^+$ ) and two minor ( $N_2^+$  and  $O_2^+$ ) ions in the F region, and the ion and electron temperatures for the entire profile (*Schunk et al.*, 2004). In addition, the IFM calculates the  $H^+$  densities for the F region and the topside ionosphere. A numerical solution to the ion continuity, momentum, and energy equations is used to determine the ion distributions. Based on the quasi-neutral state of the ionosphere, the electron density profile is derived from the ion density information.

In the E region, chemical equilibrium (Equation 2) is assumed for all four major ions with each ion having comparable density. The four coupled nonlinear equations are solved using a Taylor series expansion and iterating to a final solution (*Schunk and Sojka*, 1994). In the F region, transport is important and the two major ion densities are solved using numerical techniques for the coupled continuity and momentum equations. The two minor ions in the F region are assumed to be in chemical equilibrium and their densities are solved using Equation 2. The  $H^+$  densities in the topside ionosphere are computed by comparing the concentrations of  $H^+$  and  $O^+$  and by using a combination of chemical and diffusive equilibrium relations.

The IFM can be run on a global, regional, or local scale and has a global spatial resolution of  $3^\circ$  latitude and  $7.5^\circ$  longitude. The internal vertical resolution of the IFM is 4km, but the output resolution is variable starting at 4km in the E region, increasing to 16km in the F region, and has a maximum spacing of 96km at 1600km. The magnetic field is determined using a simplified version of the International Geomagnetic Reference Field (IGRF) that accounts for a tilted offset dipole field.

The IFM is an autonomous model that uses empirical (statistical) models for many of the required inputs. The major inputs required by the IFM are density and temperature profiles for the major neutrals ( $N_2$ ,  $O_2$ , and  $O$ ), neutral winds, magnetospheric and equatorial electric fields, auroral precipitation, and topside heat flow (*Schunk and Sojka*, 1994). The Mass Spectrometer and Incoherent Scatter (MSIS) model is used for the neutral density and temperature profiles. This empirical model provides these parameters based on a given set of geophysical conditions (solar cycle, season, geomagnetic activity, etc.). The zonal and meridional neutral winds are obtained from the Horizontal Wind Model (HWM) developed by *Hedin et al.* (1991). To account for the magnetospheric electric field, the IFM uses the *Heppner and Maynard* (1987) model, which gives electric fields in the polar regions as a function of  $K_p$ . The dynamo equatorial electric field model that is used in IFM calculations is the *Fejer et al.* (1999) model. Auroral precipitation accounted for in the IFM using the model developed by *Hardy et al.* (1985). Finally, *Schunk et al.* (1997) discusses how the topside heat flow is modeled in the IFM.

Validation of the IFM resulted in minor adjustments to certain physical parameters in the model due to discrepancies between model output and observations. These adjustments included modifications to the  $O^+/O$  collision frequency, zonal winds, tidal forcing, and ion production rates. The  $O^+/O$  collision frequency is known to be uncertain up to a factor of 2.0; correct densities were obtained in the IFM with a coefficient of 1.0 (*Schunk*, 2010). It was found that in certain geographic regions, most notably around Madagascar, the combination of the magnetic field configuration and HWM derived zonal winds led to large upward plasma drifts and enhanced electron densities in the IFM output. Setting the zonal winds to zero corrected these density enhancements. The third adjustment was to the daytime ion production rate. This rate was decreased as a linear function of  $F_{10.7}$  (*Schunk*, 2010) with the larger decreases

occurring during solar maximum conditions. This adjustment was done to counter the uncertainty in the secondary electron production calculation. Another adjustment corrected the nighttime equatorial regions with TEC values that were too low by 5–10 TEC units. USU corrected this problem by decreasing the nighttime  $\vec{E} \times \vec{B}$  drift and tested the output for various geophysical conditions. A four-wave pattern of enhanced TEC is known to exist in the ionosphere and is created by atmospheric tides (*Scherliess et al.*, 2008). The IFM cannot reproduce these tides, and so a longitudinal modulation of the  $\vec{E} \times \vec{B}$  drift was introduced into the IFM to simulate the tidal forcing. Adding this modulation reproduced the known pattern of TEC enhancements. Finally, the high latitude portion of the model had to be adjusted due to unrealistic F region densities near South America for specific geophysical conditions (winter, solar minimum, 06LT–12LT). The unique combination of the season, winds, magnetic field configuration, and high-latitude convection in this region formed the enhanced densities. Table 7 summarizes the improvements made to the IFM.

**Table 7. Improvements to the Ionosphere Forecast Model**

Parameter	Description
$O^+/O$ Collision Frequency	Scaled the $O^+/O$ collision frequency
Zonal Winds	Set zonal winds in HWM to zero
Tidal Forcing	Included atmospheric tidal forcing at low latitudes
Daytime Production	Decreased production as a linear function of $F_{10.7}$
Nighttime Drifts	Decreased nighttime equatorial $\vec{E} \times \vec{B}$
High Latitudes	Adjusted electron densities near South America

The IFM requires as input the day, year, UT start time, number of loops to run, output interval, daily and 90-day average  $F_{10.7}$  solar flux, three-hour  $K_p$  index, daily  $A_p$  index, and internal and external resolution settings. If a previous IFM run is not available, the IFM will be initiated using the empirical International Reference Ionosphere (IRI) model. This is not ideal, and in this case the IFM output is degraded for

the first 12 hours. Therefore, the model should be run for two days—one degraded day and one good day of output (*Space Environment Corporation*, 2002). Running the model for longer than two days also causes invalid output as some of the adjustments to the model do not extend past day two (*Schunk*, 2010). The two-day IFM run takes approximately six hours and the output is in a scientific binary data format as a Network Common Data Form (netCDF) file. The IFM output includes the one-dimensional latitude, longitude, and altitude arrays; the two-dimensional TEC, F<sub>2</sub> and E region peak electron density and height arrays; and the three-dimensional electron density, ion density, and ion and electron temperature arrays. More information on the options available in the IFM and how to run the IFM is available in the IFM User Manual (*Space Environment Corporation*, 2002).

## Appendix B. Governing Processes in the Ionosphere

### 2.1 Neutral Atmosphere

The major neutrals in the ionosphere are molecular nitrogen ( $N_2$ ), molecular oxygen ( $O_2$ ), and atomic oxygen ( $O$ ), with minor concentrations of argon ( $Ar$ ), helium ( $He$ ), and hydrogen ( $H$ ). The concentrations of each of these species varies with height and can be approximated using a hydrostatic equilibrium solution. Hydrostatic equilibrium occurs when the forces due to pressure and gravity are in balance. Where this balance occurs, the density of a species as a function of altitude ( $z$ ) is given as

$$N_s(z) = N_s(z_0) \exp \left[ -\frac{z - z_0}{H_s} \right] \quad (19)$$

where  $N_s$  is the number density,  $z_0$  is a reference altitude, and  $H_s$  is the scale height for the species  $s$  given by

$$H_s = \frac{k_b T_s(z)}{m_s g(z)}$$

where  $k_b$  is Boltzmann's constant,  $T_s$  is the temperature,  $m_s$  is the mass, and  $g$  is gravity. In this approximation, the concentration of the species falls off primarily as a function of mass. Therefore, the concentrations of  $N_2$  and  $O_2$  decrease more rapidly with height than does the concentration of  $O$ . Figure 43 shows the vertical variation up to 1000km of the neutral concentrations during solar maximum using this assumption. The relative abundance of each neutral compared with the other neutrals is important when calculating the production and loss of ions.

### 2.2 Production and Loss

Photoionization is the primary production mechanism for creating ion-electron pairs in the low to mid latitude ionosphere. This ionization results from the absorption by neutrals of solar extreme ultraviolet (EUV) and X-ray radiation. Production due

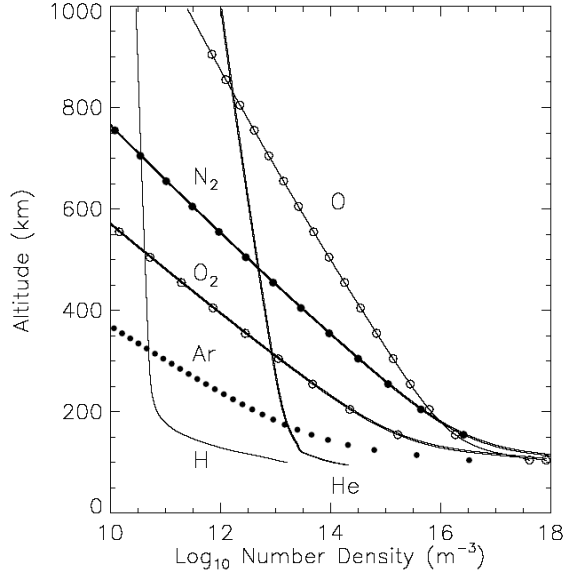


**Figure 43. Major and minor neutral concentrations during solar maximum as a function of altitude as computed by MSIS. Heavier ion concentrations decrease with altitude faster than the light ions**

to photoionization depends on the incoming solar flux, the optical depth, the neutral concentrations, and the ionization cross section. Each of these factors may also depend on species, altitude ( $z$ ), wavelength ( $\lambda$ ), or zenith angle ( $\chi$ ); for a particular species  $s$ , the photoionization rate is given as

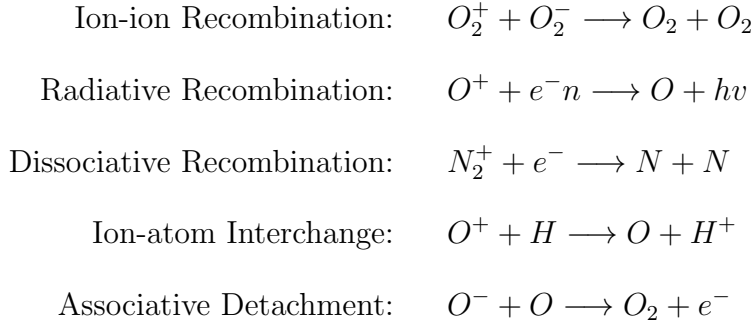
$$P_s(z, \chi) = N_s(z) \int_0^{\lambda_{si}} I_\infty(\lambda) \exp[-\tau(z, \chi, \lambda)] \sigma_s^i(\lambda) d\lambda \quad (20)$$

where

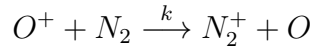
- $I_\infty(\lambda)$  is the solar flux at the top of the atmosphere
- $N_s(z)$  is the number density
- $\tau(z, \chi, \lambda)$  is the optical depth
- $\sigma_s^i(\lambda)$  is the ionization cross section
- $\lambda_{si}$  is the threshold wavelength for ionization

Also contributing to ion production are chemical reactions, secondary electron production, and impact ionization.

The primary ion loss mechanisms in the ionosphere are chemical reactions. The major loss reactions include ion-ion recombination, radiative recombination, dissociative recombination, ion-atom interchange, and associative detachment. An example of each reaction is given below.



Production and loss due to chemical reactions are dependent on the rate of the particular reaction and on the concentrations of the reactants. For a reaction such as



the production rate of  $N_2^+$  (and the loss rate of  $O^+$ ) is given as

$$P(N_2^+) = L(O^+) = k [O^+] [N_2] \quad (21)$$

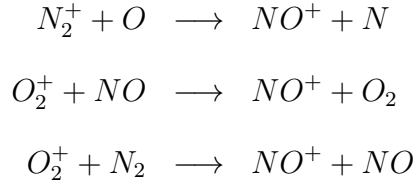
where  $k$  is the reaction rate constant for the specific reaction and  $[O^+]$  and  $[N_2]$  denote the species' concentration. The production and loss rate for each chemical reaction is the terms used in the continuity equation (Equation 1). The reaction rate constant  $k$  is dependent on the temperature of each species in addition to the activation energy of the reaction, which can be described as the minimum energy needed to form the “new” species (Schunk and Nagy, 2009). The reaction rate constant is determined by the equation

$$k_{st} = 2d^2 \sqrt{\frac{2\pi k_b}{\mu_{st}}} \sqrt{T_{st}} \exp\left(-\frac{E_a}{k_b T_{st}}\right) \quad (22)$$

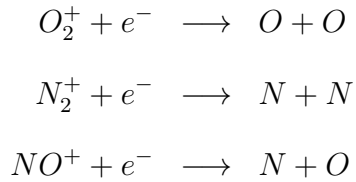
where the subscripts denote each species in the reaction,  $d$  describes the cross-section,  $k_b$  is Boltzmann's constant,  $\mu_{st}$  and  $T_{st}$  are the reduced mass and temperature, respectively, and  $E_a$  is the activation energy. This reaction constant varies by orders of magnitude for the different reaction types listed above which means that some processes will dominate over others. For example, radiative recombination reaction rate constants are on the order of  $10^{-12}$  while dissociative recombination reaction rate constants are on the order of  $10^{-7}$  (Schunk and Nagy, 2009).

In the D region, high neutral concentrations lead to complex chemical reactions. One of these reactions, electron attachment, creates the only significant population of negative ions in the ionosphere. Deep penetration of short wavelength X-ray and EUV radiation also contributes to the complexity of the D region. Due to this complex chemical nature and the difficulty in modeling the shorter wavelengths of the solar spectrum, the D region is not included in the Ionosphere Forecast Model or the Ionosphere-Plasmasphere Model and will not be discussed further here.

The relatively high neutral concentrations in the E region lead to the following chemical reaction production mechanisms for  $NO^+$



Ion-atom interchange is relatively fast compared to dissociative recombination in this region resulting in low concentrations of  $O^+$  and leaving the molecular ions ( $N_2^+$ ,  $O_2^+$ , and  $NO^+$ ) as the major ions. In the  $F_1$  region,  $O^+$  becomes an important ion due to the higher neutral atomic oxygen concentrations at  $F_1$  altitudes. The reaction rate constants determine the loss mechanisms in these regions. Radiative recombination is slow and unimportant, whereas dissociative recombination occurs  $10^5$  times faster (Hargreaves, 1992). The primary dissociative recombination reactions in the E and  $F_1$  regions are



The  $F_2$  region has the same production and loss processes as the E and  $F_1$  regions, however, at and above  $F_2$  region altitudes, plasma transport is significant and determines the density structure. While the  $F_2$  region is controlled by all three processes, the topside ionosphere is controlled by transport alone.

## 2.3 Transport

Transport in the ionosphere is governed by the momentum equation

$$\rho_s \frac{D_s \vec{u}_s}{Dt} = -\nabla p_s - \nabla \cdot \tau_s + \rho_s \vec{G} + n_s q_s \left[ \vec{E} + \vec{u}_s \times \vec{B} \right] + \sum_t \rho_s \nu_{st} (\vec{u}_t - \vec{u}_s) \quad (23)$$

where the subscripts denote the species  $s$  and the target  $t$ ,  $\rho_s$  is the mass density,  $D_s/Dt$  is the convective derivative,  $p_s$  is the pressure,  $k_b$  is Boltzmann's constant,  $\tau_s$  is the stress, and  $\nu_{st}$  is the collision frequency. In obtaining Equation 23, thermal diffusion, Coriolis force, and centripetal force were all assumed to be negligible. After also making the diffusion approximation (steady state and subsonic) Equation 23 reduces to

$$\nabla p_s + \nabla \cdot \tau_s - \rho_s \vec{G} - n_s q_s \left[ \vec{E} + \vec{u}_s \times \vec{B} \right] = \sum_t \rho_s \nu_{st} (\vec{u}_t - \vec{u}_s) \quad (24)$$

In order to further simplify the solution to the momentum equation, two separate cases are considered. First, diffusion along the magnetic field will be examined followed by diffusion perpendicular to the magnetic field. The overall plasma motion is a combination of both solutions.

For diffusion along the magnetic field, the plasma is confined to orbit the magnetic field lines. In this situation the electrons and the major ion species move together and charge neutrality ( $n_e = n_i$ ) and zero current ( $n_e \vec{u}_e = n_i \vec{u}_i$ ) conditions prevail. This ambipolar diffusion behavior is a result of the polarization electric field that develops due to the slight charge separation of the electrons and ions due to their different masses. With this ambipolar diffusion approximation and the previously mentioned assumptions, the ion and electron momentum equations along the magnetic field are

given as

$$\nabla_{||} p_i + (\nabla \cdot \tau_i)_{||} - \rho_i \vec{G}_{||} - n_i e \vec{E}_{||} = \rho_i \nu_{ie} (\vec{u}_e - \vec{u}_i)_{||} + \rho_i \nu_{in} (\vec{u}_n - \vec{u}_i)_{||} \quad (25)$$

$$\nabla_{||} p_e + (\nabla \cdot \tau_e)_{||} - \rho_e \vec{G}_{||} + n_e e \vec{E}_{||} = \rho_e \nu_{ei} (\vec{u}_i - \vec{u}_e)_{||} + \rho_e \nu_{en} (\vec{u}_n - \vec{u}_e)_{||} \quad (26)$$

where  $\vec{E}_{||}$  is the polarization electric field. Adding these equations together and solving for the ion velocity gives the *ambipolar diffusion equation*

$$\vec{u}_{i||} = -D_a \left[ \frac{1}{n_i} \nabla_{||} n_i + \frac{1}{T_p} \nabla_{||} T_p - \frac{m_i \vec{G}_{||}}{2k_b T_p} + \frac{(\nabla \cdot \tau_i)_{||}}{2n_i k_b T_p} - \frac{m_i}{2k_b T_p} \nu_{in} \vec{u}_{n||} \right] \quad (27)$$

where terms containing the electron mass ( $m_e$ ) were neglected and the ideal gas law was used, and where the ambipolar diffusion coefficient ( $D_a$ ) and plasma temperature ( $T_p$ ) are given by

$$\begin{aligned} D_a &= \frac{2k_b T_p}{m_i \nu_{in}} \\ T_p &= \frac{T_e + T_i}{2} \end{aligned}$$

Equation 27 shows that in steady state, the ions will move along the magnetic field with the neutral wind subject to temperature gradients, density gradients, gravity, and stress forces.

For diffusion across the magnetic field, the stress term in Equation 24 is also assumed to be negligible giving

$$\nabla p_s - \rho_s \vec{G} - n_s q_s [\vec{E}_\perp + \vec{u}_s \times \vec{B}] = \rho_s \nu_{sn} (\vec{u}_n - \vec{u}_s) \quad (28)$$

where  $\vec{E}_\perp$  is an applied electric field, the subscript  $s$  denotes either an electron or ion, and the electron-ion collisions are neglected because the momentum transfer

is small (*Schunk and Nagy*, 2009). Transforming Equation 28 to a reference frame moving with the neutral wind ( $\vec{u}_s \rightarrow \vec{u}'_s + \vec{u}_n$ ) simplifies the solution and introduces an effective electric field given by  $\vec{E}'_\perp = \vec{E}_\perp + \vec{u}_n \times \vec{B}$ . Equation 28 then becomes

$$\nabla p_s - \rho_s \vec{G} - n_s q_s \left[ \vec{E}'_\perp + \vec{u}'_{s\perp} \times \vec{B} \right] = -\rho_s \nu_{sn} \vec{u}'_{s\perp} \quad (29)$$

Solving for  $\vec{u}'_{s\perp}$  gives

$$\vec{u}'_{s\perp} - \frac{q_s}{m_s \nu_{sn}} \left( \vec{u}'_{s\perp} \times \vec{B} \right) = \frac{-1}{n_s m_s \nu_{sn}} \nabla_\perp p_s + \frac{1}{\nu_{sn}} \vec{G}_\perp + \frac{q_s}{m_s \nu_{sn}} \vec{E}'_\perp \quad (30)$$

Equation 30 is simplified as

$$\vec{u}'_{s\perp} - K \left( \vec{u}'_{s\perp} \times \hat{b} \right) = \frac{-D_s}{p_s} \nabla_\perp p_s + \frac{1}{\nu_{sn}} \vec{G}_\perp + \mu_s \vec{E}'_\perp \quad (31)$$

using the following relations

$$\begin{aligned} p_s &= n_s k_b T_s & \mu_s &= \frac{q_s}{m_s \nu_{sn}} \\ \omega_{cs} &= \frac{q_s B}{m_s} & \hat{b} &= \frac{\vec{B}}{B} \\ D_s &= \frac{k_b T_s}{m_s \nu_{sn}} & K &= \frac{\omega_{cs}}{\nu_{sn}} \end{aligned}$$

Because  $\vec{u}'_{s\perp}$  is perpendicular to the magnetic field, it can have two orientations. Consider a coordinate system at the equator where the magnetic field  $\vec{B}$  is pointed north in the  $\hat{b}$  direction. Then the components of  $\vec{u}'_{s\perp}$  can be in the downward ( $\hat{i}$ ) direction or the horizontal eastward ( $-\hat{j}$ ) direction. Separating  $\vec{u}'_{s\perp}$  in Equation 31 into these components and simplifying gives

$$\vec{u}'_{s\perp_D} \hat{i} - \vec{u}'_{s\perp_H} \hat{j} + K \vec{u}'_{s\perp_D} \hat{j} + K \vec{u}'_{s\perp_H} \hat{i} = \frac{-D_s}{p_s} \nabla_{\perp_D} p_s \hat{i} + \frac{1}{\nu_{sn}} \vec{G}_{\perp_D} \hat{i} + \mu_s \vec{E}'_{\perp_D} \hat{i} \quad (32)$$

where the variations of the density gradient, gravity, and electric field are small in the horizontal direction and can be neglected. Equating all the terms in the  $\hat{i}$  direction and all the terms in the  $\hat{j}$  direction, we can write

$$\vec{u}'_{s\perp_D} + K\vec{u}'_{s\perp_H} = \frac{-D_s}{p_s} \nabla_{\perp} p_s + \frac{1}{\nu_{sn}} \vec{G}_{\perp} + \mu_s \vec{E}'_{\perp} \quad (33)$$

$$\vec{u}'_{s\perp_H} = K\vec{u}'_{s\perp_D} \quad (34)$$

Substituting  $\vec{u}'_{s\perp_H}$  from Equation 34 into Equation 33 and simplifying gives

$$\vec{u}'_{s\perp_D} = \frac{1}{1+K^2} \left[ \frac{-D_s}{p_s} \nabla_{\perp} p_s + \frac{1}{\nu_{sn}} \vec{G}_{\perp} + \mu_s \vec{E}'_{\perp} \right] \quad (35)$$

Equation 35 describes the vertical drift that is perpendicular to the magnetic field but parallel to the force causing the drift. For  $\vec{G}_{\perp} = \vec{E}'_{\perp} = 0$  in an unmagnetized case ( $K = 0$ ), Equation 35 reduces to Fick's Law, which states that the particle flux is proportional to the density gradient. Substitution of Fick's Law into the continuity equation results in the classical diffusion equation (*Schunk and Nagy, 2009*).

The horizontal drift is obtained by substituting Equation 35 for  $\vec{u}'_{s\perp_D}$  back into Equation 34 and simplifying, which results in

$$\vec{u}'_{s\perp_H} = \frac{1}{1+1/K^2} [\vec{u}_P + \vec{u}_G + \vec{u}_E] \quad (36)$$

where

$$\begin{aligned} \vec{u}_P &= \frac{-1}{n_s q_s} \frac{(\nabla_{\perp} p_s \times \vec{B})}{B^2} && \text{is the gradient drift} \\ \vec{u}_G &= \frac{m_s}{q_s} \frac{(\vec{G}_{\perp} \times \vec{B})}{B^2} && \text{is the gravitational drift} \\ \vec{u}_E &= \frac{(\vec{E}'_{\perp} \times \vec{B})}{B^2} && \text{is the electromagnetic drift} \end{aligned}$$

These three drifts are perpendicular to both the magnetic field and the force (pressure gradient, gravity, or the electric field) causing the drift. Electrons and ions drift across the magnetic field in opposite directions in the presence of pressure gradients and gravity, but they drift together in the presence of a perpendicular electric field. Typically the drifts due to pressure gradients and gravity are small and the dominant drift is the electromagnetic drift.

Since  $\vec{u}'_{s\perp} = \vec{u}'_{s\perp_D} + \vec{u}'_{s\perp_H}$ , the total plasma drift across the magnetic field is

$$\vec{u}'_{s\perp} = \frac{1}{1+K^2} \left[ \frac{-D_s}{p_s} \nabla_{\perp} p_s + \frac{1}{\nu_{sn}} \vec{G}_{\perp} + \mu_s \vec{E}'_{\perp} \right] + \frac{1}{1+\frac{1}{K^2}} [\vec{u}_P + \vec{u}_G + \vec{u}_E] \quad (37)$$

When collisions are negligible  $K \rightarrow \infty$  and the first term of Equation 37 drops out leaving only the motion perpendicular to both the magnetic field and the force. This approximation is valid at high altitudes. In locations where  $K \rightarrow 0$ , the second term drops out leaving only the motion perpendicular to the magnetic field but parallel to the force. This situation occurs at low altitudes where the magnetic field strength is small compared to the collision frequency. At intermediate locations where neither approximation is valid, the plasma motion will be a combination of these motions and will move perpendicular to the magnetic field and at an angle to the force causing the motion (Kelley, 1989).

## Bibliography

Decker, D. T., and L. F. McNamara, Validation of ionospheric weather predicted by Global Assimilation of Ionospheric Measurements (GAIM) models, *Radio Science*, 42, 2007.

Fejer, B., L. Scherliess, and E. R. de Paula, Effects of the vertical plasma drift velocity on the generation and evolution of equatorial spread F, *Journal of Geophysical Research*, 104, 1999.

Finlay, C. C., et al., International geomagnetic reference field: the eleventh generation, *Geophysical Journal International*, 183, 2010.

Gardner, L., Utah State University, Logan UT, Personal Correspondence, 2010.

Hardy, D. A., M. S. Gussenhoven, and E. Holeman, A statistical model of auroral electron precipitation, *Journal of Geophysical Research*, 90, 1985.

Hargreaves, J. K., *The solar-terrestrial environment*, Cambridge University Press, Cambridge, 1992.

Hedin, A. E., Extension of the MSIS thermospheric model into the middle and lower atmosphere, *Journal of Geophysical Research*, 96, 1991.

Hedin, A. E., M. A. Biondi, R. G. Burnside, G. Hernandez, R. M. Johnson, T. L. Kileen, and C. Mazaudier, Revised global model of thermosphere winds using satellite and ground-based observations, *Journal of Geophysical Research*, 96, 1991.

Heppner, J. P., and N. C. Maynard, Empirical high-latitude electric field models, *Journal of Geophysical Research*, 92, 1987.

Horvath, I. H., and E. A. Essex, The Weddell sea anomaly observed with the TOPEX satellite data, *Journal of Atmospheric and Solar-Terrestrial Physics*, 65, 2003.

Immel, T. J., E. Sagawa, S. L. England, S. B. Henderson, M. E. Hagan, S. B. Mende, H. U. Frey, C. M. Swenson, and L. J. Paxton, Control of equatorial ionospheric morphology by atmospheric tides, *Geophysical Research Letters*, 33, 2006.

Jee, G., A. G. Burns, Y. H. Kim, and W. Wang, Seasonal and solar activity variations of the Weddell Sea Anomaly observed in the TOPEX total electron content measurements, *Journal of Geophysical Research*, 114, 2009.

Kelley, M. C., *The Earth's Ionosphere Plasma Physics and Electrodynamics*, Academic Press, San Diego, 1989.

Lean, J., Variations in the sun's radiative output, *Reviews of Geophysics*, 29, 1991.

Liu, H., H. Luhr, S. Watanabe, W. Kohler, V. Henize, and P. Visser, Zonal winds in the equatorial upper thermosphere: Decomposing the solar flux, geomagnetic activity, and seasonal dependencies, *Journal of Geophysical Research*, 111, 2006.

Prolss, G. W., *Physics of the Earth's Space Environment*, Springer, Berlin Germany, 2004.

Scherliess, L., R. W. Schunk, J. J. Sojka, and D. C. Thompson, Development of a physics-based reduced state Kalman filter for the ionosphere, *Radio Science*, 39, 2004.

Scherliess, L., R. W. Schunk, J. J. Sojka, D. C. Thompson, and L. Zhu, Utah State University Global Assimilation of Ionospheric Measurements Gauss-Markov Kalman filter model of the ionosphere: Model description and validation, *Journal of Geophysical Research*, 111, 2006.

Scherliess, L., D. C. Thompson, and R. W. Schunk, Longitudinal variability of low-latitude total electron content: Tidal influences, *Journal of Geophysical Research*, 113, 2008.

Scherliess, L., D. C. Thompson, and R. W. Schunk, Ionospheric dynamics and drivers obtained from a physics-based data assimilation model, *Radio Science*, 44, 2009.

Schunk, R. W., Utah State University, Logan UT, Personal Correspondence, 2010.

Schunk, R. W., and A. Nagy, *Ionospheres: Physics, Plasma Physics, and Chemistry*, second ed., Cambridge University Press, Cambridge, 2009.

Schunk, R. W., and J. J. Sojka, Development of a Global Ionospheric Forecast Model: Final report, 5 December 1990-5 July 1994, *Tech. Rep. PL-TR-94-2232*, Space Environment Corporation, Logan UT, 1994.

Schunk, R. W., J. J. Sojka, and J. V. Eccles, Expanded capabilities for the Ionospheric Forecast Model: Final report, 12 May 1994-30 September 1997, *Tech. Rep. AFRL-VS-HA-TR-98-0001*, Space Environment Corporation, Logan UT, 1997.

Schunk, R. W., L. Scherliess, and J. J. Sojka, Ionospheric specification and forecast modeling, *Journal of Spacecraft and Rockets*, 39, 2002.

Schunk, R. W., et al., Global Assimilation of Ionospheric Measurements (GAIM), *Radio Science*, 39, 2004.

Space Environment Corporation, Ionospheric Forecast Model User Manual, 2002.

Tascione, T. F., *Introduction to the Space Environment*, second ed., Krieger Publishing Company, Malabar FL, 1994.

Thompson, D. C., L. Scherliess, J. J. Sojka, and R. W. Schunk, The Utah State University Gauss-Markov Kalman filter of the ionosphere: The effect of slant TEC and electron density profile data on model fidelity, *Journal of Atmospheric and Solar-Terrestrial Physics*, 68, 2006.

Thompson, D. C., L. Scherliess, J. J. Sojka, and R. W. Schunk, Plasmasphere and upper ionosphere contributions and corrections during the assimilation of GPS slant TEC, *Radio Science*, 44, 2009.

Titheridge, J. E., Temperatures in the upper atmosphere and plasmasphere, *Journal of Geophysical Research*, 100, 1998.

Zhu, L., R. W. Schunk, G. Lee, L. Scherliess, J. J. Sojka, and D. C. Thompson, Validation study of the Ionosphere Forecast Model using the TOPEX total electron content measurements, *Radio Science*, 41, 2006.

## Vita

Capt Janelle Jenniges was born in Luverne, Minnesota. After graduating at the top of her class from Ellsworth Public High School in 2001, she studied Meteorology at the University of Nebraska-Lincoln (UNL). She graduated with honors with a Bachelor of Science Degree in Meteorology in December of 2005. At the same time, Capt Jenniges commissioned into the United States Air Force through the Reserve Officer Training Corp (ROTC) Detachment 465 at UNL.

Capt Jenniges' initial assignment upon commissioning was to the 21st Operational Weather Squadron at Sembach AB, Germany where she served as an assistant flight commander and as the 603d Support Group Executive Officer. Capt Jenniges PCA'd to Ramstein AB, Germany in 2008 to work as a staff weather officer for 17 AF, Air Forces Africa. In May 2009, she entered the Graduate Applied Physics program, School of Engineering, Air Force Institute of Technology to obtain a Master's Degree in physics with a specialization in space weather. Upon graduation, she will be assigned to the Air Force Weather Agency at Offutt AFB, Nebraska.

# REPORT DOCUMENTATION PAGE

Form Approved  
OMB No. 0704-0188

The public reporting burden for this collection of information is estimated to average 1 hour per response, including the time for reviewing instructions, searching existing data sources, gathering and maintaining the data needed, and completing and reviewing the collection of information. Send comments regarding this burden estimate or any other aspect of this collection of information, including suggestions for reducing this burden to Department of Defense, Washington Headquarters Services, Directorate for Information Operations and Reports (0704-0188), 1215 Jefferson Davis Highway, Suite 1204, Arlington, VA 22202-4302. Respondents should be aware that notwithstanding any other provision of law, no person shall be subject to any penalty for failing to comply with a collection of information if it does not display a currently valid OMB control number. PLEASE DO NOT RETURN YOUR FORM TO THE ABOVE ADDRESS.

1. REPORT DATE (DD-MM-YYYY)	2. REPORT TYPE	3. DATES COVERED (From — To)		
24-03-2011	Master's Thesis	May 2009 — March 2011		
4. TITLE AND SUBTITLE		<p>Sensitivity Analysis of Empirical Parameters in the Ionosphere-Plasmasphere Model</p> <p>5a. CONTRACT NUMBER</p> <p>5b. GRANT NUMBER</p> <p>5c. PROGRAM ELEMENT NUMBER</p>		
6. AUTHOR(S)		<p>Jenniges, Janelle V., Capt, USAF</p> <p>5d. PROJECT NUMBER</p> <p>5e. TASK NUMBER</p> <p>5f. WORK UNIT NUMBER</p>		
7. PERFORMING ORGANIZATION NAME(S) AND ADDRESS(ES)			8. PERFORMING ORGANIZATION REPORT NUMBER	
Air Force Institute of Technology Graduate School of Engineering and Management (AFIT/EN) 2950 Hobson Way WPAFB OH 45433-7765			AFIT/GAP/ENP/11-M03	
9. SPONSORING / MONITORING AGENCY NAME(S) AND ADDRESS(ES)			10. SPONSOR/MONITOR'S ACRONYM(S)	
Air Force Weather Agency 101 Nelson Drive Offutt AFB, NE 68113 DSN 271-0690, COMM 402-294-0690 Email: 2syosdor@offutt.af.mil			AFWA	
12. DISTRIBUTION / AVAILABILITY STATEMENT			11. SPONSOR/MONITOR'S REPORT NUMBER(S)	
APPROVED FOR PUBLIC RELEASE; DISTRIBUTION UNLIMITED.				
13. SUPPLEMENTARY NOTES				
This material is declared a work of the U.S. Government and is not subject to copyright protection in the United States.				
14. ABSTRACT				
<p>A sensitivity analysis of empirical parameters used in physics-based models was completed in this study to determine their effect on electron densities and total electron content (TEC) in the ionosphere. The model used was the Ionosphere-Plasmasphere Model (IPM) developed by Utah State University. The empirical parameters studied include the <math>O^+/O</math> collision frequency, zonal wind, secondary electron production, nighttime <math>\vec{E} \times \vec{B}</math> drifts, and tidal structure. The sensitivity analysis was completed by comparing a default run of the IPM to a run with the parameter adjusted for three geophysical cases. Many of the comparisons resulted in nonlinear changes to the model output. Doubling the <math>O^+/O</math> collision frequency increased <math>N_m F_2</math> up to 250% in the equatorial anomalies. Setting the zonal winds to zero resulted in a 400% increase in TEC units (TECU) over the Southeast Pacific and a 50% decrease near Madagascar. It was found that changes in electron density and TEC are directly proportional to how daytime production is scaled to account for secondary electron production. Decreasing the nighttime downward <math>\vec{E} \times \vec{B}</math> drift resulted in a 160%–630% increase in low latitude TEC. Finally, modulating the <math>\vec{E} \times \vec{B}</math> drift to simulate tidal forcing reproduced the four-wave pattern of enhanced low latitude TEC.</p>				
15. SUBJECT TERMS				
Ionosphere, Ionosphere-Plasmasphere Model, Physics-based Models, Space Weather				
16. SECURITY CLASSIFICATION OF:		17. LIMITATION OF ABSTRACT	18. NUMBER OF PAGES	19a. NAME OF RESPONSIBLE PERSON
a. REPORT	b. ABSTRACT	c. THIS PAGE	UU	Lt Col Ariel O. Acebal, AFIT/ENP
U	U	U	108	19b. TELEPHONE NUMBER (include area code) (937) 255-3636, x4518; ariel.acebal@afit.edu